

*(Handwritten initials)*



- A. AN ANALYTICAL AND EXPERIMENTAL STUDY OF THE EROSION BURNING OF COMPOSITE PROPELLANTS
- B. MODELING OF SINGLE PARTICLE ALUMINUM COMBUSTION

Merrill K. King

November, 1977

FINAL REPORT

**[REDACTED]**

Kinetics and Combustion Group  
 Atlantic Research Corporation  
 5390 Cherokee Avenue  
 Alexandria, Virginia 22314

TR-PL-5673

Contract Number F44620-76-C-0023

DDC  
 REPRODUCED  
 FEB 23 1978  
 REGISTERED  
 A

Approved for Public Release; Distribution Unlimited

Air Force Office of Scientific Research  
 Building 410  
 Bolling AFB, DC 20332

**ATLANTIC RESEARCH CORPORATION**  
 ALEXANDRIA, VIRGINIA • 22314

DDC FILE COPY ADA050333

Qualified requestors may obtain additional copies from the Defense Documentation Center. All others should apply to the National Technical Information Service.

CONDITIONS OF REPRODUCTION

Reproduction, translation, publication, use and disposal in whole or in part by or for the United States Government is permitted.

6

- A. AN ANALYTICAL AND EXPERIMENTAL STUDY OF THE EROSIIVE BURNING OF COMPOSITE PROPELLANTS
- B. MODELING OF SINGLE PARTICLE ALUMINUM COMBUSTION.

10 Merrill K./King

12 142 P.

11 Nov 1976

9 FINAL REPORT, 1 Oct 75-30 Sep 77,



Kinetics and Combustion Group  
 Atlantic Research Corporation  
 5390 Cherokee Avenue  
 Alexandria, Virginia 22314

14 TR-PL-5673

16 2308

17 AL

15 Contract Number F44620-76-C-0023

18 AFOSR

Approved for Public Release; Distribution Unlimited

19 TR-78-0060

Air Force Office of Scientific Research  
 Building 410  
 Bolling AFB, DC 20332

AIR FORCE OFFICE OF SCIENTIFIC RESEARCH (AFSC)  
 NOTICE OF TRANSMITTAL TO DDC  
 This technical report has been reviewed and is  
 approved for public release IAW AFR 190-12 (7b).  
 Distribution is unlimited.  
 A. D. BLOSE  
 Technical Information Officer

400 016

JOB



UNCLASSIFIED

SECURITY CLASSIFICATION OF THIS PAGE(When Data Entered)

which does not require even zero-crossflow burning rate data, using only composition and particle size as input, is outlined. In addition, a test device permitting extensive characterization of burning rate-pressure-crossflow velocity relationships for various propellants with direct continuous measurement of instantaneous burning rate by high-speed cinematography is described, and results of a series of tests with seven propellants are presented. These tests indicate that the first generation composite propellant erosive burning model has reasonably good predictive capability, particularly in the higher pressure region, where the propellant combustion is dominated by the propellant heterogeneity. In addition, the tests indicate no dependence of erosive burning on the temperature of the crossflow mainstream gases tending to cast serious doubt on models (such as the Lenoir-Robillard model) which are based upon postulated augmented heat transfer from the mainstream crossflow gases. A model of aluminum particle combustion in CO<sub>2</sub> which incorporates measured kinetic data for the gas phase reaction of aluminum with CO<sub>2</sub> rather than assuming a flame-sheet (infinite gas-phase kinetics) as in past models has been developed, programmed and used to parametrically study the effect of various parameters on particle burning rate and burn-time. This model treats aluminum oxide condensation as occurring in an infinitesimally thin shell whose location is determined by specification of a condensation temperature. Condensation of aluminum oxide at the particle surface is not permitted, but Al<sub>2</sub>O<sub>3</sub> produced by the gas-phase reaction of aluminum vapor with CO<sub>2</sub> is permitted to react with infinite kinetics with aluminum liquid at the surface to form Al<sub>2</sub>O gas, thus removing aluminum from the surface as well as supplying heat to vaporize additional aluminum. Heat feedback from the condensation shell also provides additional energy for aluminum vaporization. Two variations of this model were developed: in one, any CO<sub>2</sub> reaching the surface was permitted to react infinitely rapidly with aluminum liquid to produce Al<sub>2</sub>O gas, while in the other this reaction was prohibited. With the similarity approximations made in the model(s), the former variant leads to a degenerate solution in which the predicted burning rate is independent of the gas-phase kinetics, while the latter variant leads to burning rates predicted with the measured gas-phase kinetic data which are less than those predicted with infinite kinetics assumed. The ratio of burning rates predicted with the measured kinetic data to those predicted with infinite kinetics for the same conditions varies from about 0.3 to 0.95 over the range of conditions studied, increasing with increased particle size, increased pressure, decreased ambient CO<sub>2</sub> mole fraction, and decreased ambient temperature. This ratio asymptotically approaches unity for large particle sizes and asymptotically approaches a value between zero and unity, which depends on ambient conditions at very small particle sizes (where the location of the condensation shell dominates relative to gas-phase kinetics). Burn time versus initial particle diameter calculations indicate a reduction in the exponent in the d<sup>n</sup>-burning law ( $d_0^2 - d^2 = kt$ ) from 2 for the case of infinite kinetics (diffusion-limited burning) to 1.35 - 1.90, depending on ambient conditions.

UNCLASSIFIED

SECURITY CLASSIFICATION OF THIS PAGE(When Data Entered)

Qualified requestors may obtain additional copies from the Defense Documentation Center. All others should apply to the National Technical Information Service.

CONDITIONS OF REPRODUCTION

Reproduction, translation, publication, use and disposal in whole or in part by or for the United States Government is permitted.

TABLE OF CONTENTS

	Page
I. INTRODUCTION . . . . .	1
II. EROSION BURNING OF COMPOSITE PROPELLANTS . . . . .	3
A. Introduction and Background. . . . .	3
B. Analytical Modeling. . . . .	5
1. Review of Past Work. . . . .	5
2. First Generation Model . . . . .	10
3. Second Generation Model. . . . .	15
4. Examination of Effect of Flow Profiles . . . . .	42
C. Experimental . . . . .	46
1. Equipment. . . . .	46
2. Test Matrix. . . . .	51
3. Test Results and Discussion. . . . .	54
D. Conclusions. . . . .	73
III. MODELING OF ALUMINUM PARTICLE COMBUSTION IN CARBON DIOXIDE- NITROGEN MIXTURES, ALLOWING FOR FINITE-RATE KINETICS FOR THE ALUMINUM VAPOR-CARBON DIOXIDE GAS-PHASE REACTION . . . . .	75
A. Introduction and Background. . . . .	75
B. Development of Physical Picture. . . . .	82
C. Model Development. . . . .	89
D. Results. . . . .	99
E. Conclusions. . . . .	120
IV. REFERENCES . . . . .	126
A. Section II . . . . .	126
B. Section III. . . . .	129
V. BIBLIOGRAPHY - Papers and Reports Resulting From This Effort	131

RE: Classified reference, page 126  
 AFOSR-TR-78-0060  
 Reference is no longer classified per  
 Ms. Blöse, AFOSR

LIST OF TABLES

<u>Table No.</u>		<u>Page</u>
II-I	Aero-Time Ballistic Analysis of Nozzleless Motor with Initially Uniform Port Area . . . . .	6
II-II	Erosive Burning Models by Category . . . . .	7
II-III	Variation of Oxidizer Planar Surface Intersection Area and Associated Fuel Surface Area with Distance of Intersection Plane from Top of Particle - Typical Case . . . . .	21
II-IV	Formulations Selected for Testing. . . . .	52
III-I	Rate Constant Data Obtained by Fontijn in a Fast- Flow Tubular Reactor for the Reaction, $Al(g) +$ $CO_2 \rightarrow AlO + CO$ . . . . .	78
III-II	Estimated Reaction Zone Thicknesses for Aluminum Particles Burning in Carbon Dioxide, with Use of Fontijn Rate Data for $Al(g) + CO_2 \rightarrow AlO + CO$ . . . . .	78
III-III	Predicted Burning Rates of Aluminum Particles of Various Sizes Burning in Various $CO_2-N_2$ Environments . . . . .	104
III-IV	Thermodynamic Evaluation of the Assumption of No $Al_2O_3(l)$ Condensation of the Burning Aluminum Particle Surface . . . . .	110

## LIST OF FIGURES

<u>Figure No.</u>		<u>Page</u>
II-1	Schematic of Geometrical Model of Erosive Burning (Two-Flame Model) . . . . .	11
II-2	Erosive Buring Model Predictions and Comparisons with Saderholm Data. Transpiration Effects Included. . . . .	16
II-3	Schematic Demonstrating Calculation of Oxidizer Surface Area at Some Time, TAU, After First Exposure to the Top of the Oxidizer Particle . . . . .	25
II-4	Schematic Showing Key Dimensions Relating to Gas-Phase Heat Release . . . . .	32
II-5	Results of Preliminary Calculations with Second Generation Model, Formulation 4525 (73/27 AP/HTPB, 20 micron diameter AP). . . . .	43
II-6	Erosive Burning Rate Predictions with the First Generation Model Using Mickley-Davis Boundary Layer Profiles and Using Inviscid No-Slip Wall Boundary Layer Profiles. Formulation 4525 (73/27 AP/HTPB, 20 Micron Diameter AP). . . . .	45
II-7	Sketch of Test Hardware. . . . .	48
II-8	Test Section Detail, Emphasizing Viewing Windows . . . . .	50
II-9	Burning Rate Augmentation Ratio Versus Time for Test Condition No. 1, Formulation No. 1 (4525), Nozzled Test, Low Pressure . . . . .	55
II-10	Burning Rate Augmentation Ratio Versus Time for Test Condition No. 8, Formulation No. 1 (4525) - Nozzled Test, High Pressure, No Grain in Transition Section. . . . .	56
II-11	Comparison of Erosive Burning With and Without Test Grain Extending Thru Transition Section to Mate with Driver Grain - Low Pressure. . . . .	57
II-12	Comparison of Erosive Burning With and Without Test Grain Extending Thru Transition Section to Mate with Driver Grain - High Pressure. . . . .	58
II-13	Comparison of Erosive Burning of Formulation 1 (4525) with 1667°K Driver Grain and 2425°K Driver Grain - Low Pressure . . . . .	60
II-14	Comparison of Erosive Burning of Formulation 1 (4525) with 1667°K Driver Grain and 2425°K Driver Grain - High Pressure. . . . .	61
II-15	Theoretical and Experimental Burn Rate - Pressure Relationships for Various Crossflow Velocities for Formulation 4525 (1667°K Formulation, 73/27 AP/HTPB, 20 Micron AP). . . . .	62

LIST OF FIGURES (Continued)

<u>Figure No.</u>	<u>Page</u>
II-16	Burning Rate Versus Crossflow Velocity Data and Predictions for Formulation 4525 (73/27 AP/HTPB, 20 Micron AP) . . . . . 63
II-17	Theoretical and Experimental Burn Rate - Pressure Relationships for Various Crossflow Velocities for Formulation 5051 (1667°K Formulation, 73/27 AP/HTPB, 200 Micron AP) . . . . . 64
II-18	Theoretical and Experimental Burn Rate - Pressure Relationships for Various Crossflow Velocities for Formulation 4685 (1667°K Formulation, 73/27 AP/HTPB, 5 Micron AP) . . . . . 65
II-19	Theoretical and Experimental Burn Rate - Pressure Relationships for Various Crossflow Velocities for Formulation 4869 (1667°K Formulation, 76/22/2 AP/HTPB/Fe <sub>2</sub> O <sub>3</sub> , 20 Micron AP) . . . . . 67
II-20	Theoretical and Experimental Burn Rate - Pressure Relationships for Various Crossflow Velocities for Formulation 5542T (2065°K Formulation, 77/23 AP/HTPB, 20 Micron AP) . . . . . 68
II-21	Theoretical and Experimental Burn Rate - Pressure Relationships for Various Crossflow Velocities for Formulation 5565T (2575°K Formulation, 82/18 AP/HTPB, Bimodal with Sizes Chosen to Match 4525 Burning Rate). . . . . 69
II-22	Theoretical and Experimental Burn Rate - Pressure Relationships for Various Crossflow Velocities for Formulation 5555T (2575°K Formulation, 82/18 AP/HTPB High Burn Rate). . . . . 71
III-1	Predicted Burn Time as a Function of Particle Size For Aluminum Particles, T <sub>AMBIENT</sub> = 2000°K, y <sub>CO<sub>2</sub>, AMBIENT</sub> = 0.5 . 81
III-2	Schematic of Single Particle Aluminum Combustion Model(s) Developed in this Study . . . . . 88
III-3	Predicted Temperature and Concentration Profiles Around Burning Aluminum Particle. Case 13. . . . . 100
III-4	Predicted Temperature and Concentration Profiles Around Burning Aluminum Particle. Case 17 . . . . . 101
III-5	Predicted Temperature and Concentration Profiles Around Burning Aluminum Particle. Case 30. . . . . 102

LIST OF FIGURES (Continued)

<u>Figure No.</u>		<u>Page</u>
III-6	Predicted Ratio of Burning Rate with Fontijn Kinetics to That with Infinite Kinetics . . . . .	105
III-7	Predicted Ratio of Burning Rate with Fontijn Kinetics to That with Infinite Kinetics . . . . .	106
III-8	Burn-Time Versus Particle Radius, $T_{AMB} = 1000^{\circ}K$ , $P = 1 \text{ atm}$ , $Y_{CO_2} = 0.8$ . . . . .	112
III-9	Burn-Time Versus Particle Radius, $T_{AMB} = 1000^{\circ}K$ , $P = 1 \text{ atm}$ , $Y_{CO_2} = 0.65$ . . . . .	113
III-10	Burn-Time Versus Particle Radius, $T_{AMB} = 1000^{\circ}K$ , $P = 1 \text{ atm}$ , $Y_{CO_2} = 0.5$ . . . . .	114
III-11	Burn-Time Versus Particle Radius, $T_{AMB} = 1000^{\circ}K$ , $P = 1 \text{ atm}$ , $Y_{CO_2} = 0.35$ . . . . .	115
III-12	Burn-Time Versus Particle Radius, $T_{AMB} = 1000^{\circ}K$ , $P = 10 \text{ atm}$ , $Y_{CO_2} = 0.5$ . . . . .	116
III-13	Burn-Time Versus Particle Radius, $T_{AMB} = 300^{\circ}K$ , $P = 1 \text{ atm}$ , $Y_{CO_2} = 0.5$ . . . . .	117
III-14	Burn-Time Versus $Y_{CO_2,AMB}$ , $P = 1 \text{ atm}$ , $T_{AMB} = 100^{\circ}K$ , $r_p = 5\mu$ . . .	118
III-15	Burn-Time Versus $Y_{CO_2,AMB}$ , $P = 1 \text{ atm}$ , $T_{AMB} = 1000^{\circ}K$ , $r_p = 30\mu$ . .	119
III-16	Burn-Time Versus Pressure, $Y_{CO_2} = 0.5$ , $T_{AMB} = 1000^{\circ}K$ , $r_p = 5\mu$ . .	121
III-17	Burn-Time Versus Pressure, $Y_{CO_2} = 0.5$ , $T_{AMB} = 1000^{\circ}K$ , $r_p = 20\mu$ . .	122
III-18	Burn-Time Versus $T_{AMBIENT}$ , $P = 1 \text{ atm}$ , $Y_{CO_2} = 0.5$ , $r_p = 5\mu$ . . .	123
III-19	Burn Time Versus $T_{AMBIENT}$ , $P = 1 \text{ atm}$ , $Y_{CO_2} = 0.5$ , $r_p = 20\mu$ . . .	124

## I. INTRODUCTION

This report covers two separate efforts conducted by the author under AFOSR Contract F44620-76-C-0023 from October 1, 1975 to September 30, 1977. The first and larger of these efforts was an analytical and experimental study of the erosive burning of composite propellants, while the second was an analytical modeling study of the combustion of aluminum particles in nitrogen-carbon dioxide mixtures.

Erosive burning, the augmentation of solid propellant burning rate by the flow of products across a burning surface, is becoming increasingly important with use of lower port-to-throat area ratio motors and nozzleless motors which result in high velocity crossflows. The response of various propellants to such crossflows must be known by the motor designer in order for him to perform adequate motor design. In addition, it is important that the propellant formulator understand the effect of various formulation parameters on the sensitivity of a propellant to crossflows so that he may tailor his propellants to the desired characteristics. (For example, in a nozzleless rocket motor, the decrease in pressure from the head end to the aft end of the grain tends to result in slower burning at the aft end in the absence of erosive effects. Depending upon the sensitivity of the formulation to crossflow, the increasing Mach Number along the grain port may lead to undercompensation, exact cancellation, or overcompensation of the pressure effect.) In this program, a test apparatus was constructed for the study of the effects of crossflows up to Mach 1 on propellant ballistics, and seven propellants (with systematically varied formulation parameters) were characterized in this apparatus. In addition, a first generation analytical model for erosive burning of composite propellants based on bending of columnar diffusion flames by crossflow was developed and considerable progress toward development of a more fundamental second generation model (still based on flame-bending) was made. Results of the experimental and analytical efforts to date are described in Section II. This work is being continued under AFOSR Contract F49620-78-C-0016 in fiscal year 1978.

Existing published models of the combustion of aluminum particles employ a flame-sheet approximation wherein the reaction of aluminum vapor and oxidizer is assumed to occur instantaneously in an infinitesimally thin reaction zone located some distance from the particle surface, with the combustion thus being controlled by the diffusion of oxidizer and fuel species to this zone. Preliminary calculations (neglecting condensation effect) of aluminum particle combustion with consideration of finite-rate kinetics using kinetic data recently measured by Fontijn for the reaction of aluminum vapor with carbon dioxide indicated that the flame-sheet approximation is quite poor for aluminum particles smaller than approximately 30 to 50 microns in diameter, a size regime of considerable interest regarding aluminum combustion in solid propellant rocket motors. In fact, this analysis indicated that aluminum particle combustion more closely followed a  $d^1$ - to  $d^{1.5}$ -burning rate law than the  $d^2$ -burning rate law which follows from the assumption of infinite kinetics. Since most laboratory burning rate data available for aluminum particle combustion are for particles of 50 microns and larger diameter while aluminum cast in motors is typically in the 5 to 20 micron diameter range, calculation of degree of combustion of aluminum in motors is quite sensitive to the power law used to extrapolate the laboratory data to motor conditions. Accordingly, a model allowing for finite-rate kinetics for the initial aluminum vapor-oxidizer reaction and also incorporating a postulated description of aluminum oxide condensation was developed for further examination of the sensitivity of predicted burning rate (and burning rate-particle diameter dependency) to the assumption of infinite kinetics. Model development results are presented in Section III.

## II. EROSIIVE BURNING OF COMPOSITE PROPELLANTS

### A. Introduction and Background

Erosive burning refers to the augmentation of "normal" burning rate of a solid propellant by action of a flow of gas parallel to the burning surface. Several empirical relations appear in the literature to describe the total burning rate, which is the sum of the normal and erosive rates.

Data are often correlated by one of the following expressions:

$$\epsilon = r/r_o = 1 + K_1(V - V_t)^m, m \leq 1 \quad (1)$$

$$\epsilon = r/r_o = 1 + K_2(M - M_t)^m, m \leq 1 \quad (2)$$

$$\epsilon = r/r_o = 1 + K_3(G - G_t)^m, m \leq 1 \quad (3)$$

$$\epsilon = r/r_o = 1 + (\alpha G^{0.8} L^{-0.2} / r_o) \exp(-\beta r_o \rho_p / G) \quad (4)$$

$\epsilon$  = erosive burning rate/burning rate at same pressure in the absence of crossflow

$r$  = propellant linear burning rate, including erosive effects

$r_o$  = propellant linear burning rate in the absence of crossflow

$V$  = mainstream crossflow velocity

$M$  = mainstream crossflow Mach Number

$G$  = crossflow mass flux

$L$  = length parameter defining crossflow Reynolds' Number

$\alpha, \beta, K_1, K_2, K_3, m$  = empirical constants

the fourth of these being a form of the Lenoir-Robillard expression. The subscript "t" refers to threshold crossflow conditions below which erosion does not occur. (Some propellants have been correlated with non-zero threshold values, while others have been correlated with threshold values set equal to zero.)

General observations of importance from the past experimental studies (1-10) include:

1. Plots of burning rate versus gas velocity or mass flux at constant pressure are usually not fitted best by a straight line.

2. Threshold velocities and "negative" erosion rates are often observed.
3. Slower burning propellants are more strongly affected by crossflows than higher burning-rate formulations.
4. At high pressure, the burning rate under erosive conditions tends to approach the same value for all propellants (at the same flow velocity) regardless of the burning rate of the propellants at zero crossflow.
5. Erosive burning rates do not depend upon gas temperature of the crossflow (determined from tests in which various "driver propellant's" products are flowed across a given test propellant).

There is, however, very little data available for high crossflow velocities (greater than  $M \approx 0.3$ ). In addition, there has been no study in which various propellant parameters have been systematically varied one at a time. Such a study is necessary for determination of erosive burning mechanisms and proper modeling of the erosive burning phenomena. Much of the past work has not resulted in instantaneous (as opposed to averaged over a range of pressure and crossflow velocity) measurements of erosive burning rates under well-characterized local flow conditions.

Erosive burning can have a strong influence on rocket motor performance (ballistics) as reflected, for example, in pressure-time curves for low port-to-throat area ratio motor designs. Such effects are particularly important in the case of nozzleless rocket motors, where the gas flow is choked near or at the aft end of the grain through most or all of the motor operation. Since this point is thus the effective throat, and the throat area is thus a function of regression rate of a propellant surface being subjected to a very high crossflow velocity, the result is a chamber pressure-time history which is very dependent upon the erosive burning characteristics of the propellant. The effects of erosive burning on solid propellant rocket interior ballistics for low port-to-throat area ratio motors and nozzleless motors are discussed in some detail by this author in Reference 11. As an example, results of an analysis of the ballistics of a nozzleless motor with initially uniform port area, shortly after ignition, with an assumed no-crossflow burning rate pressure

relationship of  $r_o = bp^n$  and an erosivity relationship of  $\epsilon = 1 + K_2M$ , are presented in Table II-I. Values of  $(r_{aft}/r_{fore})_{initial}$  are presented as a function of the erosivity constant ( $K_2$ ) and the burning rate exponent ( $n$ ). As may be seen, for the case of no erosion ( $K_2 = 0$ ), the aft end will recede more slowly than the fore end, due to lower pressure at the aft end. As  $K_2$  increases, the  $r_{aft}/r_{fore}$  ratio also increases, going through unity (generally desirable) at a value of  $K_2$  which depends on the burning rate exponent. The results of Table II-I give some indication of the sensitivity of nozzleless motor design to the erosive burning characteristics of the propellant, and thus point out the importance of information regarding the propellant's erosive burning characteristics to the designer and the propellant formulator.

Since there is such a strong interaction between the local flow environment and the propellant burning rate, it is necessary to be able to predict this interaction in order to design and calculate the performance of a low port/throat area ratio rocket (particularly a nozzleless rocket with a port/throat area ratio of unity). A review of the literature has indicated that there is no unifying model or theory which can be used to reliably predict propellant burning rates in an erosive situation, nor is there a supply of systematic experimental data characterizing the erosive burning behavior of propellants as a function of compositional variables. Thus, development of an analytical model of erosive burning properly describing the physical effects which result in crossflow velocities augmenting solid propellant burning rate, coupled with an experimental program to define the effects of various parameters on erosive burning, is important to the design and development of advanced solid rocket systems.

## B. Analytical Modeling

### 1. Review of Past Work

Over the years, a large number of models of erosive burning of composite (heterogeneous) and double-base (homogeneous) propellants have been developed. A list of models by author's name, divided into four categories of models, is presented as Table II-II. These models have been

TABLE II-I. Zero-Time Ballistic Analysis of Nozzleless Motor with Initially Uniform Port Area

$$\epsilon = r/r_0 = 1 + K_2 M$$

FORE END:  $M = 0$

$$r_{\text{FORE}} = r_{0,\text{FORE}} = b P_{\text{STATIC FORE}}^n$$

AFT END:  $M = 1$

$$r_{\text{AFT}} = (K_2 + 1)r_{0,\text{AFT}} = (K_2 + 1)b P_{\text{STATIC AFT}}^n$$

$$P_{\text{STATIC AFT}}/P_{\text{STATIC FORE}} \approx 1/(\gamma + 1)$$

$$\therefore r_{\text{AFT}} = \frac{(K_2 + 1)b}{(\gamma + 1)^n} P_{\text{STATIC FORE}}^n$$

$$\text{THEREFORE } r_{\text{AFT}}/r_{\text{FORE}} \approx (K_2 + 1)/(\gamma + 1)^n$$

FOR  $\gamma = 1.25$

$n$	$K_2$	$r_{\text{AFT}}/r_{\text{FORE}}$
0.4	0	0.72
	0.5	1.08
	1.0	1.45
	1.5	1.80
0.6	0	0.61
	0.5	0.92
	1.0	1.23
	1.5	1.54
0.8	0	0.52
	0.5	0.78
	1.0	1.05
	1.5	1.31

TABLE II-II. Erosive Burning Models by Category

1. Models Based on Heat Transfer from a "Core Gas" in the Presence of Crossflow:
  - Lenior & Robillard (15)
  - Burick and Osborn (16)
  - Zucrow, Osborn and Murphy (17)
  - Saderholm (3)
  - Marklund (7)
  - Jojic & Blagojevic (18)
  
2. Models based on Alteration of Transport Properties in Region from Surface to Flame Zone by Crossflow, Generally Due to Turbulence Effects. Includes Effects on Conductivity from Flame Zone Back to Propellant and Effects on Time for Consumption of Fuel Pockets Leaving Surface:
  - Saderholm, Biddle, Caveny, et al. (19)
  - Lengellé (20)
  - Corner (Double-Base) (21)
  - Vandenkerckhove (Double-Base) (22)
  - Zeldovich (Double-Base) (23)
  - Vilyunov (Double-Base) (10)
  - Geckler (24)
  
3. Models Based on Chemical Reacting Boundary Layer Theory (Homogeneous Systems Only):
  - Tsuji (25)
  - Beddini, et al. (26)
  - Kuo, et al. (27)
  
4. Other
  - Klimov (18)
  - Molnar (29)
  - Miller (30)
  - King (12,13)

discussed by this author in References 11 - 14, and will not be discussed in detail here. A general weakness of the models in the first category (models based upon added heat transfer from a "core gas" in the presence of crossflow) is that they predict substantial dependence of the erosive burning contribution on the temperature of the core gas: such dependence was found by Marklund and Lake (7) to be absent, as discussed in References 11 - 13. Of the models other than the one developed by this author and discussed below, those of Lengellé (20), Beddini, et al. (26), and Kuo, et al. (27), appear to be the most advanced of the models listed. Common to all three of these models is the assumption that the increase in propellant burning rate associated with crossflow results from turbulence associated with this crossflow penetrating between the propellant gas flame zone(s) and the surface, causing increases in mass and energy transport rates. However, for a typical propellant containing oxidizer particles with diameters of from 10 to 50 microns, diffusion flame distances may be calculated to be typically of the order of one-quarter to one-half of the particle diameter, or 2.5 to 25 microns. On the other hand, for a crossflow velocity of 200 meters/second (650 ft/second), the universal  $u^+$ ,  $y^+$  correlation (transpiration effects neglected) indicates a laminar sublayer thickness of approximately 10 microns and a buffer zone thickness of about 50 microns, full turbulence not being achieved closer than 60 microns from the propellant surface. Moreover, transpiration of the binder and oxidizer decomposition gases from the propellant surface will tend to increase the thickness of these zones. Thus, it is not at all certain that crossflow-induced turbulence does penetrate into the zone between the propellant surface and the gas-phase flame zone(s). In addition, even if the turbulent region does extend into this zone, in order for the eddies to have significant effect on mixing and thus on heat and mass transfer, they must be considerably smaller than the flame offset distance; that is, they must be on the order of one micron in diameter or less. It is not clear to this author that a significant amount of turbulence of this scale will be induced in the zone between the propellant surface and the gas-phase flame zone(s) by crossflows up to Mach 1, more than an order of magnitude above typical erosive burning threshold velocities. Accordingly, an alternate possible mechanism for

erosive burning of composite propellants based upon bending of columnar diffusion flames by a crossflow has been postulated and model development based upon this picture has been carried out by this author.

In the development of a proper model of erosive burning of a given class of propellants, it is necessary that a physical-chemical mechanism for the "normal" (no crossflow) burning of such propellants be specified, that the boundary layer flow be properly described (theoretically or empirically) and that the description of these processes be properly coupled.

Considering first the flow field, it is informative to estimate flow profiles and angles near the surface of a composite propellant for a typical erosive burning situation. As an example, let us examine a case where the operating pressure is  $6.89 \cdot 10^6 \text{ N/m}^2$  (1000 psi), the propellant flame temperature is  $3000^\circ\text{K}$ , the crossflow mainstream velocity is 200 m/sec (650 ft/sec), the characteristic length dimension for determining Reynold's Number is 15 cm (0.5 feet) and the propellant burning rate is 1.25 cm/sec (0.5 in/sec). In this case, the gas velocity away from the surface calculated at the flame temperature is approximately 4 m/sec (13 ft/sec). Using Mickley and Davis's (31) flow profile data for boundary layer velocity profiles in the presence of transpiration, we estimate that the crossflow velocity 10  $\mu\text{m}$  from the propellant surface is about 10 m/sec (30 ft/sec). A simplified energy balance equating the heat feedback flux from a flame sheet above a propellant surface to the value required for preheating and vaporizing the solid ingredients at a regression rate of 1.25 cm/sec (0.5 in./sec) indicates that the gas-phase flame must be on the order of 10  $\mu\text{m}$  from the surface. Thus, at the position of the gas-phase flame front, the velocity component away from the propellant is about 4 m/sec, while the velocity component parallel to the surface is 10 m/sec, and the resultant flow vector makes an angle with the propellant surface of only 22 degrees. While this vector will vary with distance from the surface, since the velocity components normal to and parallel to the surface do not scale with distance from the surface in exactly the same way, the variation will not be great. Thus, fuel and oxidizer gas columns leaving the surface will not flow perpendicular to the surface (as they would in the absence of crossflow, but at an angle of approximately 20 to 25 degrees from parallel with the surface for this typical case.

The important feature of this picture is that any diffusion flame at the AP-binder boundaries is bent over toward the propellant surface by the crossflow velocity. Since the deflection of this mixing column or cone can be shown to cause the distance from the base to the tip, measured perpendicular to the propellant surface, to decrease, the height above the propellant at which any given fraction of the mixing of AP products and fuel decomposition products is complete should therefore be decreased and the distance from the propellant surface to the "average" location of the diffusion flame should also be decreased. This in turn will increase heat feedback and thus increase the burning rate. A first generation model based upon this picture, which permits prediction of burning rate-pressure-crossflow velocity relationships, given only no-crossflow burning rate versus pressure data over a wide pressure range, has been developed. This model, described briefly below, has been presented in detail in Reference 13. In addition, considerable progress has been made on development of a second generation model of a more fundamental nature, requiring as input only propellant composition and particle size data: formulation of this model is also discussed below.

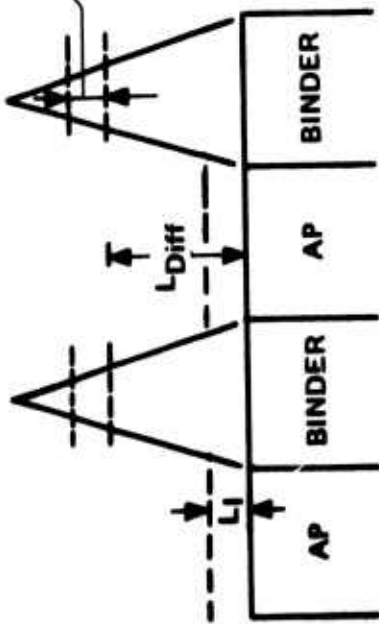
## 2. First Generation Model

A schematic depicting the first generation composite propellant erosive burning model is presented in Figure II-1. In the first part of the figure, we picture the flame processes occurring in the absence of crossflow. There are two flames considered: an ammonium perchlorate deflagration monopropellant flame close to the surface; and a columnar diffusion flame resulting from mixing and combustion of the AP deflagration products and fuel binder pyrolysis products at an average distance somewhat further from the surface. Three important distance parameters considered are the distance from the propellant surface to the "average" location of the kinetically controlled AP monopropellant heat release ( $L_T$ ), the distance associated with mixing of the oxidizer and fuel for the diffusion flame ( $L_{Diff}$ ), and the distance associated with the fuel-oxidizer reaction time subsequent to mixing ( $L_{Kin}$ ). A heat balance between heat

(FUEL-LEAN CASE PICTURED: THEREFORE DIFFUSION FLAME CLOSES OVER BINDER)

DISTANCE ASSOCIATED WITH REACTION TIME  
SUBSEQUENT TO MIXING,  $L_{Kin}$

- ← AVERAGE LEVEL OF HEAT RELEASE FOR SECONDARY FLAME
- ← AVERAGE LEVEL OF END OF FUEL-OXIDIZER MIXING ZONE



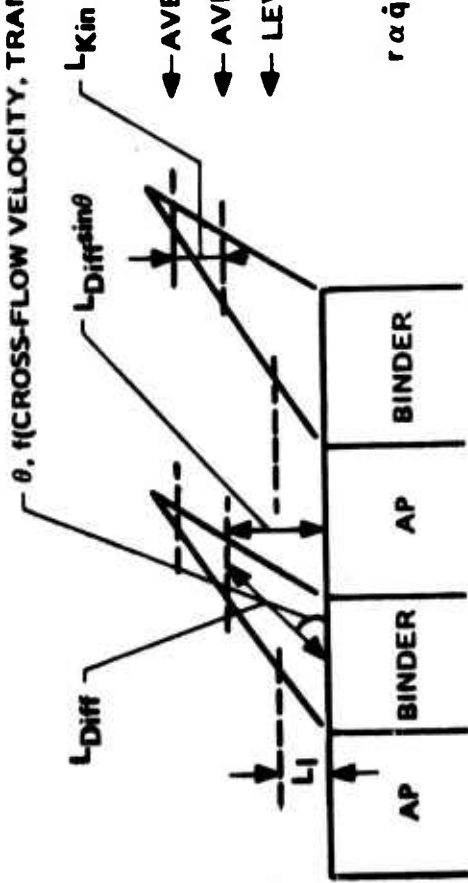
← LEVEL OF AP MONOPROPELLANT FLAME

$$r \alpha \dot{q} = \frac{k_1 (T_{AP} - T_S)}{L_1} + \frac{k_2 (T_f - T_S)}{L_{Diff} + L_{Kin}}$$

a) NO CROSS-FLOW VELOCITY

≡

b) CROSS-FLOW VELOCITY, TRANSPARATION VELOCITY



- ← AVERAGE LEVEL OF HEAT RELEASE FOR SECONDARY FLAME
- ← AVERAGE LEVEL OF END OF FUEL-OXIDIZER MIXING ZONE
- ← LEVEL OF AP MONOPROPELLANT FLAME

$$r \alpha \dot{q} = \frac{k_1 (T_{AP} - T_S)}{L_1} + \frac{k_2 (T_f - T_S)}{L_{Diff} \sin \theta + L_{Kin}}$$

b) CROSS-FLOW,  $L_{Kin}$ ,  $L_{Diff}$ ,  $L_1 = f(\dot{m}, P)$  ALONE, INDEPENDENT OF CROSS-FLOW ANGLE

Figure 11-1. Schematic of Geometrical Model of Erosive Burning (Two-Flame Model).

feedback from these two flames and the energy requirements for heating the propellant from its initial temperature to the burning surface temperature and decomposing it yields (assuming that the heat feedback required per unit mass of propellant consumed is independent of burning rate):

$$\dot{r}_o \propto \dot{q}_{\text{feedback}} \propto \frac{k_1(T_{\text{AP}} - T_s)}{L_I} + \frac{k_2(T_f - T_s)}{L_{\text{Diff}} + L_{\text{Kin}}} \quad (5)$$

$T_{\text{AP}}$  = ammonium perchlorate flame temperature

$T_f$  = propellant flame temperature

$T_s$  = surface temperature

$\dot{q}_{\text{feedback}}$  = heat feedback flux from gas flames to propellant surface

$k_1$  = ratio of heat feedback flux from AP flame to the average temperature gradient from that flame to the surface

$k_2$  = ratio of heat feedback flux from columnar diffusion flame to the average temperature gradient from that flame to the surface.

The situation pictured as prevailing with a crossflow is shown in the second part of Figure II-1. Since  $L_I$  and  $L_{\text{Kin}}$  are both kinetically controlled and are thus simply proportional to a characteristic reaction time (which is assumed to be unaffected by the crossflow) multiplied by the propellant gas velocity normal to the surface (which for a given formulation is fixed by burning rate and pressure alone), these distances are fixed for a given formulation at a given burning rate and pressure independent of the crossflow velocity. Of course, since crossflow velocity affects burning rate at a given pressure through its influence on the diffusion process as discussed below,  $L_I$  and  $L_{\text{Kin}}$  are influenced through the change in burning rate, but this is simply coupled into a model by expressing  $L_I$  and  $L_{\text{Kin}}$  as explicit functions of burning rate and pressure in that model. The important point is that they can be expressed as functions

of these two parameters alone for a given propellant. However, the distance of the mixing zone from the propellant surface is directly affected by the crossflow. It may be shown through geometrical arguments coupled with the columnar diffusion flame height analysis presented by Schultz, Penner and Green (4), that  $L_{Diff}$  measured along a vector coincident with the resultant crossflow and transpiration velocities should be approximately the same as  $L_{Diff}$  in the absence of a crossflow at the same burning rate and pressure (except at very high ratios of local crossflow velocity to transpiration velocity). That is, the magnitude of  $L_{Diff}$  is essentially independent of the crossflow velocity although its orientation is not. Thus, the distance from the surface to the "average" mixed region is decreased to  $L_{Diff} \sin \theta$  where  $\theta$  represents the angle of the average flow vector in the mixing region. (See Figure II-1.) The heat balance at the propellant surface now yields:

$$r \propto \dot{q}_{feedback} \propto \frac{k_1(T_{AP} - T_s)}{L_I} + \frac{k_2(T_f - T_s)}{L_{Diff} \sin \theta + L_{Kin}} \quad (6)$$

This picture has been used as the basis of development of a first generation flame bending model for prediction of burning rate versus pressure curves at various crossflow velocities, given only a curve of burning rate versus pressure in the absence of crossflow. This model employs no empirical constants other than those obtained from regression analysis of the no-crossflow burning rate data. Thus, although it is not as powerful as a model which would permit prediction of erosive burning phenomena with no burning rate data at all (but only propellant composition and ingredient size data), it is still a very useful tool, in that it permits prediction of erosive burning characteristics given only relatively easily obtained strand-bomb burning rate data. (By comparison, the Lenoir and Robillard model employs two free constants which are adjusted to provide a best fit of erosive burning data for a given propellant and since these constants vary from propellant to propellant, the Lenoir and Robillard model does not permit a priori erosive burning predictions for

new propellants without some erosive burning data, whereas the first generation model developed on this program does not require such data.

The general approach followed in development of this model was:

1. Derive expressions for  $L_I$ ,  $L_{Diff}$ , and  $L_{Kin}$  as functions of burning rate (or burning mass flux,  $\dot{m}_{burn}$ ), pressure, and propellant properties and substitute these into a propellant surface heat balance.
2. Work the resulting equation into the form:

$$r_o = A_3 P \left[ 1 + \frac{A_4}{1 + A_5 d_p^2 P^2} \right]^{1/2} \quad (7)$$

$r_o$  = burning rate in absence of crossflow

$P$  = pressure

$d_p$  = particle size of oxidizer (diameter)

$A_3, A_4, A_5$  = empirical constants

for burning in the absence of crossflow and perform a regression analysis using no-crossflow burning rate data to obtain best fit values for  $A_3, A_4,$  and  $A_5$ . ( $d_p$  is the average ammonium perchlorate particle size. For a given propellant, the burning rate data may be just as effectively regressed on  $A_3, A_4$  and  $A_5 d_p^2$ , eliminating the necessity of actually defining an effective average particle size.)

3. From these results, obtain expressions for  $L_I, L_{Diff}$ , and  $L_{Kin}$  as functions of burning rate (or  $\dot{m}_{burn}$ ) and pressure.
4. Combine these expressions with an analysis of the boundary layer flow which gives the crossflow velocity as a function of distance from the propellant surface, mainstream velocity, and propellant burning rate, to permit calculation of the angle  $\theta, L_I, L_{Diff}, L_{Kin}$ , and  $\dot{m}_{burn}$  for a given pressure and crossflow velocity.

Detailed equation development for this model is presented in Reference 13. Initial testing of the model was carried out using a systematic erosive burning data set taken by Saderholm (2). (This was the only systematic erosive burning data set found in the literature with sufficient zero crossflow data to permit evaluation of  $A_3$ ,  $A_4$ , and  $A_5 d_p^2$ .) Results are presented in Figure II-2. As may be seen, agreement between experiment and theory is excellent over a wide range of pressure and crossflow velocities. Further testing of this model against data obtained in the experimental part of this program (described below) is presented later in this report.

### 3. Second Generation Model

As indicated above, the first generation model does require as input burning rate versus pressure data with no crossflow (i.e., strand data) for each propellant for which erosive burning predictions are to be made. A more fundamental model (with explicit calculation of the distances of flames from the surface rather than inference of these distances from zero crossflow data) of the propellant combustion process which would permit prediction of burning rate versus pressure with or without crossflow, given only propellant composition and ingredient size data, is highly desirable. During the second year of this program, this author has been working on development of such a model for the rather limited case of propellants containing unimodal ammonium perchlorate oxidizer and no metal additives (with plans to extend this model later to treat multimodal oxidizer and metallized propellant cases). The first thought was to simply modify the Beckstead-Derr-Price (BDP) model (32) for prediction of burning rates of composite propellants as a function of pressure (in the absence of crossflow) to allow for bending of the diffusion flame(s) considered in that model. However, upon careful review of the BDP model, this author found sufficient problems and areas of disagreement with that model that it was decided to develop an entirely new composite propellant combustion computer code (embodying many of the BDP concepts, while modifying or replacing others) with the flame-bending mechanism described in the preceding section embedded in the mathematical analysis. Major modifications to the BDP model included are:

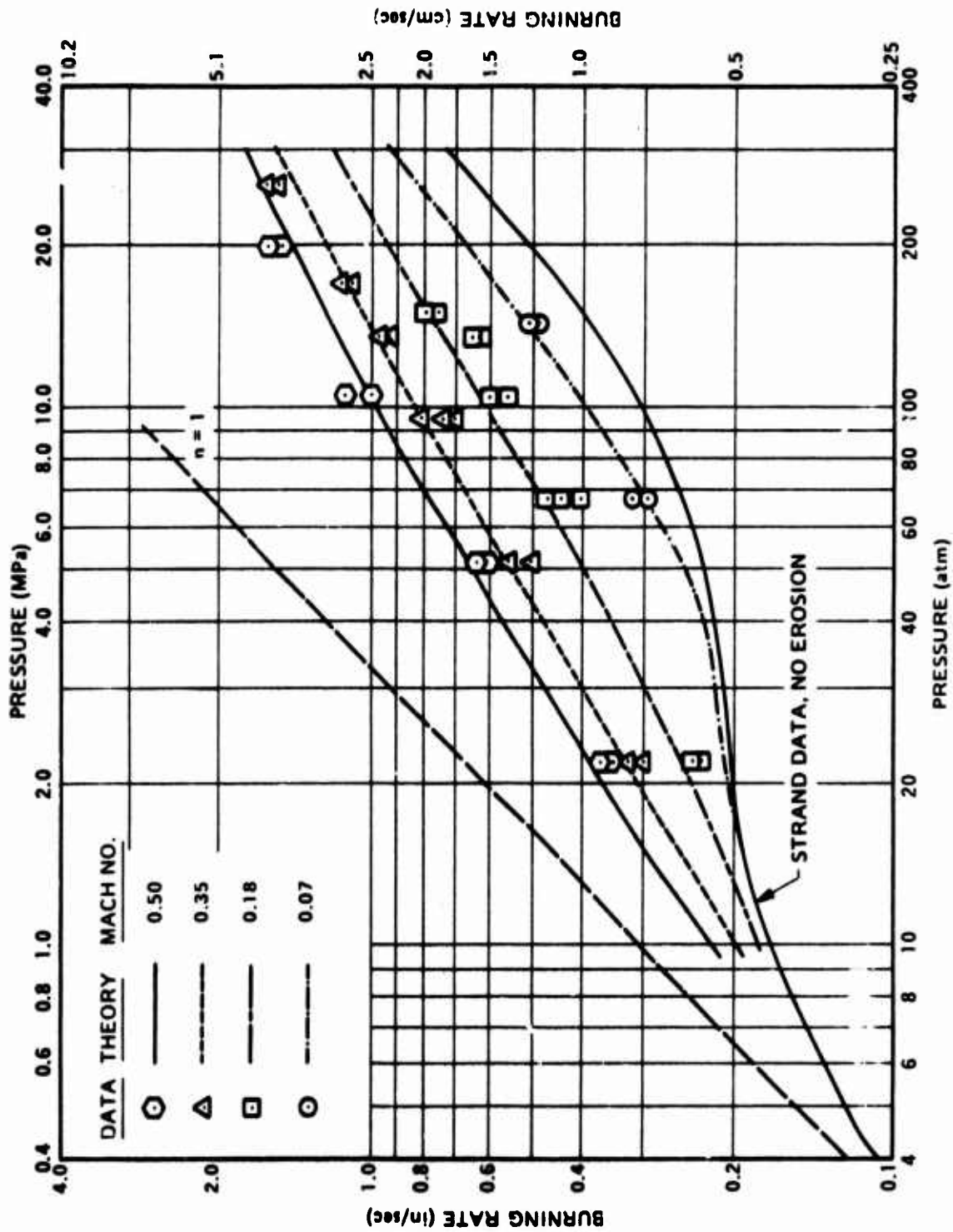


Figure 11-2. Erosive Burning Model Predictions and Comparisons with Saderholm Data. Transpiration Effects Included.

- 1) Variation in the ratio of local oxidizer-surface intersectional area to the binder surface area as the propellant surface regresses past an oxidizer particle is considered. (In the BDP model, a geometrical average ratio is used; this involves an assumption that a lot of very nonlinear processes can be linearly averaged.)
- 2) The kinetics of subsurface/surface exothermic reactions are considered, with use of rate expressions based upon the work of Waesche and Wenograd (33). (In the BDP model, subsurface/surface heat release is included with the endothermic ingredient vaporization heats, with the resultant implicit assumption that the amount of heat release in these reactions per unit mass of propellant is independent of such parameters as burning rate.)
- 3) A correction of an inconsistency in definition of areas in the BDP model is made.
- 4) The calculation of the dimensionless stoichiometric group needed for calculation of the diffusion flame height via the Burke-Schumann (34) analysis is modified. (The group used in the BDP model is inconsistent with that defined in the original work of Burke-Schumann.)
- 5) A two-flame (fuel-gas/oxidizer-gas columnar diffusion flame and ammonium perchlorate monopropellant flame), rather than a three-flame model, is used. (With correction of the calculation of the stoichiometry dimensionless group for the Burke-Schumann analysis, it no longer appears necessary to differentiate between the parts of the diffusion flame inside and outside of an ammonium perchlorate monopropellant flame.)
- 6) The procedure for calculation of heat feedback from the diffusion flame and the AP monopropellant flame is modified. (In the BDP model, all flames are considered to occur in flame sheets at discrete distances from the surface: in the current model, the AP monopropellant heat release is treated as a flame-sheet type heat release, but the diffusion flame heat release is considered to occur over a finite range of distances from the propellant surface.)

- 7) The distance associated with oxidizer-binder gas interdiffusion in the presence of crossflow is assumed to be reduced by a factor,  $\sin \theta$ , where  $\theta$  is the angle of the resultant of the crossflow and transpiration velocities relative to the surface, as in the first generation model.

A major assumption made in the BDP model (and variants thereof) is that one may work in terms of an average oxidizer-fuel ratio for a given size oxidizer particle. In reality, however, an oxidizer particle and the fuel surrounding it (and associated with it) will be receiving heat feedback from a diffusion flame of strongly varying oxidizer/fuel ratio during its burning. As the oxidizer particle first becomes exposed to the surface, with only its tip showing, the local oxidizer-fuel ratio will be quite low. As the burning surface passes the equator of the particle, however, the oxidizer-fuel ratio will be comparatively high, and as the particle burns out, the ratio will again be low. Implicit in the BDP use of an "average" oxidizer-surface planar intersectional area is the assumption that all of the highly non-linear dependencies of burning rate, flame temperature, and consequently heat feedback from the diffusion flame can be linearly averaged over the range of the variations during regression of the propellant surface through the oxidizer. Things may work out this way, but this appears to this author to be a somewhat risky a priori assumption. Accordingly, in this model (limited thus far to unimodal oxidizer) an attempt is made to allow for the variation in local oxidizer/fuel ratio associated with the burning of an individual oxidizer particle due to the variation in relative oxidizer-fuel surface intersectional areas as the surface regresses through the particle.

In deciding how to treat this variation (or, indeed, whether to treat it) one must first address the question of propellant surface and subsurface response to variation in heat feedback flux from the varying oxidizer/fuel gas-phase diffusion flame. If the burning rate response is very slow, such variations in feedback flux are damped out and the averaging procedure of BDP is probably adequate. If, on the other hand, response of burning rate variations to heat feedback flux variations is sufficiently fast, one may use quasi-steady state calculations of the burning

rate at each fuel/oxidizer area ratio during the regression of the burning surface through the particle and then properly average these to arrive at an average burning rate. In between these extremes lies great difficulty. A transient heat conduction program allowing for surface ablation was employed to examine the response of ablation rate to variation in heat flux to the surface. Variations in heat flux up to  $10^6 \text{ cal/cm}^2 \text{ sec}^2$  (corresponding to approximate doubling of heat feedback flux from a typical steady-state value in 0.50 msec, the time required for a propellant burning at 2 cm/sec to regress 10 microns) were examined. In all cases, the burning rate response was found to track the feedback flux variation within 10 percent. Accordingly, it was concluded that use of a quasi-steady-state approach to calculation of propellant burning rate at various oxidizer/fuel ratios associated with different intersections of the propellant burning surface with a given oxidizer particle would not be seriously in error.

As mentioned earlier, this second generation model is presently limited to unimodal oxidizer particle size. Having concluded that one can use a quasi-steady-state approach to calculating burning rate as a function of the ratio of planar areas of oxidizer and associated fuel intersected by the regressing surface, one is next faced with the question of how to calculate the distribution of these areas. Since composite propellants are normally quite highly loaded with solid oxidizer in the rubber fuel binder, and since with unimodal oxidizer propellants the desire for these high loadings tends to lead to loadings approaching maximum theoretical loading, it was decided that as a reasonable approximation, one might assume a regular packing of oxidizer crystals in the binder corresponding to the arrangement of a cubic closest packing array, though with the spacing larger than that for a true cubic closest packing, corresponding to less than 100 percent of theoretical maximum loading. Simple geometrical considerations then permit one to calculate the characteristic lattice dimension  $D_1$  (where lattice spacings in three mutually orthogonal planes are given by  $D_1$ ,  $0.866 D_1$ , and  $0.82 D_1$ ) as:

$$D_1 = \left( \frac{0.737}{VLO} \right)^{1/3} D_o = \left( \frac{0.737 [WFO/\rho_{ox} + (1 - WFO)/\rho_F] \rho_{ox}}{WFO} \right)^{1/3} D_o \quad (8)$$

VLO = volumetric fraction oxidizer in propellant

$D_o$  = oxidizer diameter

WFO = weight fraction oxidizer in propellant

$\rho_{ox}$  = oxidizer density (1.95 gm/cm<sup>3</sup> for ammonium perchlorate)

$\rho_f$  = fuel (binder) density (0.92 gm/cm<sup>3</sup> for HTPB or CTPB binders)

It is arbitrarily assumed that the propellant burns in the direction in which the planes of oxidizer are separated by  $0.82 D_1$ . This distance is broken up into equally spaced increments and straightforward geometrical relations are then used to calculate the planar intersection area of the burning surface with the oxidizer (APOX) and its associated fuel planar area (AFU) at each of the intersection planes, with the assumption that wherever two layers of oxidizer overlap the fuel is apportioned between them in the ratio of their planar surface intersection areas. The result of these calculations is a table of planar oxidizer-surface intersectional area (APOX) and associated fuel surface area (AFU) versus distance of the intersection plane from the top of the particle (XDTOP). Results of a typical calculation are presented in Table II-III. Burning rates for each of these conditions (starting at the top of the particle since one must allow for different regression rates of fuel and oxidizer) are then calculated as described below and an averaging procedure, also described below, is then used to calculate the propellant burning rate.

Next let us address the question of calculation of propellant burning rate at each of the conditions defined by the various distances of the burning surface intersection plane from the top of the oxidizer particle, as listed for the example in Table II-III. First, since as mentioned above, different oxidizer and fuel regression rates are to be allowed, one must address rather carefully the questions of surface geometry and mass conservation at the surface. In this model, as in the BDP model, the fuel is assumed to regress in a planar manner, and the oxidizer-fuel surface is forced to be continuous at their intersection. These restrictions, coupled with the fact that the linear regression rates of fuel and oxidizer parallel to their directions of regression are allowed to differ, force the oxidizer surface to assume a curved shape as it regresses. Oxidizer

TABLE II-III. Variation of Oxidizer Planar Surface Intersection Area and Associated Fuel Surface Area with Distance of Intersection Plane from Top of the Particle - Typical Case

Particle Diameter = 20 microns  
 Weight Fraction Oxidizer = 0.73  
 Oxidizer Density = 1.95 gm/cm<sup>3</sup>  
 Binder Density = 0.92 gm/cm<sup>3</sup>  
 Volumetric Oxidizer Loading = 56.05 percent  
 D<sub>1</sub> = 21.91 microns

<u>Increment Number</u>	<u>XDTOP Distance from Top of Particle (microns)</u>	<u>APOX Planar Oxidizer Intersectional Area (microns)<sup>2</sup></u>	<u>AFU Planar Fuel Area (microns)<sup>2</sup></u>
1	0.119	7.4	19.1
2	1.017	60.6	147.2
3	1.915	108.8	280.4
4	2.813	151.9	263.8
5	8.712	18.19	225.8
6	4.610	222.9	192.8
7	5.508	250.8	165.0
8	6.407	273.6	142.1
9	7.305	291.3	124.4
10	8.203	304.0	111.7
11	9.101	311.6	104.1
12	10.0	314.2	101.5
13	10.899	311.6	104.1
14	11.797	304.0	111.7
15	12.695	291.3	124.4
16	13.593	273.6	142.1
17	14.492	250.8	165.0
18	15.390	222.9	192.8
19	16.288	189.9	225.8
20	17.187	151.9	263.8
21	18.085	108.8	280.4
22	18.983	60.6	147.2
23	19.881	7.4	19.1

mass fluxes may be expressed relative to either the actual curved surface area or the planar projection of this area, the two values being related by:

$$\dot{m}_{\text{ox,p}} (\text{APOX}) = \dot{m}_{\text{ox,s}} (\text{ASOX}) = \frac{r_{\text{ox}}}{\rho_{\text{ox}}} (\text{ASOX}) \quad (9,9a)$$

$\dot{m}_{\text{ox,p}}$  = oxidizer mass flux, based on planar surface projection

$\dot{m}_{\text{ox,s}}$  = oxidizer mass flux, based on actual total curved surface area

APOX = planar projection of oxidizer surface area

ASOX = total curved oxidizer surface area

$r_{\text{ox}}$  = linear regression rate of oxidizer, normal to its surface

$\rho_{\text{ox}}$  = oxidizer density

The average mass flux of fuel and oxidizer normal to the mean regression plane is given by:

$$\dot{m} = \frac{\dot{m}_{\text{fuel}} (\text{AFU}) + \dot{m}_{\text{ox,p}} (\text{APOX})}{\text{AFU} + \text{APOX}} = \frac{\dot{m}_{\text{fuel}} (\text{AFU}) + \dot{m}_{\text{ox,s}} (\text{ASOX})}{\text{AFU} + \text{APOX}} \quad (10)$$

It is important to know the value of ASOX at each plane since the Arrhenius expression relating oxidizer mass flux to surface temperature must be written in terms of  $\dot{m}_{\text{ox,s}}$  to be meaningful:

$$\dot{m}_{\text{ox,s}} = B_{\text{ox}} \text{ ex } (-E_{\text{ox}}/RT_s) \quad (11)$$

$B_{\text{ox}}$  = pre-exponential rate factor

$E_{\text{ox}}$  = activation energy of oxidizer surface ablation reaction

$T_s$  = surface temperature

A similar expression for the fuel pyrolysis rate:

$$\dot{m}_{\text{fuel}} = B_{\text{fuel}} \exp(-E_{\text{fuel}}/RT_s) \quad (12)$$

enables one to calculate the ratio of oxidizer and fuel regression rates as a function of surface temperature:

$$\frac{r_{\text{ox}}}{r_{\text{fuel}}} = \frac{\dot{m}_{\text{ox},s} \rho_{\text{fuel}}}{\dot{m}_{\text{fuel}} \rho_{\text{ox}}} = \frac{\rho_{\text{fuel}} B_{\text{ox}} \exp(-E_{\text{ox}}/RT_s)}{\rho_{\text{ox}} B_{\text{fuel}} \exp(-E_{\text{fuel}}/RT_s)} \quad (13)$$

There is considerable uncertainty as to best values to be used for  $B_{\text{ox}}$ ,  $B_{\text{fuel}}$ ,  $E_{\text{ox}}$ , and  $E_{\text{fuel}}$ : thus, parametric study of the effects of these values is required. Note that it has been assumed here that the oxidizer and fuel surface temperatures are equal. This is probably not a particularly good assumption, but relaxing it requires a rather complex three-dimensional heat transfer analysis.

Now, how does one go about calculating ASOX for succeeding regression intervals through the oxidizer particle? First, it is assumed (approximated) that at the first increment after the tip of the particle becomes exposed (in Table II-III, when the distance from the top of the particle is 0.119 microns) the oxidizer surface is planar. The procedure outlined below for calculation of burning rate, given the local oxidizer/fuel area ratio, is then used to calculate the oxidizer and fuel linear regression rates under the conditions given for this first increment. The fuel regression rate is then used to calculate the time for the regressing fuel to reach the second increment (distance from the initial particle top of 1.017 microns in Table II-III) as:

$$\text{TAU}_2 = (\text{XDTOP}_2 - \text{XDTOP}_1)/r_f \quad (14)$$

The distance which the center of the AP particle peak regresses in that time is then calculated as:

$$\Delta(\text{DELOX}) = r_{\text{ox}}(\text{TAU}_2) \quad (15)$$

Similar procedures are followed for each succeeding increment, yielding for each XDTOP (distance of fuel surface from the initial top of the oxidizer particle) a value of DELOX (distance of the center of the oxidizer surface from the initial top). The geometrical method depicted in Figure II-3 (for a case where the oxidizer regresses more slowly than the fuel) is then used to calculate ASOX at each calculational increment. Applying the Pythagorean Theorem to the larger triangle and using  $|H| = |XDTOP - DELOX|$ ,

$$2R_1 |XDTOP - DELOX| = A^2 + (XDTOP - DELOX)^2 \quad (16)$$

while similar analysis of the smaller triangle yields:

$$A^2 = D_o (XDTOP) - XDTOP^2 \quad (17)$$

Elimination of A from these equations and use of  $ASOX = 2\pi R_1 |XDTOP - DELOX|$  then gives:

$$ASOX = \pi [(XDTOP)D_o - 2(XDTOP)(DELOX) + DELOX^2] \quad (18)$$

For the calculation of the columnar diffusion flame between fuel gases from the binder pyrolysis and oxidizer gases from the oxidizer decomposition (discussed later) several other parameters associated with the surface configuration of the oxidizer particle-associated fuel combination at each increment must be calculated. First, the combined radius of the oxidizer and binder gas streams (in this model, a modified Burke-Schumann analysis with a fuel annulus surrounding an oxidizer gas core is employed for the columnar diffusion flame calculation) is calculated as:

$$R_{BS} = \sqrt{(AFU + APOX)/\pi} \quad (19)$$

$R_{BS}$  = outer radius of fuel annulus

In line with the requirement in the Burke-Schumann analysis that the linear velocity of the fuel and oxidizer streams have the same initial

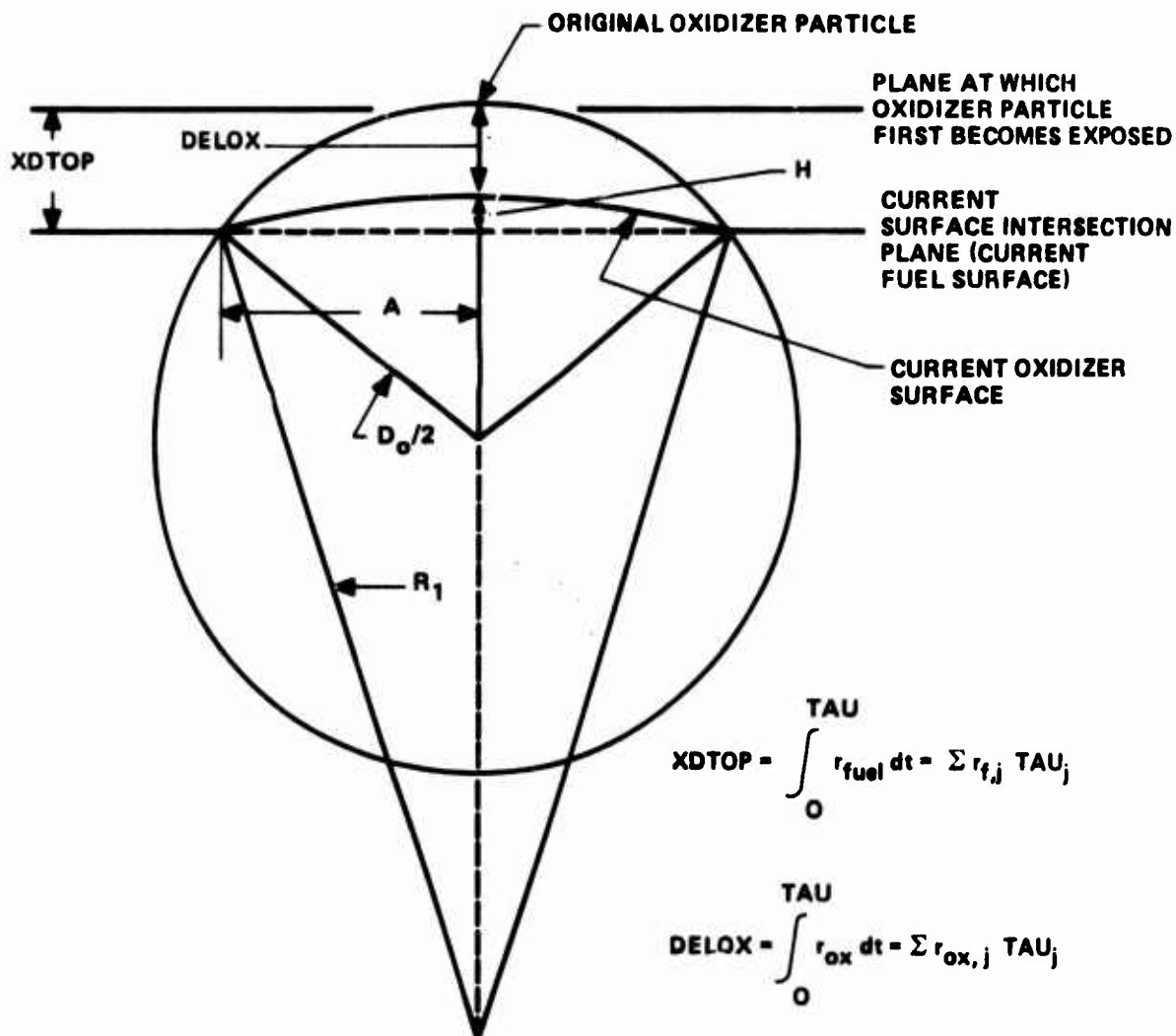


Figure II-3. Schematic Demonstrating Calculation of Oxidizer Surface Area at Some Time, TAU, After First Exposure of the Top of the Oxidizer Particle.

value, the oxidizer and fuel gas streams leaving the surface are assumed to adjust their areas quickly from the planar areas of the solids to meet this requirement. Since the temperature at the surface is assumed to be the same for the fuel and oxidizer, and pressures are equal, this leads to an expression for the radius of the inner oxidizer gas jet of:

$$L_{BS} = R_{BS} \left/ \left( 1 + \frac{\dot{m}_{fuel} (AFU) (MW)_{ox}}{\dot{m}_{ox,s} (ASOX) (MW)_{fuel}} \right)^{1/2} \right. \quad (20)$$

$L_{BS}$  = oxidizer gas column radius

$MW_{ox}$  = molecular weight of oxidizer gases (estimated to be approximately 35 for ammonium perchlorate)

$MW_{fuel}$  = molecular weight of fuel pyrolysis gases (estimated to be approximately 19 for CTPB or HTPB binder)

The linear gas velocity away from the surface, also required in the modified Burke-Schumann analysis, as well as for calculation of characteristic reaction distances (products of reaction times and this velocity) is calculated as:

$$v_{gas,surf} = \frac{\dot{m}_{ox,s} (ASOX) RT_{surf}}{(MW)_{ox} \pi (L_{BS})^2 P} \quad (21)$$

$v_{gas,surf}$  = gas velocity away from propellant surface

$P$  = pressure

Finally, the ratio of the molar fuel/oxidizer ratio to stoichiometric molar fuel/oxidizer ratio for the combined fuel and oxidizer streams ( $\phi$ ), also required in the modified Burke-Schumann analysis, is calculated as:

$$\phi = \frac{C_2}{iC_1} \frac{R_{BS}^2 - L_{BS}^2}{L_{BS}^2} \quad (22)$$

$C_2$  = initial concentration of fuel in the binder pyrolysis product gases

$C_1$  = initial net (excess of oxidizer over fuel molecules) concentration of oxidizer in the oxidizer decomposition product gases

$i$  = stoichiometric moles of fuel per mole of oxidizer.

Since the initial pressure and temperature of the fuel and gas streams are the same, the concentration ratio  $C_2/C_1$  may be replaced by a ratio of mole fractions  $Y_2/Y_1$ . The mole fraction of fuel in the binder pyrolysis products for HTPB and CTPB binder systems in the absence of subsurface reactions depleting some of this fuel (as discussed later) is approximately 0.96, while the initial net mole fraction of oxidizer molecules in the decomposition products of ammonium perchlorate is approximately 0.28. For an HTPB/AP or CTPB/AP system, the stoichiometric moles of fuel per mole of oxidizer are about 0.6, calculated on the basis of  $H_2O$ ,  $CO_2$  stoichiometry. (These calculations, as well as the calculations of molecular weights for ammonium perchlorate and HTPB decomposition gas streams mentioned earlier are based on HTPB binder yielding approximately 0.16 moles  $CO$ , 0.03 moles  $N_2$ , and 5.0 moles  $C_{1.4}H_{2.1}$  per 100 grams; and AP yielding approximately 5 moles  $H_2O$ , 2 moles  $NH_3$ , 2 moles  $ClO_3$ , 1 mole  $HClO_4$ , 1 mole  $HCl$ , 1 mole  $N_2O$ , 1.5 moles  $O_2$ , 0.5 moles  $Cl_2$ , 1 mole  $NO$ , and 1 mole  $H_2$  per 585 grams.) With subsurface reactions, the fuel mole fraction is reduced by a factor  $(1 - \beta)$  while the oxidizer mole fraction is reduced by a factor  $(1 - \alpha)$  where  $\beta$  is the fraction of fuel consumed in subsurface reactions and  $\alpha$  is the fraction of oxidizer consumed in these reactions. (See later discussion.) With these substitutions, Equation 22 becomes:

$$\phi = \frac{Y_{2,o}(1 - \beta)(R_{BS}^2 - L_{BS}^2)}{1 Y_{1,o}(1 - \alpha) L_{BS}^2} \quad (23)$$

$Y_{2,o}$  = mole fraction of fuel in binder-pyrolysis products in absence of subsurface reactions

$Y_{1,o}$  = mole fraction of oxidizer in oxidizer decomposition products in absence of subsurface reactions.

The burning rate of the propellant at any given set of oxidizer/fuel conditions (any regression increment) is controlled by heat releases (exothermic reactions) at various locations. In this model, we consider three principal heat release zones: (1) heat release in a thin subsurface zone quite near (and including) the propellant surface; (2) heat release in the gas-phase above the propellant from ammonium perchlorate decomposition

products burning as a monopropellant; and (3) heat release from a diffusion flame between AP decomposition (and monopropellant flame) products and fuel vapor released by binder pyrolysis.

The subsurface/surface heat release is calculated by an iterative process, coupled with the remainder of the model, in which an estimate of the subsurface temperature profile is made and substituted into an Arrhenius rate expression representing subsurface heat release rate data measured by Waesche and Wenograd (33), which is then integrated from the surface into the propellant to obtain the total subsurface heat release per unit mass of propellant. This procedure differs quite a bit from that of the BDP model, in which the amount of subsurface heat release per unit mass of propellant is assumed to be a constant, independent of such parameters as burning rate, and is included with the binder heat of vaporization. Since the subsurface temperature profile steepens rapidly with increasing burning rate, our procedure results in the subsurface heat release per unit mass of propellant decreasing with increasing rate. As will be discussed later, the surface energy balance in this model is written with the surface area of the oxidizer and associated fuel as the basis: thus all terms appear in the units of energy/time. For bookkeeping convenience, the surface/subsurface heat release term is written as:

$$\dot{q}_{\text{sub}} = \dot{m}_{\text{ox},s} (A_{\text{SOX}}) Q_{\text{EXO}} \alpha \quad (24)$$

$\dot{q}_{\text{sub}}$  = heat release via subsurface reactions, energy/time

$Q_{\text{EXO}}$  = heat release per unit mass of oxidizer consumed in surface/subsurface reactions

$\alpha$  = mass fraction of oxidizer which reacts at or below the surface

For an AP-HTPB binder system,  $Q_{\text{EXO}}$  is approximately 1150 calories per gram of oxidizer. It is assumed that a stoichiometric amount of fuel is reacted with the oxidizer in these surface/subsurface reactions. Thus the fraction of fuel reacted in these reactions,  $\beta$ , is given by:

$$\beta = \text{SMRBO} \frac{\dot{m}_{\text{ox},s} \text{ (ASOX)}}{\dot{m}_{\text{fuel}} \text{ (AFU)}} \alpha \quad (25)$$

SMRBO = stoichiometric ratio (mass) of binder to oxidizer  
(0.111 for HTPB/AP or CTPB/AP systems)

$\dot{m}_{\text{fuel}}$  = mass flux of fuel

AFU = fuel surface area

Based upon Waesche and Wenograd subsurface reaction rate data, the fraction of oxidizer reacted per unit time is given for AP/CTPB systems as a function of temperature by:

$$R_{\alpha} = B_{\text{Sub}} \exp(-E_{\text{sub}}/RT) \quad (26)$$

$$B_{\text{sub}} = 5.1(10)^{12}/D_{\text{O}} \text{ for } D_{\text{O}} > 20\mu$$

$$B_{\text{sub}} = 2.55(10)^{11} \text{ for } D_{\text{O}} < 20\mu$$

$D_{\text{O}}$  = oxidizer particle diameter in microns

$B_{\text{sub}}$  = pre-exponential for subsurface reaction rate equation

$E_{\text{sub}}$  = activation energy for subsurface reaction rate equation

T = temperature

The unperturbed (uncoupled) subsurface temperature profile is given by:

$$T = (T_{\text{s}} - T_{\text{O}}) \exp(r_{\text{ox}} \rho_{\text{ox}} C_{\text{pox}} x / \lambda_{\text{ox}}) + T_{\text{O}} \quad (27)$$

$T_{\text{s}}$  = surface temperature

$T_{\text{O}}$  = propellant bulk temperature

$r_{\text{ox}}$  = linear regression rate of oxidizer

$\rho_{\text{ox}}$  = oxidizer density (1.95 gm/cm<sup>3</sup> for ammonium perchlorate)

$C_{\text{pox}}$  = oxidizer heat capacity (approximately 0.4 cal/gm °K for AP)

$\lambda_{\text{ox}}$  = oxidizer thermal conductivity (approximately 0.001 cal/cm sec °K for AP)

x = distance from surface (sign convention such that it is negative below the surface).

Substitution of Equation 27 into Equation 26 and integration of:

$$\alpha = \int_{x=0}^{x=x'} \frac{R_{\alpha} dx}{r_{ox}} \quad (28)$$

$x'$  = distance below surface (sign convention such that it is negative) at which reaction rate drops to  $\sim 1$  percent of its surface value

yields, with use of the approximation  $e^{-u} \approx 1 - u$ , in Equation 27 and  $x' \approx -0.25 \lambda_{ox} / r_{ox} \rho_{ox} C_{pox}$ :

$$\alpha \approx \frac{B_{sub} \lambda_{ox} e^{-E_{sub}/RT_s} RT_s^2 [1 - e^{-0.25E_{sub}(T_s - T_o)/RT_s^2}]}{r_{ox}^2 \rho_{ox} C_{pox} E_{sub} (T_s - T_o)} \quad (29)$$

Thus Equation 29 relates the mass fraction of oxidizer reacting exothermically at or below the surface to the surface temperature and linear regression rate of the oxidizer and may be used in an iterative procedure with the surface energy balance given later and Equation 11 to solve for all three quantities.

As regards gas-phase heat release zones, a two-flame approach was chosen for this model, the two flames being an AP monopropellant flame and a columnar diffusion (Burke-Schumann) flame. The reasons that a two-flame rather than a three-flame model (as the BDP) was chosen were:

- 1) Mathematical simplification.
- 2) Lack of apparent difference in a diffusion flame between AP decomposition products and fuel and a flame between AP monopropellant flame products and fuel. In both cases, the overall stoichiometry is the same since, while AP decomposition products bring more oxidizer into a binder fuel stream than do AP monopropellant flame products, they also bring more fuel, with the result that the overall mixture ratio at a given point is nearly the same.

- 3) Provisions were made in calculation of the AP monopropellant heat release to allow for consumption of reactants for that flame in that part of the columnar diffusion flame which occurred inside the AP flame.

Three distance parameters are important in calculating heat feedback from these gas flames to the propellant surface. These are pictured in Figure II-4. These distances are  $FH90 \sin \theta$ ,  $L_{AP}$  and  $L_{RX}$ .  $FH90$  refers to the distance associated with completion of 90 percent of the mixing of fuel and oxidizer gas products. (If there were no reaction delay, this would be equivalent to the 90 percent heat release point.)  $L_{RX}$  refers to the reaction distance associated with the binder gas-oxidizer gas flame, and  $L_{AP}$  refers to the reaction distance associated with the monopropellant AP product flame (both being characteristic times divided by the gas velocity away from the surface as in the first generation model.) As before, flame bending is assumed to reduce the distance to the end of the columnar diffusion heat release (90 percent point) by reducing  $FH90$  to  $FH90 \sin \theta$ , measured perpendicular to the surface.  $FH90$  is calculated as a function of various parameters using a modified Burke-Schumann analysis as described below. A series of calculations of  $FH90$  as a function of these parameters were generated externally and correlations of the results were used in the final program. In this model, it is assumed that the fraction of planar projection of surface,  $APOX/(APOX + AFU)$  receives flux from both the AP and columnar diffusion flames (the latter at the adiabatic flame temperature,  $T_f$ , which is a function of the oxidizer/fuel ratio,  $\dot{m}_{ox,s} [ASOX]/\dot{m}_{fuel} [AFU]$ ) while the remaining fraction of the surface receives flux only from this diffusion flame; however, these fluxes are assumed to smear out uniformly in the propellant. Thus, the total heat flow from the gas-phase heat release zones is given as:

$$\dot{q}_{gas} = \frac{APOX}{APOX + AFU} (\dot{q}_{series\ flames}) + \frac{AFU}{APOX + AFU} (\dot{q}_{diffusion\ flame}) \quad (30)$$

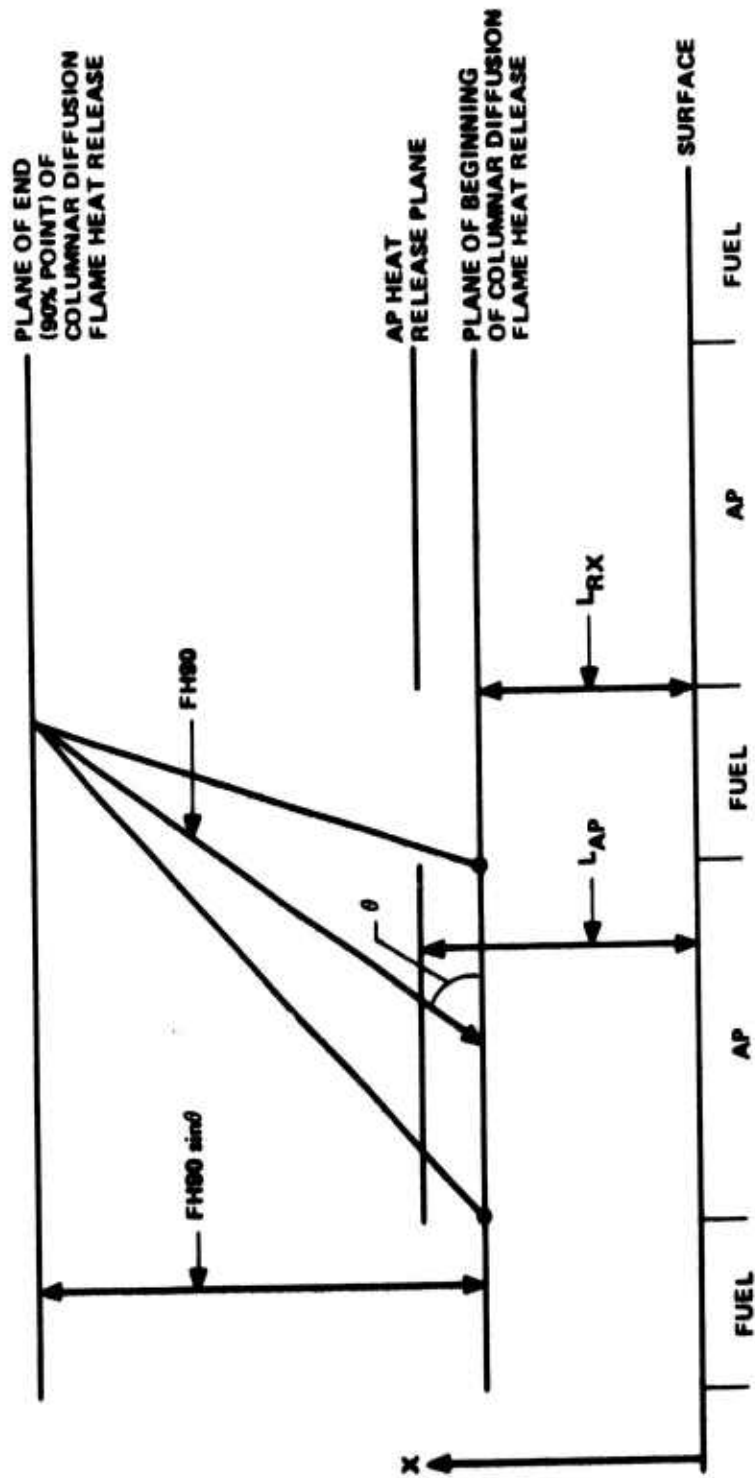


Figure 11-4. Schematic Showing Key Dimensions Relating to Gas-Phase Heat Release.

Heat release from the AP monopropellant flame is assumed to be a planar one, resulting in a discontinuity in the temperature derivative at its point of release, while the columnar diffusion flame is assumed to release its heat uniformly between  $x = L_{RX}$  and  $x = L_{RX} + FH90 \sin \theta$ . Actually, it would be better (more physically realistic) to assume different uniform heat releases in the  $L_{RX} < x < L_{AP}$  and the  $L_{AP} < x < L_{RX} + FH90$  regions with the difference related to the heat release at the AP reaction plane. Sample calculations, however, indicate that the effect on predicted burning rates is small, while the added complexity of this approach is considerable. With use of multiple algebraic manipulations, we arrive at the following expressions for the heat fluxes at the surface (allowing for reduction of reactants available for the AP monopropellant reaction by occurrence of some diffusion flame reaction closer to the surface):

$$\dot{q}_{\text{diffusion flame}} = \frac{\dot{m} C_p (T_f - T_s)}{(e^{z_1} - 1)} \left[ 1 - \frac{e^{z_1} \left\{ 1 - \frac{\lambda}{\dot{m} C_p FH90 \sin \theta} (e^{z_2} - 1) \right\}}{e^{z_1} - \frac{\lambda}{\dot{m} C_p FH90 \sin \theta} (e^{z_2} - 1)} \right] \quad (31)$$

$$\dot{q}_{\text{series flames}} = \dot{q}_{\text{diffusion flame}} + \frac{\dot{m} Q_{AP} (1 - \alpha) \left[ 1 - \frac{(L_{AP} - L_{RX})}{FH90 \sin \theta} \right] \left[ \frac{\dot{m} C_p FH90 \sin \theta}{\lambda} e^{z_3} - e^{z_2} + 1 \right]}{\left[ \frac{\dot{m} C_p FH90 \sin \theta}{\lambda} e^{z_1} - e^{z_2} + 1 \right]} \quad (32)$$

$$z_1 = \dot{m} C_p (L_{RX} + FH90 \sin \theta) / \lambda$$

$$z_2 = \dot{m} C_p FH90 \sin \theta / \lambda$$

$$z_3 = \dot{m} C_p (FH90 \sin \theta + L_{RX} - L_{AP}) / \lambda$$

$\dot{m}$  = average surface mass flux (based on planar area)

$C_p$  = gas heat capacity (function of oxidizer/fuel ratio as discussed later)

$T_f$  = flame temperature

$T_s$  = surface temperature

$\lambda$  = thermal conductivity of gas (discussed later)

$Q_{AP}$  = Heat release per unit mass associated with  $HClO_4(g) + NH_3(g) \rightarrow$  Equilibrium Products

$\alpha$  = Fraction of AP reacted below surface

Next, let us consider the calculation of the distances  $L_{RX}$ ,  $L_{AP}$ , and FH90 (and FH90  $\sin \theta$ ). The distance FH90, which is calculated from a modified Burke-Schumann columnar diffusion flame analysis (modified to allow for axial diffusion) is defined as the distance from the starting plane at which 90 percent of the fuel (for oxidizer-rich cases) or 90 percent of the oxidizer (for fuel-rich cases) will be consumed, assuming infinite reaction kinetics. This definition of the characteristic diffusion distance differs from that of the BDP model where the characteristic distance is defined as the distance from the starting plane to the point of closure of the flame over the oxidizer (fuel-rich cases) or the fuel (oxidizer-rich cases). One serious problem with use of the flame closure point to define the characteristic distance is that it has a singularity for stoichiometric situations: that is, for stoichiometric oxidizer-fuel ratio, the flame does not close and this characteristic distance goes to infinity. Since most of the heat is still released fairly close to the surface, this latter definition of a characteristic diffusion distance leads to seriously misleading results as regards heat feedback to the propellant surface at near stoichiometric oxidizer-fuel ratios: at oxidizer-fuel ratios far from stoichiometric, FH90 and the distances associated with flame closure differ only slightly.

While the Burke-Schumann analysis (and its modification allowing for axial diffusion) deals with a central fuel circular jet surrounded by an annular jet of oxidizer, we have here reversed the situation. This does not basically change the analysis, but could lead to confusion regarding nomenclature for anyone comparing equations. The modified Burke-Schumann analysis results in a series expression for the concentration of oxidizer as a function of axial position (distance from the propellant surface) and radial position (distance from the center of the oxidizer particle surface):

$$\frac{C}{C_1} = \left(1 + \frac{\phi L_{BS}^2}{R_{BS}^2 - L_{BS}^2}\right) \frac{L_{BS}^2}{R_{BS}^2} - \frac{\phi L_{BS}^2}{R_{BS}^2 - L_{BS}^2} + \frac{2L_{BS}}{R_{BS}^2} \left(1 + \frac{\phi L_{BS}^2}{R_{BS}^2 - L_{BS}^2}\right) \sum_{n=1}^{\infty} \frac{1}{\mu_n} \frac{J_1(\mu_n L_{BS}) J_0(\mu_n r)}{[J_0(\mu_n R_{BS})]^2} e^{-\left[1 + \left(\frac{2D\mu_n}{v_{gas}}\right)^2\right]^{1/2}} \frac{v_{gas} x}{2D} \quad (33)$$

where:

$\phi$  = (actual molar fuel/oxidizer ratio)/(stoichiometric molar fuel/oxidizer ratio) (It appears that in the BDP analysis the stoichiometric fuel/oxidizer ratio is arbitrarily set equal to 1.0 .)

$L_{BS}$  = oxidizer jet radius

$R_{BS}$  = outer radius of fuel annular jet

$C_1$  = initial concentration of oxidizer in the central oxidizing gas stream

$C$  = oxidizer concentration at any radial position  $r$  and axial position  $x$  (Negative values exist. Physically these represent fuel regions, with the magnitude of  $C$  representing the concentration of oxidizer needed to react stoichiometrically with the fuel at that location.)

$r$  = radial distance from center of oxidizer surface

$x$  = axial distance from propellant surface

$V_{gas}$  = axial gas velocity

$D$  = gas diffusivity (Discussed later.)

$\mu_n$  = nth positive root of  $J_1(\mu_n R_{BS}) = 0$

$J_0$  = zero order Bessel Function

$J_1$  = first order Bessel Function

This equation was programmed for solution for oxidizer concentration as a function of  $r$  and  $x$  for any given set of four independent parameters:  $L_{BS}$ ,  $D/V_{gas}$ ,  $\phi$ , and  $R_{BS}/L_{BS}$ , which may be seen to specify the problem. In this program, the first nine terms of the series expression ( $n = 1 \dots 9$ ) were used. The program also included integration of the profiles from  $r = 0$  to  $r = R_{BS}$  at various values of  $x$  for evaluation of the fraction of the deficient ingredient reacted as a function of  $x$ . (Negative values of  $C$  were set equal to zero, of course, in this integration.) These fractions were then plotted against  $x$  to determine FH90 as a function of the four independent parameters:

$$FH90 = f_1(L_{BS}, D/V_{gas}, \phi, R_{BS}/L_{BS}) \quad (34)$$

An extensive set of calculations covering a wide range of each of these variables was carried out and tabulations and correlations of the results were built into the final combustion model.

The reaction distances,  $L_{RX}$  and  $L_{AP}$ , are calculated as the products of reaction times and gas velocity away from the surface. Using the Zeldovich approach for premixed flame analysis along with several minor approximations which will not be detailed here, we arrive at for the oxidizer-fuel reaction distance,  $L_{RX}$ :

$$L_{RX} = \frac{K_{OF} v_{gas,surf} (1 + \phi)^2 T_f^2 (\exp[E_{ACT,OF}/RT_f])}{P\phi} \quad (35)$$

$E_{ACT,OF}$  = activation energy for the fuel-oxidizer reaction, probably about 11,000 calories/mole for ammonium perchlorate systems based on the data of Powling

$K_{OF}$  = constant including the pre-exponential for the reaction rate term along with several other proportionality constants such as the gas law constant

For the ammonium perchlorate reaction distance, we find, neglecting variation of temperature at the AP heat release site (probably not a very bad approximation due to the low activation energy associated with the ammonia-perchloric acid reaction):

$$L_{AP} = \frac{K_{AP} v_{gas,surf}}{P} \quad (36)$$

$K_{AP}$  = constant including the pre-exponential for the reaction rate term along with several other proportionality constants

(Note that both reactions have been assumed to be second order, as shown by the dependence of the L's on pressure. This assumption could easily be relaxed to treat an nth order reaction by replacing P in the denominator by  $P^{n-1}$ .)

The same approach to calculation of  $\sin \theta$  was used in this model as in the first generation model, <sup>(12,13)</sup> the resulting equations being:

$$U_{gas,x} = FH90 \sin \theta = v_{gas,surf} \frac{T_f}{T_s} \quad (37)$$

$$Y^+ = \frac{10.5(FH90 \sin \theta) (\bar{U}_{\text{crossflow}})^{0.9} T_f^{0.9} P^{0.9}}{D_{\text{channel}}^{0.1} ([T_s + T_f]/2)^{1.8}} \quad (38)$$

$$\left. \begin{aligned} U^+ &= Y^+ \text{ for } Y^+ < 5 \\ U^+ &= -3.05 + 5.00 \ln Y^+ \text{ for } 5 \leq Y^+ \leq 30 \\ U^+ &= 5.5 + 2.5 \ln Y^+ \text{ for } Y^+ > 30 \end{aligned} \right\} \quad (39)$$

$$U_{\text{crossflow},x} = FH90 \sin \theta$$

$$U^+ \left[ \frac{0.023 (\bar{U}_{\text{crossflow}})^{0.9} T_f^{0.18}}{D_{\text{channel}}^{0.1} P^{0.1}} \right] \exp(-60 U_{\text{gas},x} = FH90 \sin \theta / \bar{U}_{\text{crossflow}}) \quad (40)$$

$$\sin \theta = \frac{U_{\text{gas},x} = FH90 \sin \theta}{\sqrt{U_{\text{gas},x}^2 = FH90 \sin \theta + U_{\text{crossflow},x}^2 = FH90 \sin \theta}} \quad (41)$$

$U_{\text{gas},x} = FH90 \sin \theta$  = linear gas flow rate away from propellant at distance  $FH90 \sin \theta$  from the surface

$U_{\text{crossflow},x} = FH90 \sin \theta$  = linear gas crossflow rate at distance  $FH90 \sin \theta$  from the surface

$\theta$  = angle between resultant velocity vector and planar surface (See Figure II-4.)

$Y^+$  = dimensionless value of  $FH90 \sin \theta$

$U^+$  = dimensionless crossflow velocity at  $x = FH90 \sin \theta$

$\bar{U}_{\text{crossflow}}$  = mainstream crossflow velocity

$D_{\text{channel}}$  = flow port hydraulic diameter

As mentioned earlier, the final flame temperature,  $T_f$ , depends on the relative flow rates of fuel and oxidizer gases at each calculational

increment during progression of the propellant surface through the oxidizer. Accordingly, a table of flame temperature calculated with a thermochemical equilibrium program versus a parameter representing the relative flow rates is generated for the propellant system of interest (e.g., HTPB-AP) and included as a tabular look-up in the final program in the form:

$$T_f = f_2 \left( \frac{\dot{m}_{ox,s} \text{ ASOX}}{\dot{m}_{fuel} \text{ AFU}} \right) \quad (42)$$

In addition, the product gas heat capacity is somewhat dependent upon this parameter and an additional tabular look-up, based on thermochemical calculations, of the form:

$$C_p = f_3 \left( \frac{\dot{m}_{ox,s} \text{ ASOX}}{\dot{m}_{fuel} \text{ AFU}} \right) \quad (43)$$

is included.

At this point, we have 26 equations (9, 9a, 10 - 13, 19 - 21, 23 - 25, 29 - 32, 34-43) in 27 unknowns ( $\dot{m}_{ox,p}$ ,  $\dot{m}_{ox,s}$ ,  $r_{ox}$ ,  $\dot{m}$ ,  $\dot{m}_{fuel}$ ,  $T_s$ ,  $r_{fuel}$ ,  $R_{BS}$ ,  $L_{BS}$ ,  $V_{gas, surf}$ ,  $\phi$ ,  $C_p$ ,  $\alpha$ ,  $\beta$ ,  $\dot{q}_{sub}$ ,  $\dot{q}_{gas}$ ,  $\dot{q}_{series \text{ flames}}$ ,  $\dot{q}_{diffusion \text{ flame}}$ ,  $L_{AP}$ ,  $L_{RX}$ ,  $FH90$ ,  $\theta$ ,  $T_f$ ,  $U_{gas,x} = FH90 \sin \theta$ ,  $Y^+$ ,  $U^+$ ,  $U_{crossflow,x} = FH90 \sin \theta$ ). For closure of the problem, we finally write an energy balance at the propellant surface as:

$$\begin{aligned} & \dot{m}_{fuel} \text{ (AFU)} [C_{p,fuel} (T_s - T_o) + Q_{melt,fuel}] + \dot{m}_{fuel} \text{ (AFU)} Q_{fuel \text{ vap}} (1 - \beta) + \\ & \dot{m}_{ox,s} \text{ (ASOX)} [C_{p,ox} (T_s - T_o) + Q_{melt,ox}] + \dot{m}_{ox,s} \text{ (ASOX)} Q_{subl} (1 - \alpha) = \quad (44) \\ & \dot{q}_{sub} + \dot{q}_{gas} \end{aligned}$$

$C_{p,fuel}$  = solid fuel heat capacity (0.3 cal/gm °K for HTPB or CTPB)

$C_{p,ox}$  = solid oxidizer heat capacity (0.4 cal/gm °K for AP)

- $Q_{\text{melt},f}$  = heat of melting of binder (0 for HTPB and CTPB which are assumed not to melt)
- $Q_{\text{melt},ox}$  = heat of melting of oxidizer (30 cal/gm for AP)
- $Q_{\text{melt},vap}$  = heat of pyrolysis of fuel (433 cal/gm, endothermic, for HTPB)
- $Q_{\text{subl}}$  = heat of sublimation of oxidizer (450 cal/gm, endothermic, for AP)

The resulting 27 equations (some of which, as mentioned, are tabular look-ups or correlations of one parameter as a function of others) are solved simultaneously in a computer program for each given set of value of ASOX and AFU associated with each surface regression increment. Among the outputs of each solution are values for  $r_{ox}$  and  $r_{fuel}$  which are used in calculation of ASOX from the known APOX for the succeeding increment via Equations 14 - 18.

In the solution procedure, the thermal conductivity of the gas and the ratio of diffusivity to gas velocity (one of the independent parameters in Equation 34), both proportional to the square root of temperature, are evaluated at the average of the flame and surface temperature.

As mentioned earlier, definitive values for  $B_{ox}$ ,  $E_{ox}$ ,  $B_{fuel}$ , and  $E_{fuel}$  are hard to come by, as are values for the gas-phase reaction pre-exponentials,  $K_{AP}$  and  $K_{OF}$ . In addition, further study of the Waesche and Wenograd data (more of which has been recently received by this author) may result in changes in the pre-exponential and/or activation energy used for the subsurface reaction term. Further, the thermal conductivity and diffusivity probably cannot be estimated to within better than a factor of 2 or 3. Thus, considerable testing of the model against data to determine the best values of these parameters (within reasonable ranges) is required. Such testing has not yet been carried out.

As the program is stepped through the succeeding increments of fuel plane distance from the initial top of the oxidizer particle (see Table II-III), the oxidizer surface will either assume a protruding bulge or a depression relative to the planar fuel around it, depending upon whether the oxidizer linear regression rate is slower or faster than the

binder regression rate. This raises interesting questions regarding the "end-game" if the particle burns out before the surrounding fuel. (Geometrical considerations show that the inverse problem cannot occur as long as increment sizes are kept sufficiently small.) In this case, there is no oxidizer to burn with the surrounding fuel in succeeding increments and the burning rate is set equal to zero for these remaining increments. Three different approaches have been taken to calculating the average propellant burning rate from the information obtained during the procedure of stepping through the increments of regression of the fuel planar surface past the oxidizer particle (XDTOP) increments). In the first of these, the burning rate is calculated by statistically averaging all of the oxidizer mass fluxes and fuel mass fluxes over the increments and dividing by the propellant density:

$$r_{avg} = \frac{\sum_j (\dot{m}_{ox,p,j} APOX_j + \dot{m}_{fuel,j} AFU_j)}{\rho_{propellant} \sum_j (APOX_j + AFU_j)} \quad (45)$$

while in the second approach it is calculated by statistically averaging all of the oxidizer mass fluxes and then dividing by the overall oxidizer mass fraction and the propellant density:

$$r_{avg} = \frac{\sum_j \dot{m}_{ox,p,j} APOX_j}{\rho_{propellant} \alpha_{overall} \sum_j (APOX_j + AFU_j)} \quad (46)$$

$\alpha_{overall}$  = overall oxidizer-mass fraction

The fact that these two procedures do not always give the same result is tied in with the "end-game" problem mentioned above. If the oxidizer burns out before the fuel plane reaches the bottom of the oxidizer, mass fluxes for succeeding increments are set equal to zero in the procedure currently used. Not only does this result in different answers by the two above procedures, but it also pulls the average burn rates down. One's first temptation is

to simply perform the summing procedure over just these increments for which a burning rate is calculated, both in the numerator and denominator of Equations 45 and 46, but it is not clear whether or not this is more physically realistic than the procedure of summing over all increments, with burning rate set equal to zero for increments in which there is no oxidizer for the fuel. A third procedure of calculating average burning rate was developed which basically does take this approach, however, though in a slightly different manner. In this procedure, the burning rate is calculated by dividing the oxidizer particle diameter by the sum of the times required for each increment until the bottom of the oxidizer particle is reached:

$$r_{avg} = D_o / \sum_j TAU_j = D_o / \sum_j [(\Delta(DELOX))_j / r_{ox,j}] \quad (47)$$

$TAU_j$  = time for regression plane to move from one increment to the next; summation carried out only to increment at which oxidizer burns out

$DELOX_j$  = distance of center of oxidizer surface from initial oxidizer peak at jth calculation increment (See Figure III-3.)

$r_{ox,j}$  = linear oxidizer regression rate in jth calculation increment

This procedure begs the question of what happens to the fuel "left over" when the oxidizer particle burns out before the fuel. Physically we can perhaps just assume that it somehow flakes off. This question needs to be addressed further. This third approach is intuitively more appealing to this author in that it allows for the fact that the particle will spend more time at regression increments where the burning rate is lower, while the first two procedures involve an implicit assumption that each of the regression increments is equally likely.

To date, only preliminary calculations have been run with this model, with no attempt at optimizing the values of such parameters as  $K_{AP}$ ,  $K_{OF}$ ,  $B_{ox}$ ,  $E_{ox}$ ,  $B_{fuel}$  and  $E_{fuel}$ . These calculations have been run only for Formulation 4525, the 73/27 AP/HTPB propellant with 20 micron diameter unimodal oxidizer used as the baseline formulation in the experimental phase of this program. The equations used for thermal conductivity and gas diffusivity were:

$$\lambda = 5.5 \cdot 10^{-6} \sqrt{T} \text{ cal/cmsec } ^\circ\text{K}, \quad T \text{ in } ^\circ\text{K} \quad (48)$$

$$D = 1.0 \cdot 10^{-5} T^{3/2} / P \text{ cm}^2/\text{sec}, \quad T \text{ in } ^\circ\text{K}, P \text{ in atm.} \quad (49)$$

The activation energies for the fuel vaporization and oxidizer sublimation,  $E_{\text{fuel}}$  and  $E_{\text{ox}}$ , were chosen as 16,900 cal/mole and 22,000 cal/mole, respectively, the former value based on data of Cohen, Fleming, and Derr<sup>(36)</sup> and the latter based on data of Andersen and Chaiken.<sup>(35)</sup> The pre-exponential factor in the oxidizer sublimation expression,  $B_{\text{ox}}$  was set at  $2 \cdot 10^5$  gm/cm<sup>2</sup>sec based on the BDP analysis of pure ammonium perchlorate deflagration, while  $B_{\text{fuel}}$  was set at 5500 gm/cm<sup>2</sup>sec, this value being chosen to force the linear regression rates of oxidizer and fuel to be equal at  $T_g = 900^\circ\text{K}$  (somewhat arbitrary, to say the least). Based on the BDP analysis for pure ammonium perchlorate deflagration,  $K_{\text{AP}}$  (Eq'n. 36) was chosen to be 0.0001 to 0.0002 atm sec. The diffusion flame reaction distance constant  $K_{\text{OF}}$  (Eq'n. 35) was chosen to yield a reaction rate approximately ten times higher than the AP monopropellant reaction rate at  $T = 2000^\circ\text{K}$ , resulting in a range of values of  $(0.3 - 0.5) \cdot 10^{-13}$  atm sec  $^\circ\text{K}^{-2}$  (again, rather arbitrarily). Predicted burning rate versus pressure curves at 0 and 1000 ft/sec crossflow velocities for various combinations of these parameters are plotted in Figure II-5 along with data for Formulation 4525. As may be seen, agreement between theory and experiment is surprisingly good. However, it is realized that this may be fortuitous and that application of the model to other formulations may not give such satisfactory results.

#### 4. Examination of Effect of Postulated Flow Profiles

During the course of this program, the author became aware of complaints that data on erosive burning taken in test devices where driver grain product gases were passed over small specimens (strips or tablets) of the test propellant did not extrapolate well to motor conditions, the erosive effects being considerably less in actual motors than anticipated from the laboratory results. One possible explanation for this is that the boundary layer flow profiles are considerably different in the test device flow channel than in a motor. In most test devices, including the one used in this program, the ratio of blowing velocity (gas velocity normal to the propellant surface, generated by the combustion) to crossflow velocity is quite small, less than 0.05, lying in a range where the data

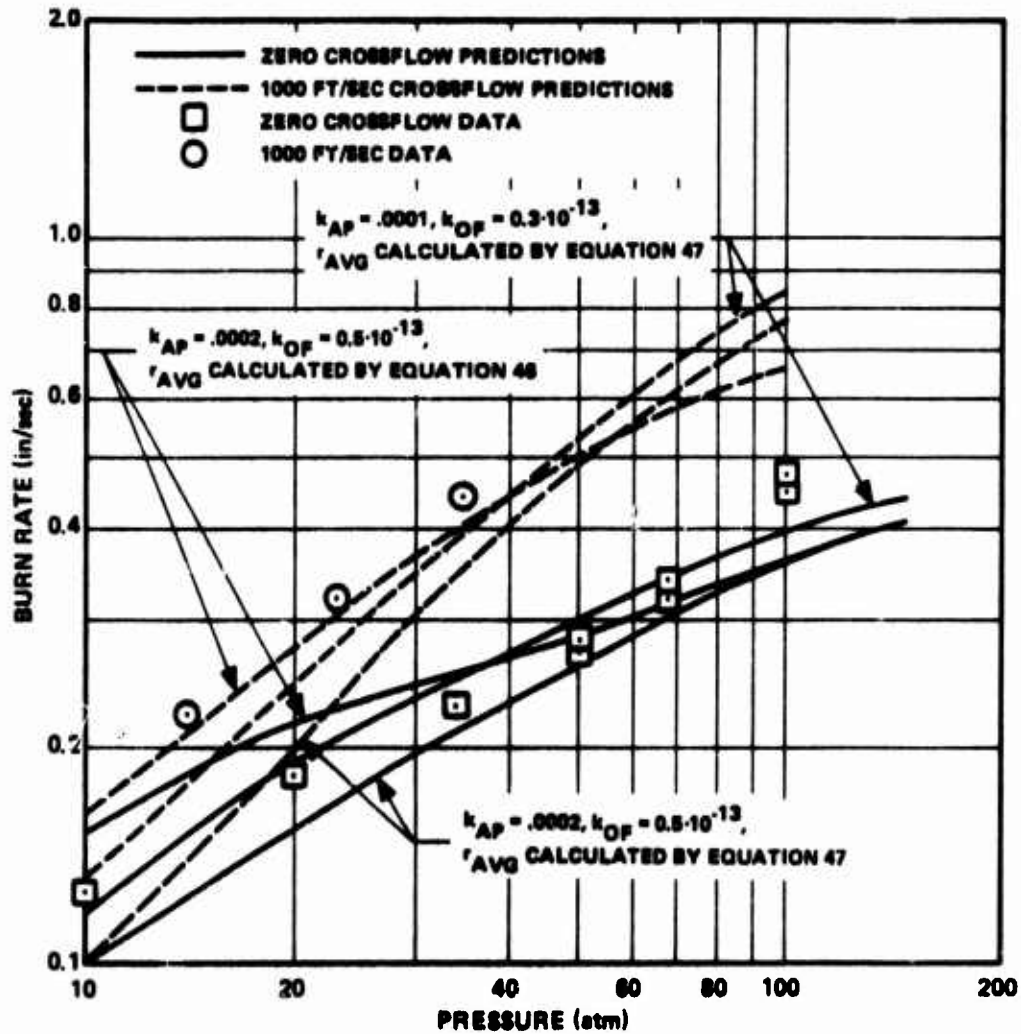


Figure 11-5. Results of Preliminary Calculations with Second Generation Model, Formulation 4525 (73/27 AP/HTPB, 20 micron Diameter AP).

of Mickley and Davis<sup>(31)</sup> used in both of the models described above are applicable. Recent work by Yamada, et al.<sup>(37)</sup> and Dunlap, et al.,<sup>(38)</sup> however, indicates that in cylindrically perforated motors, where the ratio of blowing velocity to crossflow velocity tends to be much higher (except at the aft end of very long grains), the flow profiles are considerably different, approximating those of an inviscid flow with a no-slip wall boundary condition. In this case, the axial velocity flow profile is given by (referring back to the nomenclature of the first generation model regarding diffusion distance):

$$u_{\text{crossflow},y} = L_{\text{diff}} \sin \theta = \frac{\bar{u}\pi}{2} \cos \left\{ \frac{\pi}{2} \left( \frac{(D/2) - L_{\text{Diff}} \sin \theta}{(D/2)} \right)^2 \right\} \quad (50)$$

$\bar{u}$  = average crossflow velocity

D = flow channel diameter

The first generation model was modified to use this profile rather than the one described by Equations 37 to 40 in the development of the second generation model (which was also used in the original version of the first generation model). A set of calculations was then run for a motor with a port diameter of 1.2 inches using both types of profiles for comparison. Formulation 4525 (73/27 AP/HTPB, 20 micron diameter AP) was used for these predictions since, as will be shown later, good agreement was found between the Generation 1 Model using the Mickley-Davis profiles and data taken in our test apparatus with this propellant. Results of these calculations are shown in Figure II-6. As may be seen, replacement of the Mickley-Davis profiles with the inviscid no-slip profiles results in a considerable reduction in the predicted degree of erosive burning. This is a particularly important result, pointing out the necessity of correct definition of flow profiles in a given motor configuration for accurate prediction of erosive burning. Thus it appears that further attention need be paid to accurate definition of profiles, not only in cylindrically perforated motors, but in wagon-wheel perforations, star configurations, and any other configurations where it is felt that erosive burning may be important. Modification of the first generation model (and the second generation model) to accommodate various flow profiles is quite simple, the modification of the first generation model to use inviscid no-slip profiles having taken less than one man-day.

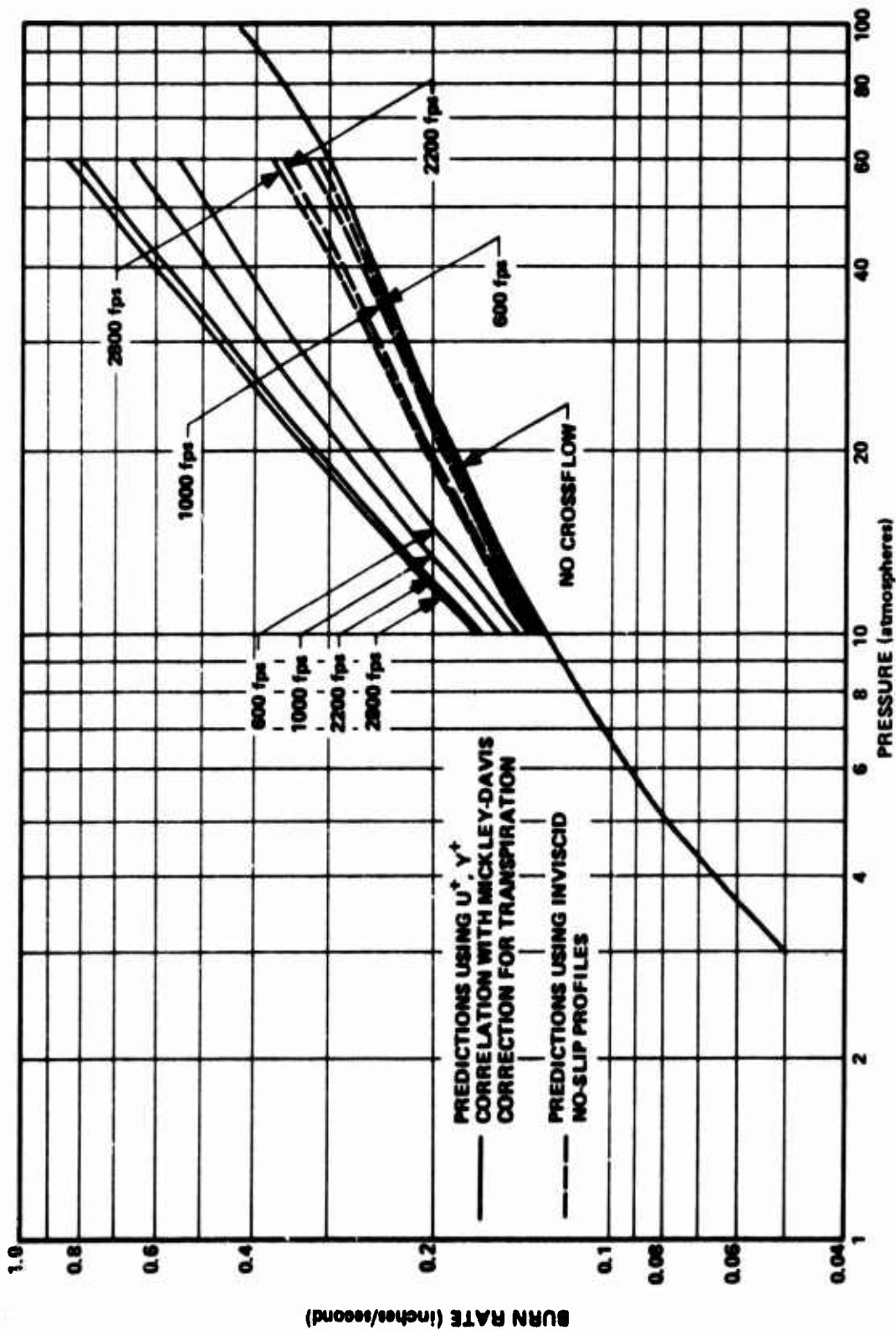


Figure 11-6. Erosive Burning Rate Predictions with the First Generation Model Using Mickley-Davis Boundary Layer Profiles and Using Inviscid No-Slip Wall Boundary Layer Profiles. Formulation 4525 (73/27 AP/HTPB, 20 micron Diameter AP).

C. EXPERIMENTAL

1. Equipment

In the past, two basically different approaches, each with advantages and disadvantages, have been pursued for measurement of steady-state erosive burning rates. The first involves determination of ablation rates of grains in rocket motors under actual firing conditions, while the second involves measurement of burning rates of propellant specimens (tablets or strips) located in a stream of hot flowing gas external to a motor. The first method has the advantage that the erosive burning process is being studied under actual motor test conditions, but the disadvantage that these conditions are difficult to determine accurately. Pressure and velocity vary through the chamber and also change with time. Such burn rate measurement techniques as interrupted burning must use time-averaged values, and the time periods must be relatively long. Continuous measurement of burning rates within a rocket by x-ray requires special elaborate equipment. The use of probes to measure burning rates and pressures is difficult because many probes are required, and also runs the risk of interfering with the chamber flow and disturbing normal burning.

The major disadvantage of the second method of studying erosive burning lies in possible differences in detailed flow characteristics for flow over strips or buttons of propellant, as compared to flow adjacent to a grain surface in a motor, even at the same freestream velocity and pressure. (In fact, while flow of a hot gas stream from a gas generator over a propellant strip or button preceded by some sort of flow channel will tend to develop turbulent boundary layer type profiles, the recent work by Yamada, et al.,<sup>(37)</sup> and Dunlap, et al.,<sup>(38)</sup> indicates that the flow profiles in typical cylindrically perforated motors approximate those of an inviscid flow with a no-slip wall boundary condition, as discussed in the preceding section of this report.) Advantages are that such parameters as freestream crossflow velocity and pressure can be easily controlled and measured. Most important, continuous measurement of burning rate can be accomplished with high speed visual photography through quartz windows in the apparatus. Hence, results obtained using this approach are likely to be more accurate and reliable than those from motor firings.

Previous studies have, in general, not resulted in instantaneous measurements of erosive burning rates under well-characterized local flow conditions. This, coupled with a lack of data in the high Mach number region ( $M \geq 0.5$ ) and a lack of studies in which propellant parameters are systematically varied one at a time under identical hydrodynamic conditions has resulted in an incomplete understanding of erosive burning phenomena.

The experimental test apparatus and procedures employed in this study of erosive burning are described in some detail in Reference 12. A schematic of the basic test apparatus is presented as Figure II-7. A cylindrically perforated 604 driver grain (15.2 cm outside diameter, 10.2 cm inside diameter) whose length is chosen to give the desired operating pressure for a given test, produces a high velocity gas flow through a transition section into a rectangular test section which contains the test grain (generally the same formulation as the driver grain). The contoured transition section is approximately 10 cm (4 inches) long. The test grain extends from the test section back through the transition section to butt against the driver grain in order to eliminate leading edge effects which would be associated with a test grain standing alone. The test grain is approximately 30 cm (12 inches) long (plus the 10 cm extending through the transition section) by 1.90 x 2.50 cm (3/4 inch and 1 inch) web and burns only on the 1.90 cm face. The flow channel of the test section is initially 1.90 cm x 1.90 cm (3/4 inch x 3/4 inch), opening up to 1.90 cm x 4.45 cm (3/4 inch x 1-3/4 inch) as the test propellant burns back through its 2.54 cm (1 inch) web. For high Mach number tests, the apparatus was operated in a nozzleless mode with the gases choking at or near the end of the test grain, while for lower Mach Number tests, a 2-dimensional nozzle was installed at the end of the test channel.

During each test, pressure and crossflow velocity varied with time and location along the test grain. (For the nozzleless tests, pressure varied significantly with time and location, while crossflow velocity varied considerably with location but not significantly with time. For tests using a nozzle with an initial port to throat area ratio of 1.5 or higher, on the other hand, pressure did not vary strongly with location but did rise with time due to the progressivity of the driver grain, while

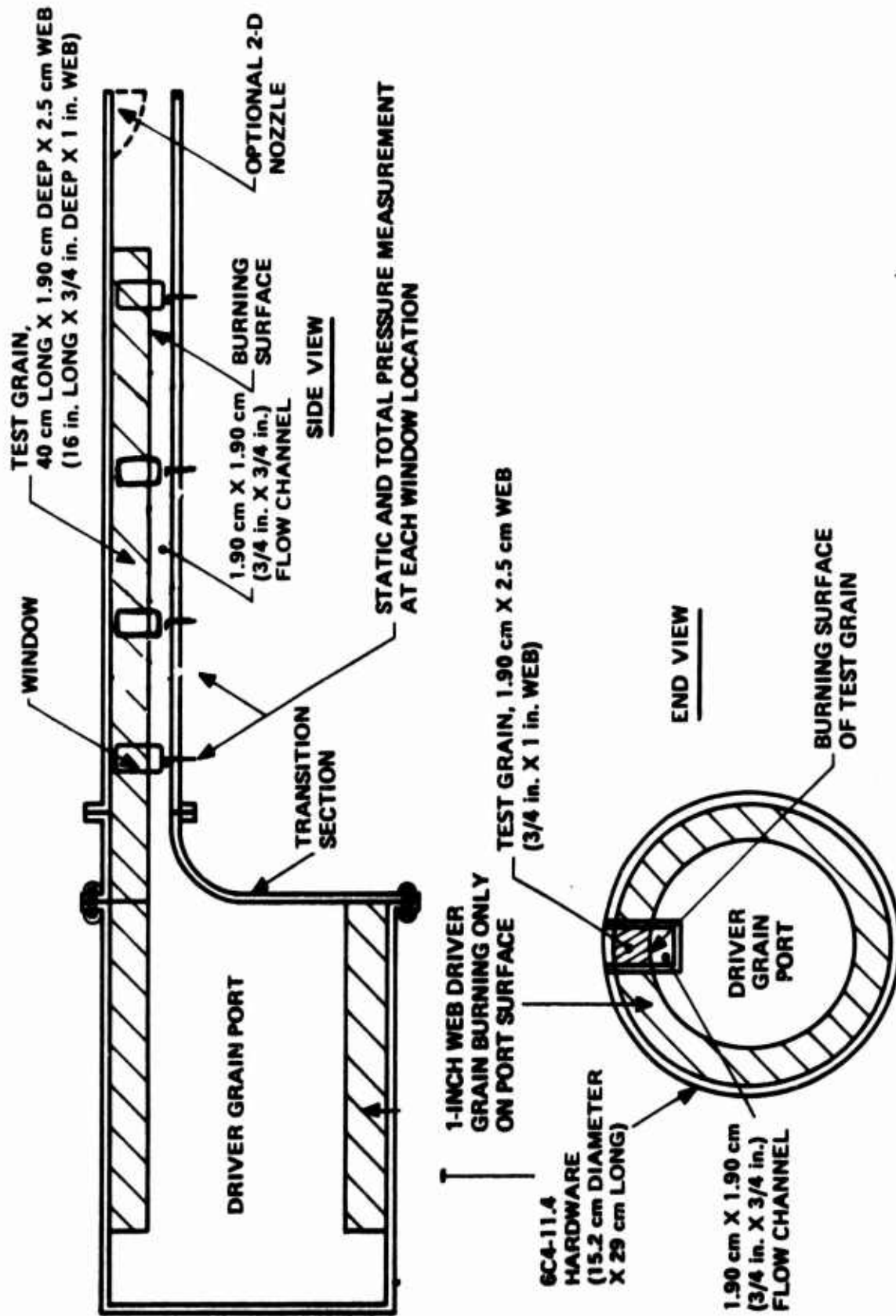
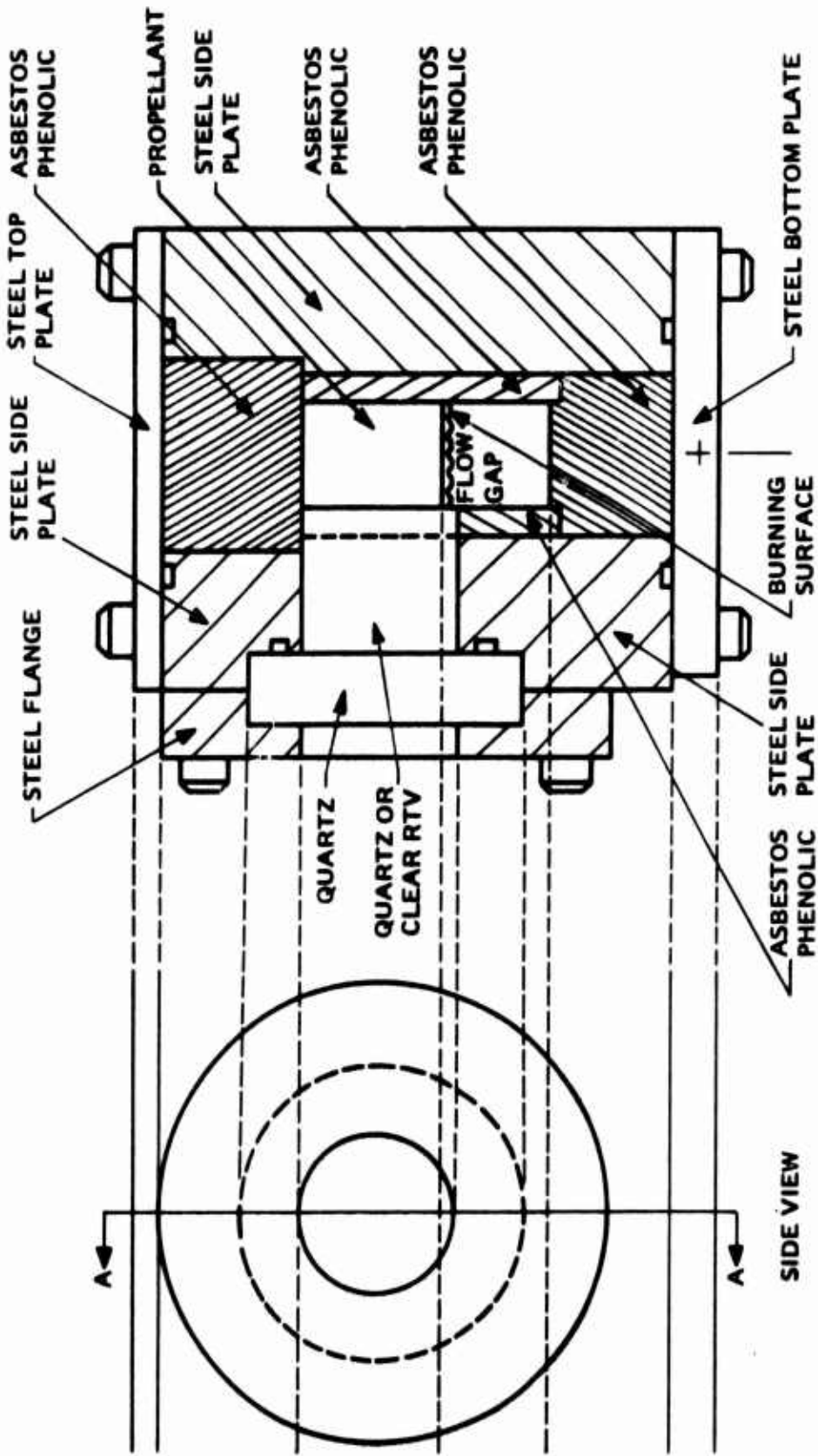


Figure 11-7. Sketch of Test Hardware.

crossflow velocity varied strongly with time and slightly with location.) These variations permitted design of tests to yield considerable burning rate-pressure-crossflow velocity data in relatively few tests, provided that these parameters could be measured continuously at several locations along the test grain. These parameters were measured in the following manner.

The burning rate was directly measured by photographing the ablating grain with a high-speed motion picture camera through a series of four quartz windows located along the length of the test section. (See Figure II-7 and II-8.) Frame by frame analysis of the films allowed determination of instantaneous burning rate as a function of time at each of the four window locations. The windows were flush-mounted on the inside of one side wall and sealed with "O"-ring seals. A detailed drawing of the test section, emphasizing the viewing window layout is shown in Figure II-8. The flow gap was surrounded by propellant on one side and asbestos phenolic on the other three sides, with circular cutouts in the asbestos phenolic through which the inner part of the windows butted flush against the propellant. (Inner and outer window sections were used, since under the more severe test conditions, the inner window surface suffers damage during the test or during post-test cooldown.) To date, tests with either quartz or RTV potting compound inner windows have been satisfactory as long as the side of the test propellant was adequately inhibited to prevent any side-burning, and quite satisfactory films have been obtained.

For nozzled cases, the measured location of the burning propellant surface at each window as a function of time, together with the known constant throat area, permitted straightforward calculation of the crossflow velocity as a function of time. However, the very sensitive dependence of Mach Number on area ratio for  $M > 0.5$  made calculation of crossflow velocity from area ratio measurement quite poor for nozzleless cases. Accordingly, for these tests, stagnation pressure was measured at the aft end of the test section and used in combination with the measured driver chamber pressure for calculation of the stagnation pressure in the test section as a function of time and position. (Static pressure wall taps at each window location were used for measurement of static pressure as a



END VIEW - SECTION A-A

Figure 11-8. Test Section Detail, Emphasizing Viewing Windows.

function of time for both nozzleed and nozzleless cases.) From the static and stagnation pressure values determined as a function of time and position down the test section, crossflow Mach Number and velocity were calculated as a function of time at each window location in the test section for the nozzleless cases.

## 2. Test Matrix

The rationale of the experimental part of this program was to measure the erosive burning characteristics, over a wide range of pressure and crossflow velocity, of a series of propellants in which various formulation parameters were systematically varied. A series of 14 formulations (Table II-IV) was originally selected for investigation, with 10 tests to be conducted with the first formulation, and 5 tests each with the succeeding formulations. During the course of this program, seven of these formulations (1 - 5, 7 and 8) were characterized. Additional study of the matrix will be carried out in a follow-on program.

The first six formulations listed in Table II-IV are "scholastic" formulations. (These are referred to as "scholastic" formulations in that they are formulations specifically chosen to permit systematic variation of well-defined composition and ingredient-size parameters, including the use of unimodal ammonium perchlorate particle size, but as a consequence are not formulations being currently considered for mission applications.) It was considered that the use of unimodal oxidizer in early testing was important, since any model permitting prediction of burning rate-pressure-crossflow velocity characteristics from first principles will almost certainly be first derived for unimodal oxidizer. (Methods of handling multimodal oxidizer sizes for predictions of burning rates even in the absence of crossflows are still the subject of considerable debate.) Formulation 1 (also referred to elsewhere as Formulation 4525) is a baseline 1667°K HTPB formulation (73/27 AP/HTPB) for the initial test series. Formulations 2, 3, and 4 (5051, 4685 and 4869) were selected for investigation of the interrelated effects of oxidizer particle size and base (no crossflow) burning rate. Formulations 1 and 4 are essentially identical except for use of burning rate catalyst to change base burning rate. Formulations 2 and 3 differ from Formulation 1 in oxidizer particle size (200, 5 and

TABLE II-IV. Formulations Selected for Testing \*\*

<u>Number*</u>	<u>Composition</u>	<u>Rationale</u>
1(4525)	73/27 AP/HTPB, 20 $\mu$ AP	Baseline Formulation, T = 1667°K
2(5051)	73/27 AP/HTPB, 200 $\mu$ AP	Compare with 1 for AP Size Effect
3(4685)	73/27 AP/HTPB, 5 $\mu$ AP	Compare with 1 and 2 for AP Size Effect
4(4869)	72/26/2 AP/HTPB/Fe <sub>2</sub> O <sub>3</sub> , 20 $\mu$ AP	Compare with 1 for BR Effect at Constant AP Size
5(5524T)	77/23 AP/HTPB, 20 $\mu$ AP	Compare with 1 for Mix Ratio (Temperature) Effect at Constant AP Size. T = 2065 °K
6	65/35 AP/Polyester, 20 $\mu$ AP	Baseline Polyester Formulation, T = 1850 °K. Compare with 1 for Binder Effect.
7(5565T)	82/18 AP/HTPB, Bimodal AP (68.33% 20 $\mu$ , 13.65% 90 $\mu$ )	Medium Temperature HTPB Formulation. AP Sizes Chosen to Match BR of No. 1, Compare with 1 for Temperature Effect T = 2575°K.
8(5555T)	82/18 AP/HTPB, Bimodal AP (41% 1 $\mu$ , 41% 7 $\mu$ )	Compare with 7 for BR Effect. T = 2575°K.
9	75AP/25 Polyester, Bimodal AP Giving BR to Match No. 6	Medium Temperature Smokeless Polyester Formulation. Compare with No. 6.
10	88AP/12 HTPB, Multimodal AP	Arcadene 368 (Operational Smokeless Propellant).
11	74AP/21 HTPB/5 Al, Multimodal AP to Match BR of No. 7	Same Temperature as No. 7. Compare with No. 7 for Aluminum Effect.
12	80AP/15HTPB/5Al, Multimodal AP to Match BR of No. 11	Compare with No. 11 for Mixture Ratio (Temperature) Effect.
13	73AP/17 HTPB/10Al, Multimodal AP to Match BR of No. 12	Same Temperature as No. 12. Compare with No. 12 for 5 vs. 10% Aluminum.
14	70AP/12HTPB/18 Al, Multimodal AP	Candidate Metallized Nozzleless Motor Propellant.

\*Formulations 1 - 6 are "scholastic" formulations.

\*\*Formulations 1 - 5, 7 and 8 tested during this program.

20 micron AP, respectively), and as a consequence, also in base burning rate. Comparison of results from tests with these four formulations should permit isolation of the oxidizer particle size and base burning rate effects on sensitivity of propellant burning rate to crossflow.

In terms of independent variables, Formulation 5 (5542T) differs from Formulation 1 only in terms of oxidizer/fuel ratio (77/23 versus 73/27), yielding a higher flame temperature (2065°K vs. 1667°K) and a different burning rate, oxidizer size being held constant. Thus comparison of the results for these formulations permits definition of the effect of oxidizer/fuel ratio change at constant oxidizer particle size. With Formulation 7 (5565T), on the other hand, oxidizer/fuel ratio is varied from that of Formulation 1 (82/18 vs. 73/27), but oxidizer sizes are changed to give approximately the same zero-crossflow burning rate-pressure curve for the two formulations - this permits examination of the effect of varying oxidizer/fuel (and thus flame temperature) at constant base burning rate. Formulation 8 (5555T) is identical to Formulation 7 except for use of much finer oxidizer to yield higher base burning rate.

A total of 45 tests were carried out with these seven formulations. Of these, 39 yielded useful data, while six were failures due to breakup of the test grain (in nozzleless tests) or due to camera failure. The rationale and ballistics analyses used in selecting the test conditions employed were discussed in detail in Reference 12. Basically, the first three tests were designed to yield erosive burning data for Formulation 1 over a range of crossflow velocities of 180 to 350 m/sec (600 to 1200 ft/sec) and a range of pressures of 1.4 to 8.2 MPa (200 to 1200 Psia). The next three tests were chosen to examine the same formulation over a crossflow velocity range of approximately 600 to 850 m/sec (2000 to 2800 ft/sec) and a pressure range of 1 to 5 MPa (150 to 750 psia). Tests 7 and 8 differed from Tests 1 and 3 only in having no test grain in the transition section. These tests were aimed at determining the sensitivity of erosive burning to major upstream geometry changes. Tests 9 and 10 differed from Tests 1 and 3 only in their use of a hotter (2400°K) driver formulation with the baseline test formulation (1667°K flame temperature). The purpose of these tests was to determine whether the "core" gas temperature affected the erosive burning of a given formulation. (Recall that Marklund and

Lake<sup>(7)</sup> found that it did not.) Test 11 - 15, 16 - 20, 21 - 25, 26 - 30, 31 - 35 and 36 - 40 were designed to be analogous to Test 1 - 5 with replacement of Formulation 1 (4525) by Formulations 2, 3, 4, 5, 7 and 8 (5051, 4685, 4869, 5542T, 5565T, and 5555T). Tests 41 - 45 were added to fill in data gaps revealed by earlier tests.

### 3. Test Results and Discussion

Measured burning rate augmentation ratios ( $\epsilon = r/r_0$ ) for two typical nozzled tests are plotted against time in Figure II-9 and II-10. For these tests, the augmentation ratio at any given time should be nearly the same from window to window (since pressure and crossflow velocity do not vary significantly with location), unless boundary layer development effects are playing an important role. As may be seen, the variation from window to window is actually fairly small. The augmentation ratio versus time predicted with the first generation model described earlier, using the measured pressure and crossflow velocity versus time data, is also presented in these figures. The agreement between theory and experiment is seen to be reasonably good.

Results of the tests made for study of the effect of upstream flow conditions (two tests conducted at essentially identical conditions to tests in the main test series, except for the absence of test grain in the transition section) are presented in Figure II-11 and II-12. As may be seen, the effects of the upstream flow change were quite small, the differences in burning rate augmentation ratio between corresponding tests varying essentially only to the degree predicted by the slight difference in pressure-crossflow velocity-time history in the matched tests. Accordingly, it is concluded that the erosive burning measured at the viewing ports is not particularly sensitive to the driver grain-transition section contours in the test apparatus. This result is consistent with the observation that the augmentation rates do not vary significantly with window location for the nozzled tests (where pressure and crossflow velocity are nearly the same at each window location at any given time).

As discussed earlier, erosive burning models based upon increased heat transfer from a "core" gas flow accompanying crossflow, predict that

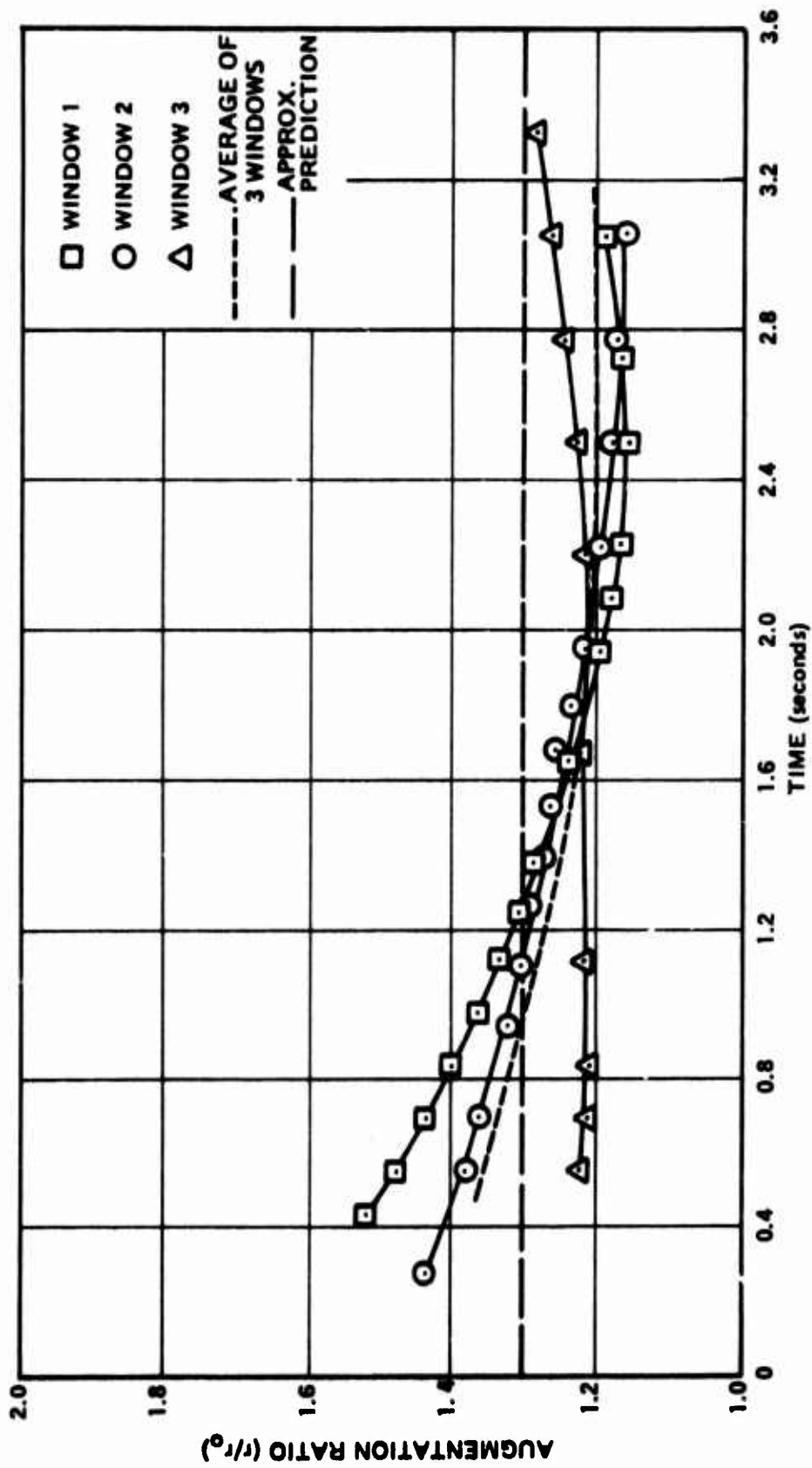


Figure 11-9. Burning Rate Augmentation Ratio Versus Time for Test Condition No. 1, Formulation No. 1 (4525), Nozzled Test, Low Pressure.

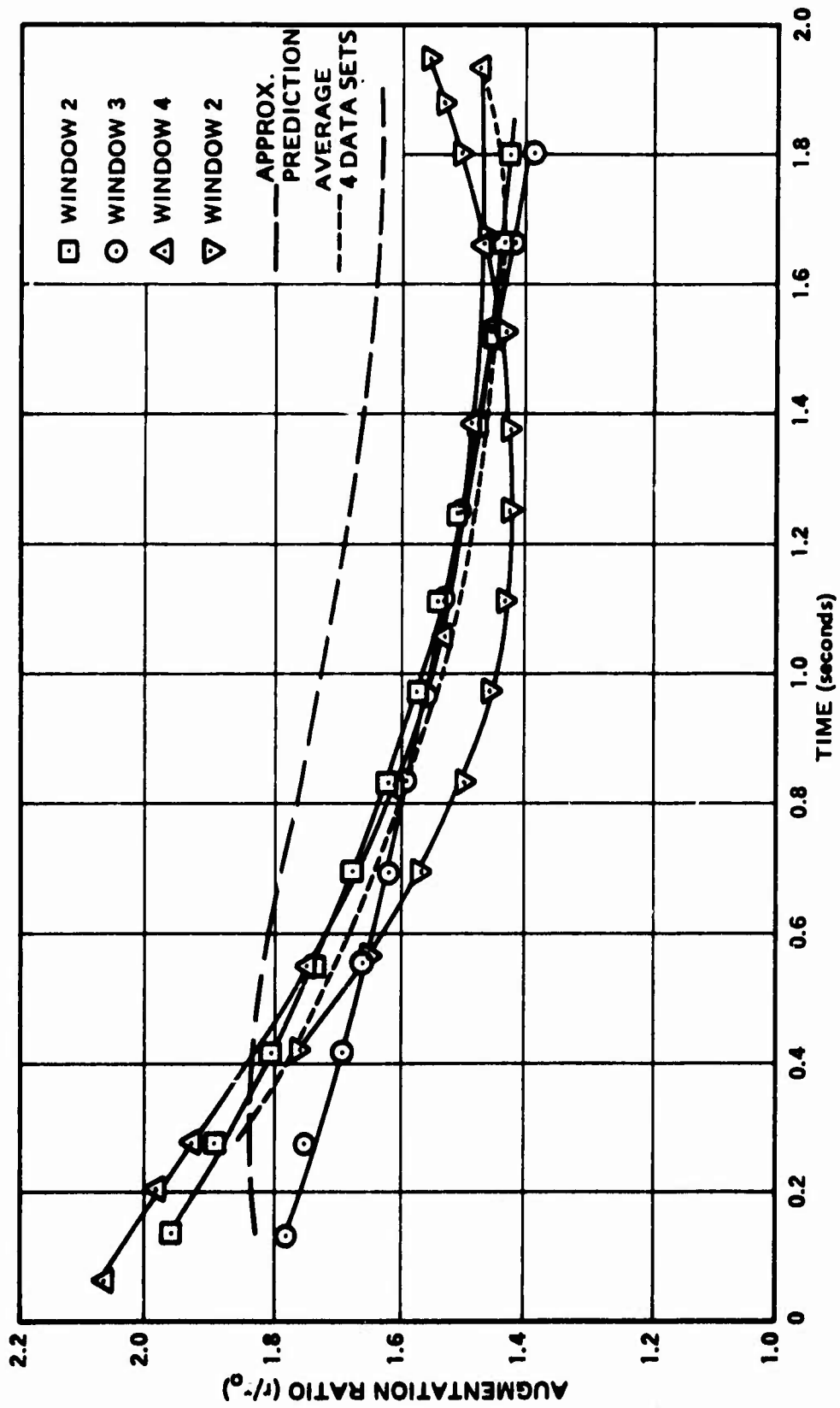


Figure 11-10. Burning Rate Augmentation Ratio Versus Time for Test Condition No. 8, Formulation No. 1 (4525) - Nozzled Test, High Pressure, No Grain in Transition Section.

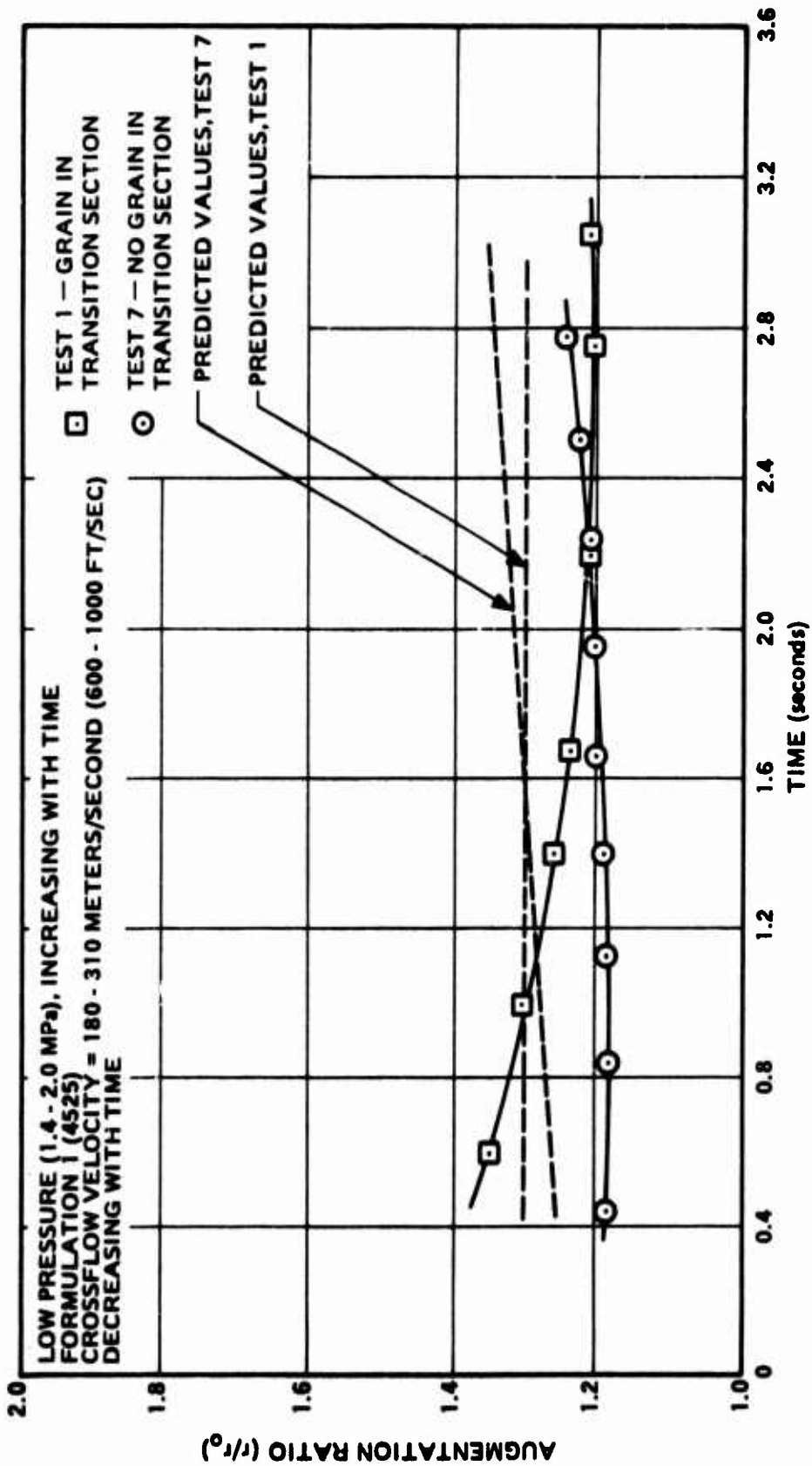


Figure II-11. Comparison of Erosive Burning with and Without Test Grain Extending Thru Transition Section to Mate with Driver Grain - Low Pressure.

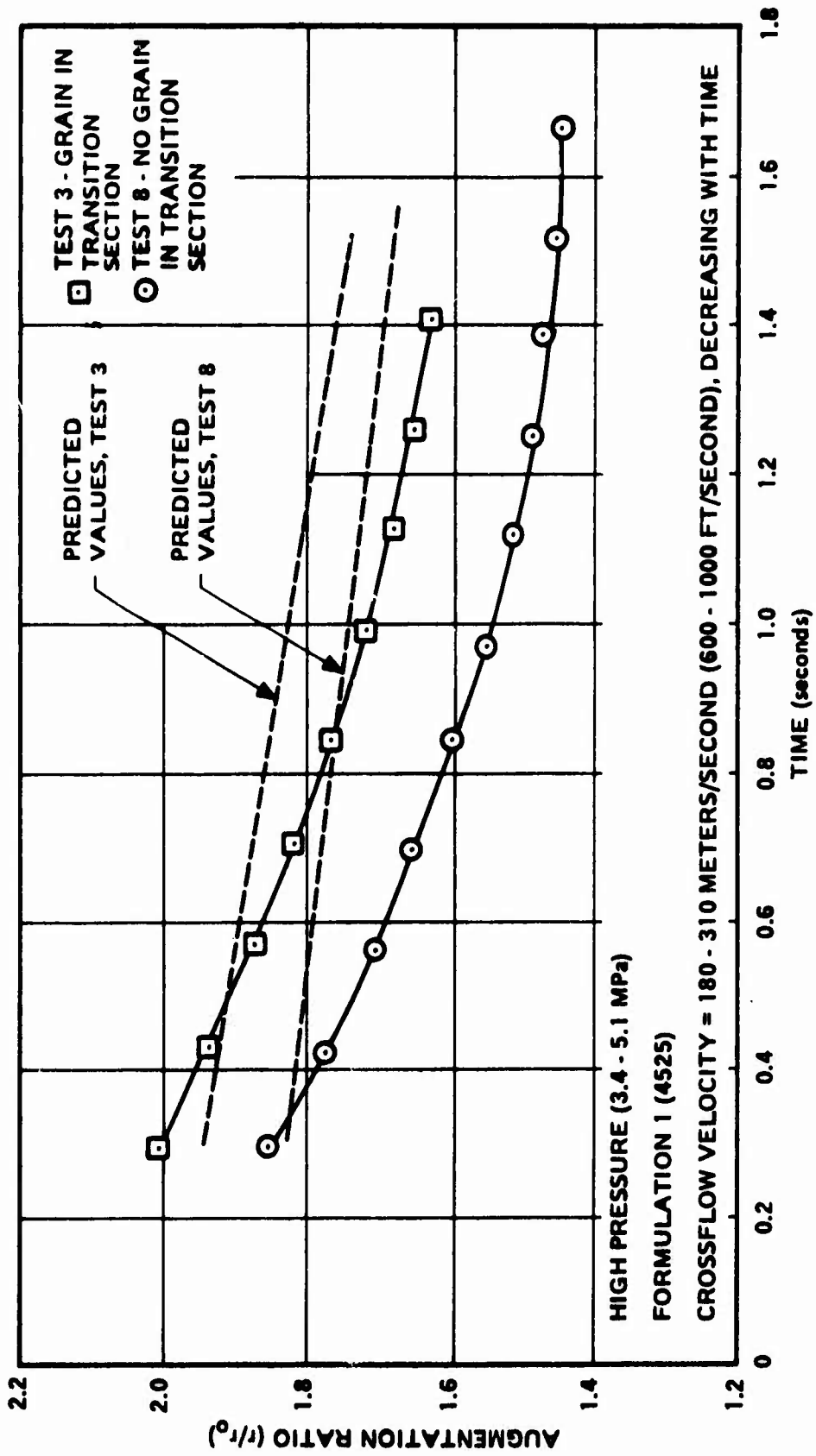


Figure 11-12. Comparison of Erosive Burning with and Without Test Grain Extending Thru Transition Section to Mate with Driver Grain - High Pressure.

with a given test section propellant, variation of the flame temperature of the driver propellant should lead to variation in the erosive burning augmentation ratio at fixed crossflow velocity and pressure. Two pairs of tests (1 and 9, 3 and 10), in which the driver grain flame temperature was varied from 1667°K to 2425°K, while the test section propellant was held constant and crossflow velocity and pressure versus time histories were held as nearly constant as possible, were carried out in this program. Results are presented in Figures II-13 and II-14. In each figure, measured burning rate augmentation ratio and the ratio predicted using the first generation model described earlier are plotted against time for each of the paired tests. (The predicted values are presented to permit a zeroing out of the slight differences in pressure and crossflow velocity versus time histories of the paired tests.) The different "core" gas temperatures in the paired tests are seen to have negligible effect on the erosive burning characteristics of the test propellant. This result is consistent with the results of Marklund and Lake<sup>(7)</sup> and casts further doubt on the validity of models in Category 1 of Table II-II (most notably, the commonly used model of Lenoir and Robillard).

A rather complete set of data, covering a pressure range of 1 to 5 MPa (10 to 50 atmospheres) and a crossflow velocity range of 180 to 670 m/sec (600 to 2200 ft/sec) has been obtained for Formulation 4525. (This is the baseline HTPB formulation, containing 73 weight percent 20 micron diameter ammonium perchlorate and 27 weight percent hydroxyterminated polybutadiene (HTPB) binder, with a trace of carbon black added to opacify the propellant.) Experimental results and theoretical predictions are presented in Figure II-15 and II-16. As may be seen, agreement between prediction and data, while not as good as with the Saderholm propellant, is reasonably good. The predicted curves for burning rate versus pressure at various crossflow velocities (Figure II-15) do seem to group more tightly than the data. That is, as shown more clearly in Figure II-16, the model tends to slightly overpredict the burning rate at low crossflow velocities and slightly underpredict it at high velocities.

Theoretical predictions and experimental measurements of erosive burning rates for Formulations 5051, 4685, 4869, 5542T, 5565T, and 5555T are presented in Figures II-17 through II-22. Formulation 5051, which

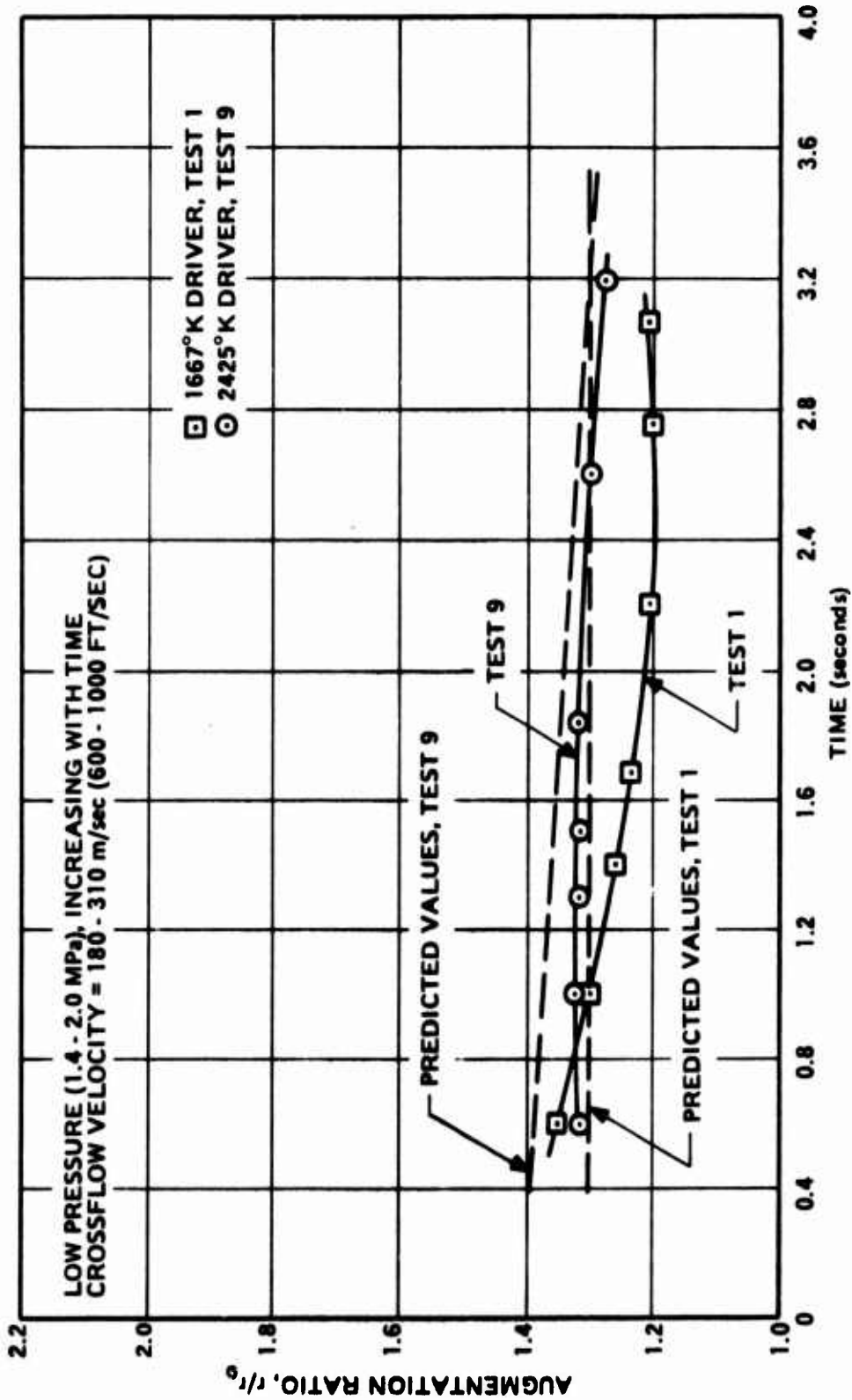


Figure II-13. Comparison of Erosive Burning of Formulation 1 (4525) with 1667°K Driver Grain and 2425°K Driver Grain - Low Pressure.

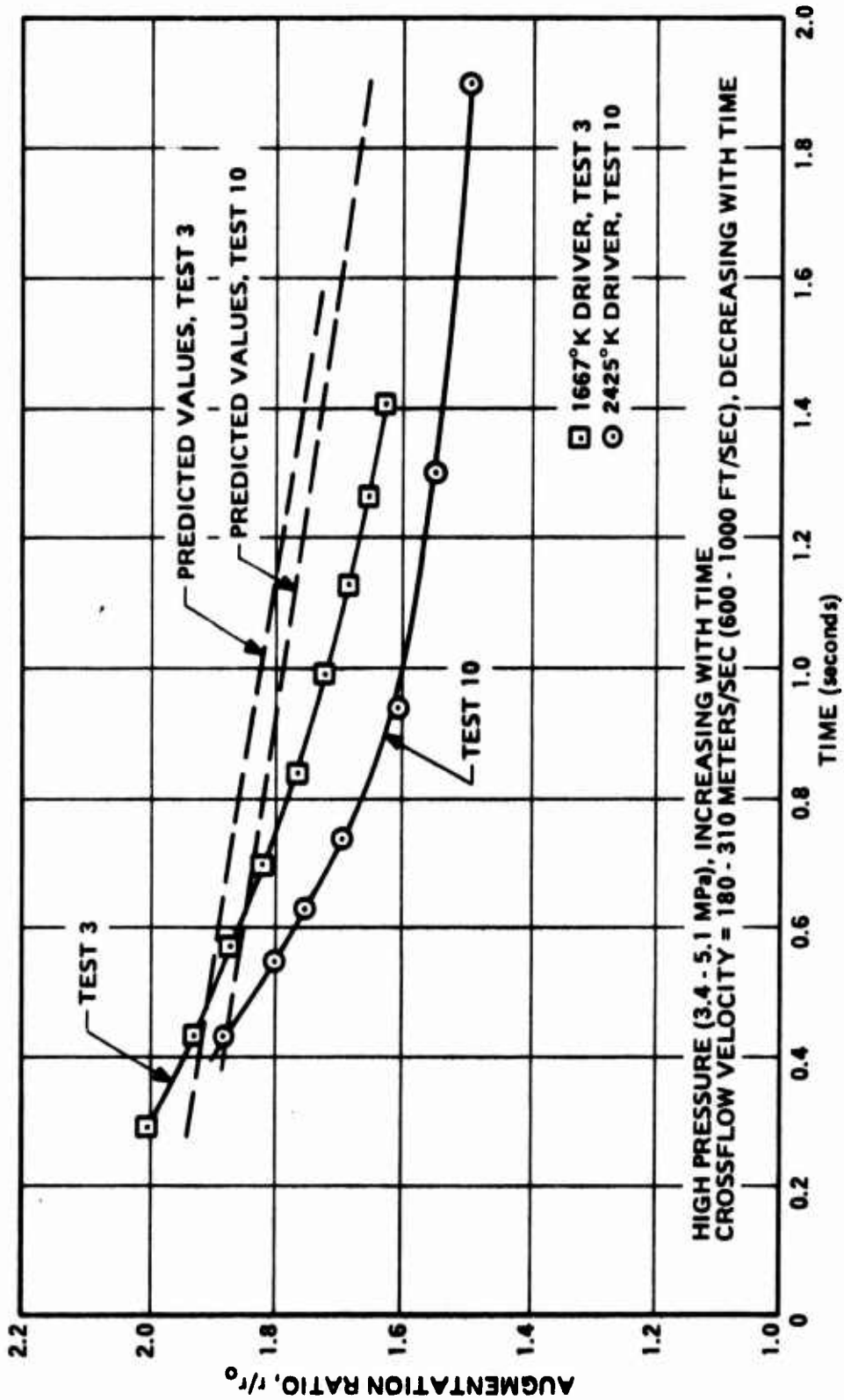


Figure II-14. Comparison of Erosive Burning of Formulation 1 (4525) with 1667°K Driver Grain and 2425°K Driver Grain - High Pressure.

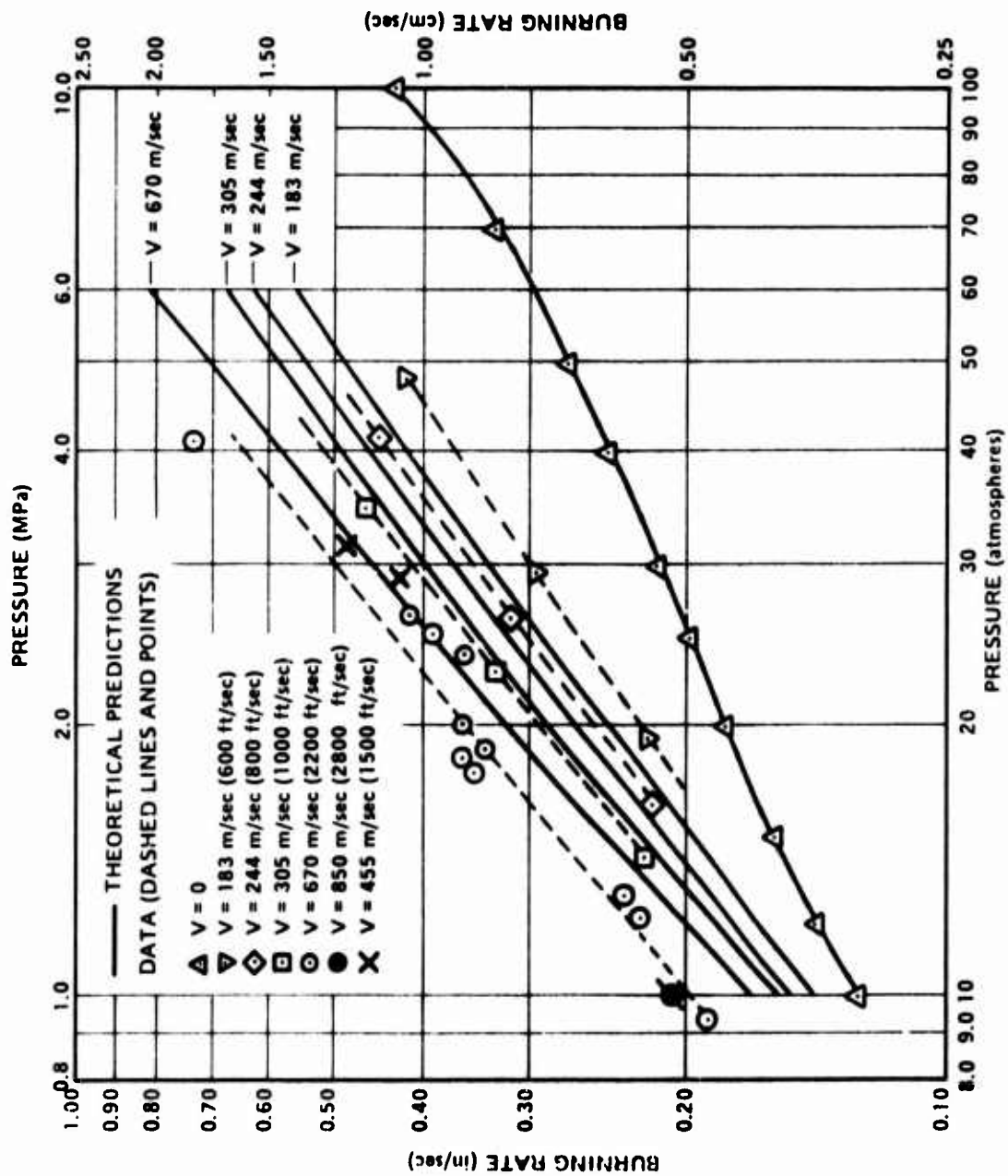


Figure 11-15. Theoretical and Experimental Burn Rate - Pressure Relationships for Various Crossflow Velocities for Formulation 4525 (1667°K) Formulation, 73/27 AP/HTPB, 20 Micron AP).

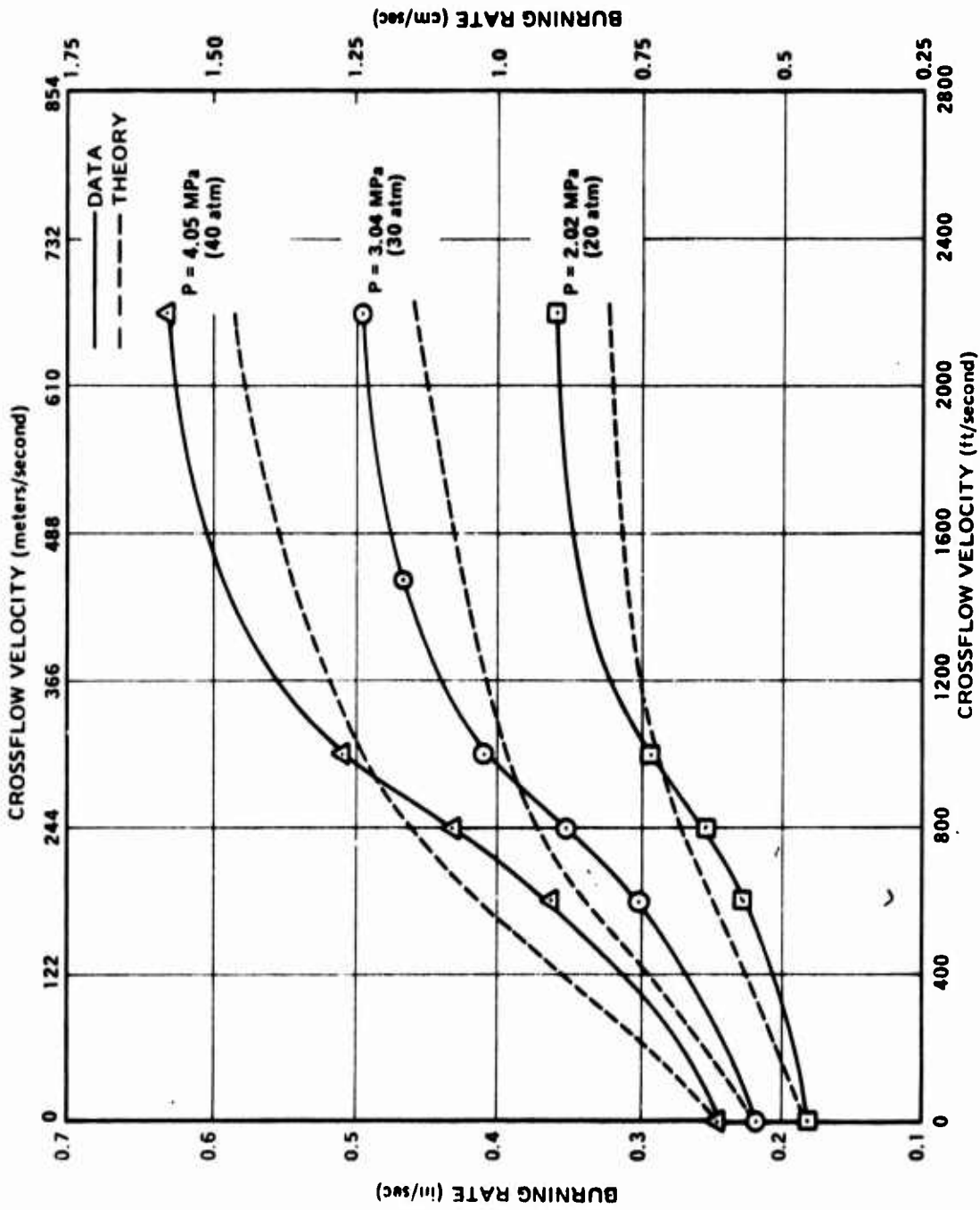


Figure II-16. Burning Rate Versus Crossflow Velocity Data and Predictions for Formulation 4525 (73/27 AP/HTPB, 20 Micron AP).

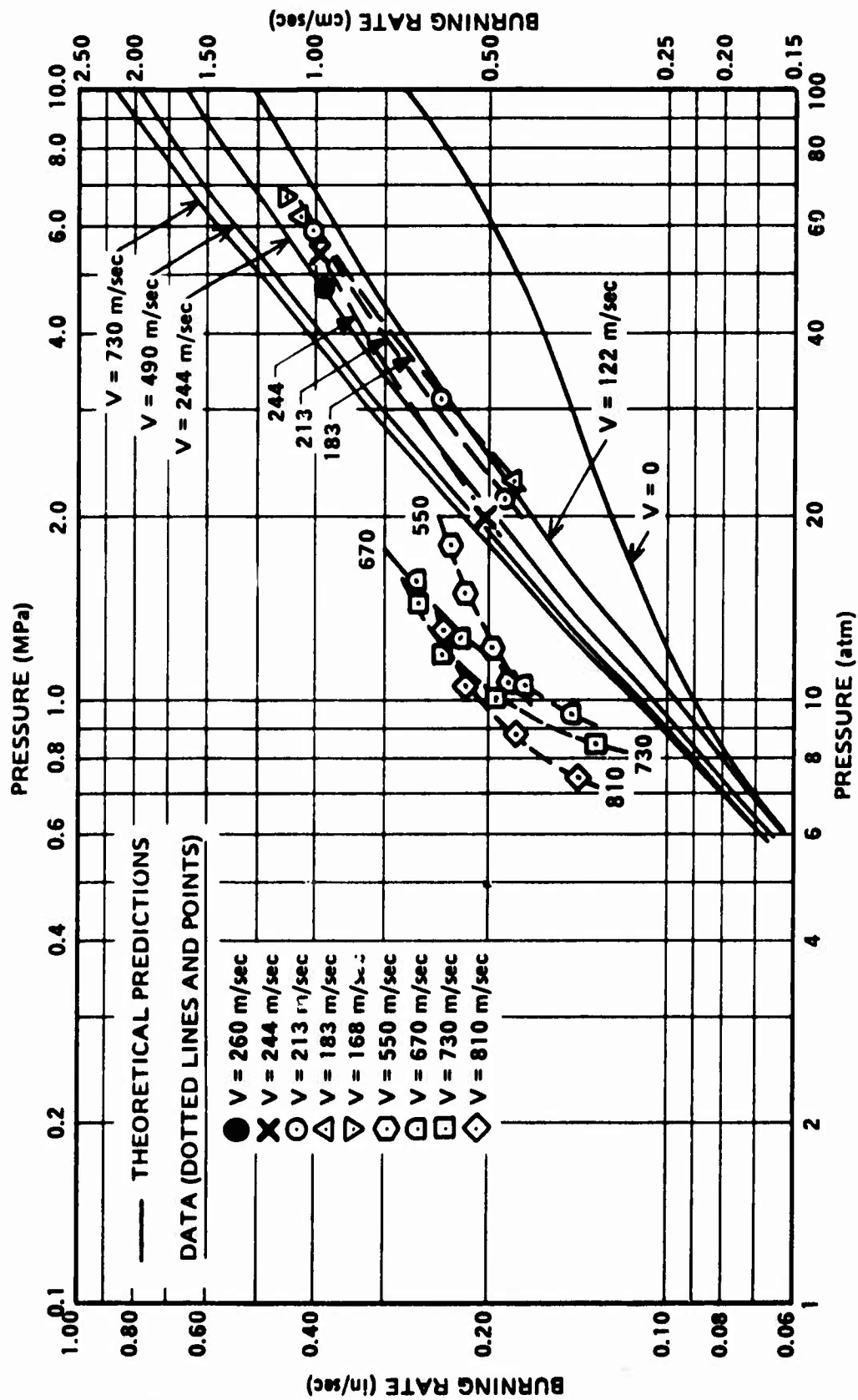


Figure 11-17. Theoretical and Experimental Burn Rate - Pressure Relationships for Various Crossflow Velocities for Formulation 5051 (1667°K Formulation, 73/27 AP/HTPB, 200 Micron AP).

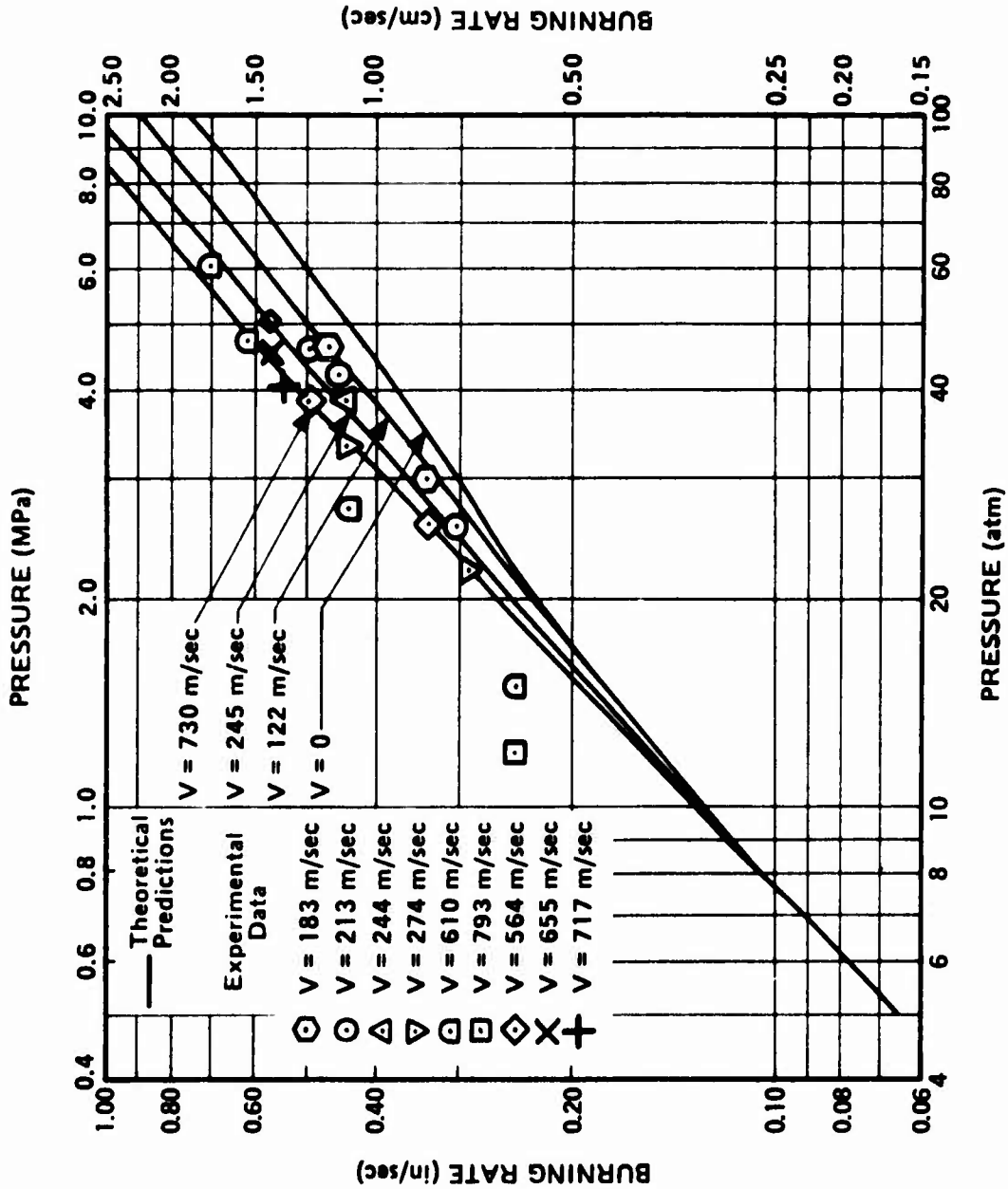


Figure 11-18. Theoretical and Experimental Burn Rate - Pressure Relationships for Various Crossflow Velocities for Formulation 4685 (1667°K Formulation, 73/27 AP/HTPB, 5 Micron AP).

differs from the baseline formulation through use of 200 micron AP oxidizer in place of 20 micron oxidizer, is predicted to be somewhat more sensitive to crossflow than the baseline formulations. Except at low pressure and very high crossflow velocities, agreement between predicted and measured augmentation ratio is fairly good. At low pressure and high crossflow velocity, however, the measured burning rates considerably exceed the predicted values. As shown in Figure II-18, Formulation 4685, which differs from the baseline formulation by replacement of 20 micron oxidizer with 5 micron oxidizer, exhibits considerably less sensitivity to erosion than that baseline formulation, as predicted. Agreement between predicted and observed burning rates appears to be good, except, again, in the low pressure, high crossflow velocity region (less than 2 MPa or 20 atmospheres, greater than 300 to 600 m/sec or 1000 to 2000 ft/sec crossflow velocity). Break-down of the model presented herein in this pressure-crossflow velocity region is not unexpected since, in this region, the composite propellant begins to behave more like a homogeneous propellant than a heterogeneous propellant, and the model only considers effects of crossflow on the diffusional mixing processes of oxidizer and fuel streams. In order for the model to be useful in low pressure, high crossflow velocity regions, it appears that an additional mechanism beyond that of flame-bending must be invoked. With Formulation 4869 (Figure II-19), which differs from the baseline formulation through addition of two percent iron oxide catalyst, data and theoretical predictions agree fairly well at high crossflow velocities, but not nearly as well at low crossflow velocities where the predictions of erosive burning rate augmentation are somewhat higher than observed in the experiments. An explanation of this discrepancy has not yet been developed.

With Formulation 5542T (analogous to the baseline formulation but with higher oxidizer/fuel ratio and consequently higher temperature and base burning rate, oxidizer size being held constant) the sensitivity to crossflow appears to be somewhat lower than predicted (Figure II-20) though the degree of disagreement between data and theory is not gross. The data obtained for Formulation 5565T (with approximately the same zero crossflow burning rate-pressure behavior as the baseline formulation, but a considerably higher oxidizer/fuel ratio and flame temperature) presented in Figure II-21

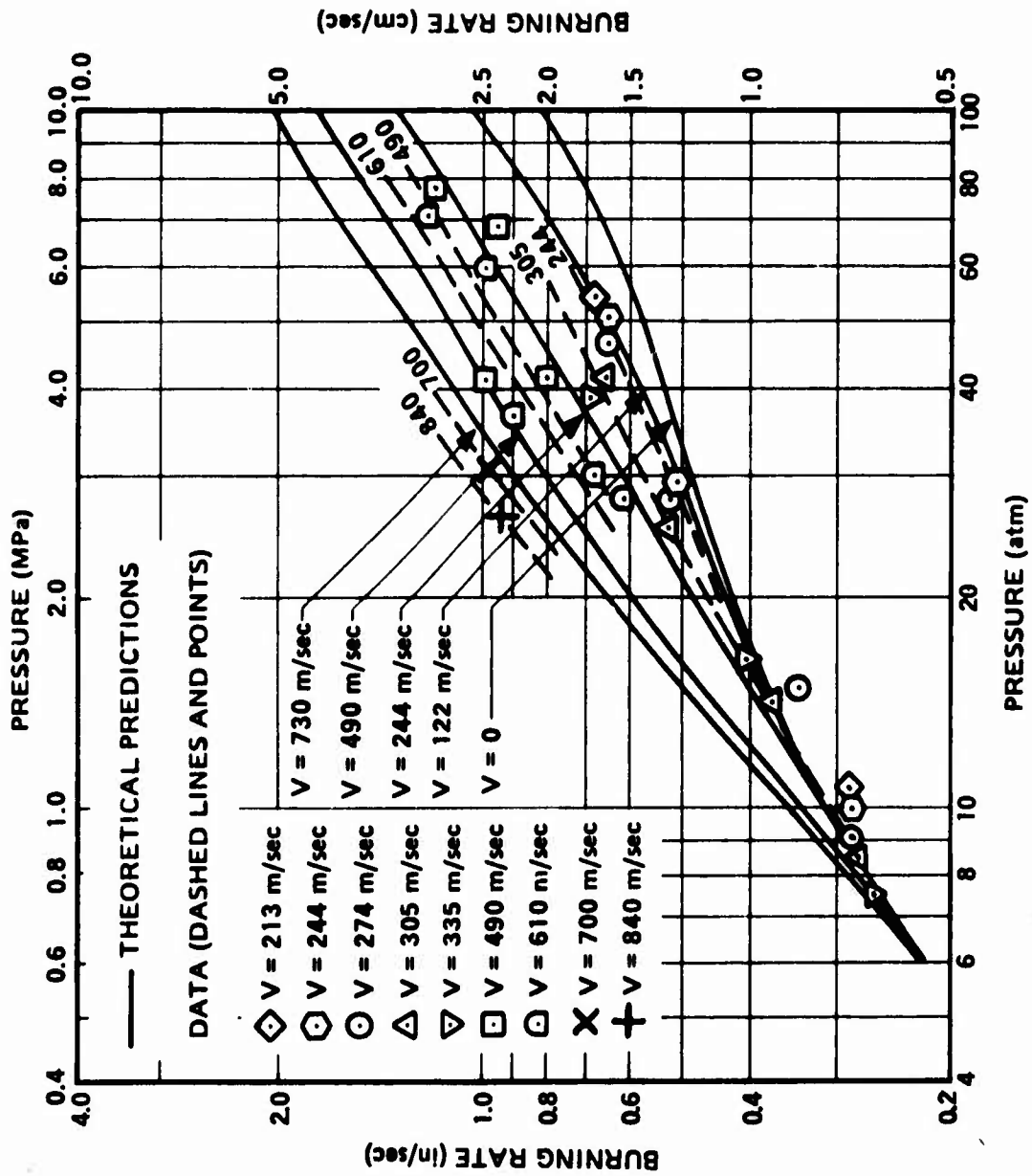


Figure II-19. Theoretical and Experimental Burn Rate - Pressure Relationships for Various Crossflow Velocities for Formulation 4869 (1667°K Formulation, 76/22/2 AP/HTPB/Fe<sub>2</sub>O<sub>3</sub>, 20 Micron AP).

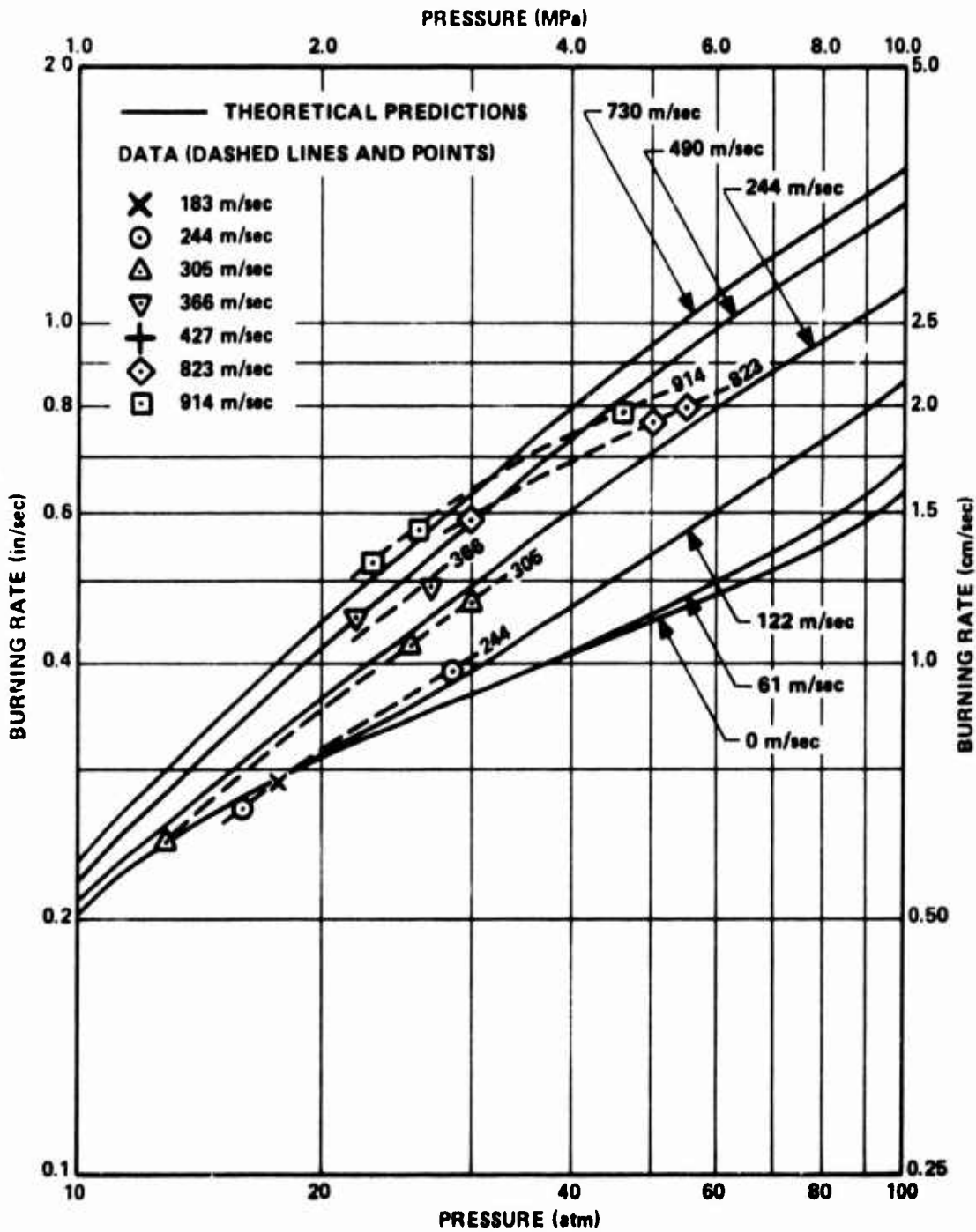


Figure II-20. Theoretical and Experimental Burn Rate - Pressure Relationships for Various Crossflow Velocities for Formulation 5542T (2065°K Formulation, 77/23 AP/HTPB, 20 Micron AP).

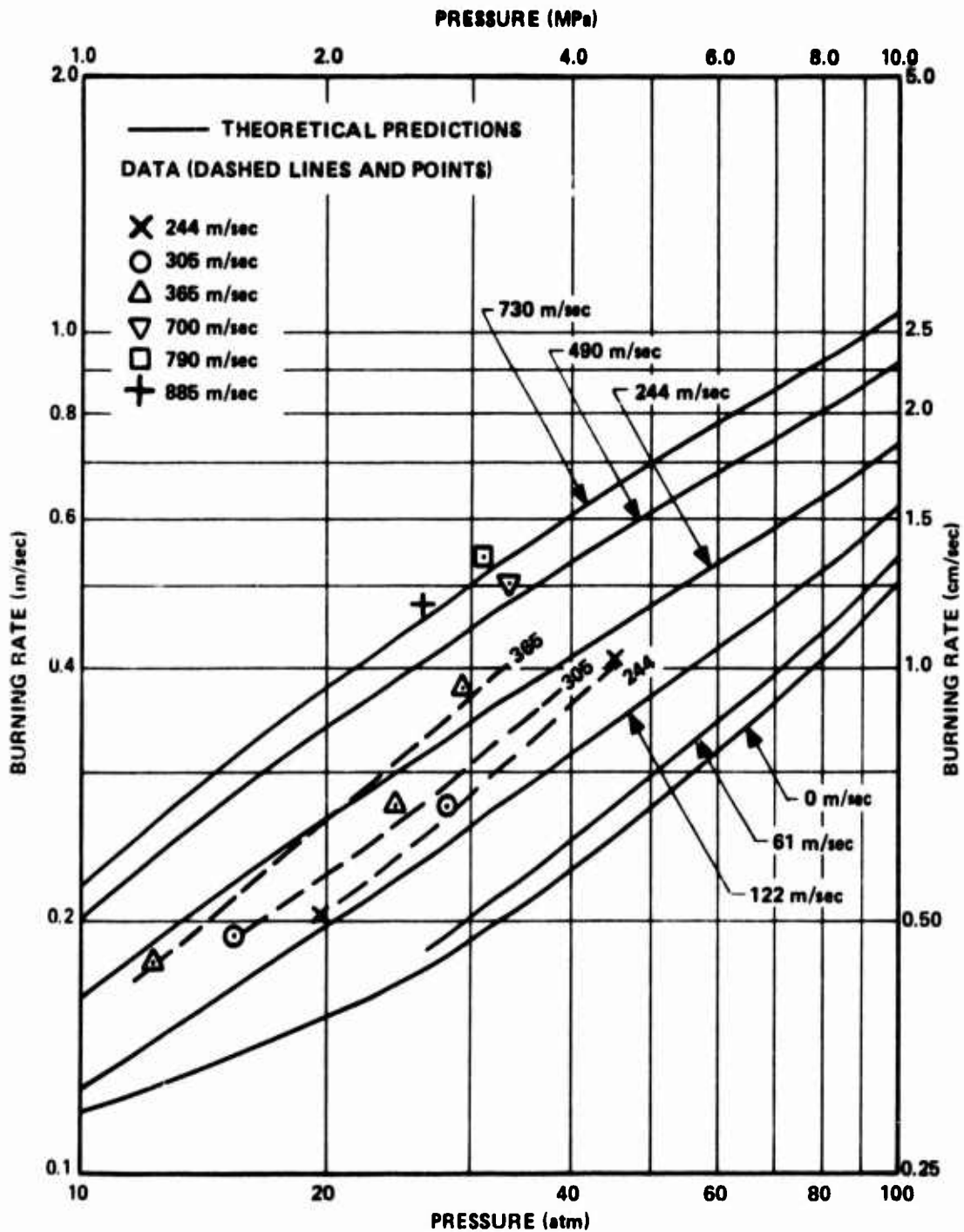


Figure II-21. Theoretical and Experimental Burn Rate - Pressure Relationships for Various Crossflow Velocities for Formulation 5565T (2575°K Formulation, 82/18 AP/HTPB, Bimodal With Sizes Chosen to Match 4525 Burning Rate).

are somewhat limited, but indicate reasonable agreement with theory, the formulation being quite sensitive to crossflows. Formulation 5555T (Figure II-22), a high burning rate formulation is predicted to be rather insensitive to crossflows: the data corroborates this prediction.

Next, let us compare results for the various formulations to identify parameters which influence the sensitivity of composite propellants to crossflows. Between Formulations 4525, 5051, and 4685, the only independent variable changed is the oxidizer particle size, composition being held constant. The change of oxidizer size, of course, leads to a change in base (no crossflow) burning rate versus pressure characteristics. Formulation 5051, containing 200 micron diameter AP is the slowest burning of the three formulations, with Formulation 4685 (5 micron AP) being the fastest and Formulation 4525 (20 micron AP) being intermediate. For instance, at 5 MPa (50 atmospheres) the base burning rate of 5051 is 0.47 cm/sec, that of 4525 is 0.68 cm/sec and that of 4685 is 1.15 cm/sec. Examination of Figures II-15, II-17, and II-18 indicates that the sensitivity of burning rate to crossflow increases with increasing particle size (decreasing base burning rate). For example, at a crossflow velocity of 200 m/sec (650 ft/sec) and a pressure of 5 MPa (50 atmospheres), the augmentation ratio for 4685 is about 1.10, that for 4525 is 1.65, and that for 5051 is 2.0.

Comparison of data for 4525 and 4869, two formulations of essentially the same oxidizer/fuel ratio, flame temperature, and oxidizer particle size, with the base burning rate being varied through use of catalyst in 4869, again shows an increase in sensitivity of burning rate to crossflow with a decrease in burning rate. At 5 MPa (50 atmospheres) the base burning rates for 4869 and 4525 are 1.40 cm/sec and 0.68 cm/sec, respectively. At this pressure, with a crossflow velocity of 200 m/sec (650 ft/sec) their  $r/r_0$  values are 1.10 and 1.65 respectively, while at 600 m/sec (1950 ft/sec), the  $r/r_0$  values are 1.75 and 2.3. Thus base burning rate is seen to affect the erosion sensitivity of composite propellants even at constant oxidizer particle size, erosive effects increasing with decreasing base burning rate.

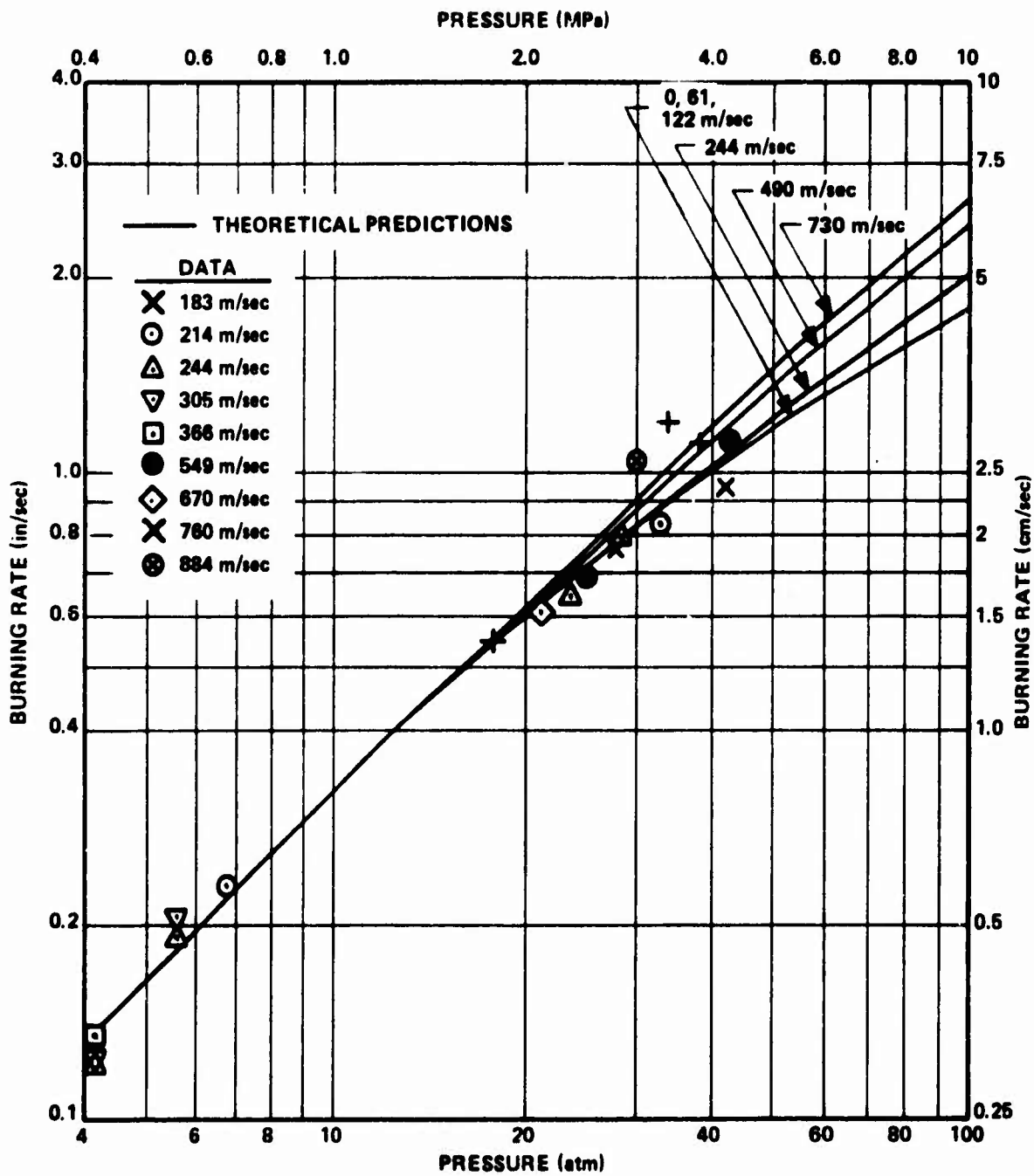


Figure II-22. Theoretical and Experimental Burn Rate - Pressure Relationships for Various Crossflow Velocities for Formulation 5555T (2575°K Formulation, 82/18 AP/HTPB, High Burn Rate).

Formulations 4685 and 4869 have approximately the same base burning rate at 8 MPa (80 atmospheres) with catalyst and oxidizer particle size effects on base burning rate roughly cancelling. Thus comparison of erosion sensitivity of these formulations at this pressure is of interest in that oxidizer particle size is varied (5 micron diameter for 4685, 20 micron diameter for 4869) while base burning rate is held constant. Comparison of data from Figures II-18 and II-19 indicates that these formulations have roughly the same sensitivity to the lower crossflow velocities tested at 8 MPa (80 atmospheres), with the catalyzed propellant being somewhat more sensitive at the higher crossflow velocities tested. Thus it appears that it is the base burning rate rather than the oxidizer particle size per se which dominates the sensitivity of composite propellants to erosive burning, though oxidizer size does have some further residual effect, erosion sensitivity decreasing with decreasing particle size at constant base burning rate.

Comparison of test results for Formulations 4525, 5542T and 5565T permits study of the effect of oxidizer/fuel ratio (and thus flame temperature) on erosion sensitivity, both at constant oxidizer particle size (5542T and 4525) and at constant base burning rate (5565T and 4525). Formulation 5542T differed from 4525 in oxidizer/fuel ratio (77/23 versus 73/27) and consequently flame temperature (2065°K vs. 1667°K). Since the oxidizer particle size was the same for both propellants, the higher oxidizer/fuel ratio for 5542T led to high base burning rate (1.14 cm/sec vs. 0.68 cm/sec at 5 MPa). Study of Figures II-15 and II-20 reveals that the erosion sensitivity of 5542T is considerably less than that of 4525 over the entire range of crossflow velocities studied (e.g.,  $r/r_o = 1.10$  for 5542T and  $1.65$  for 4525 at 200 m/sec, 5 MPa; and  $r/r_o = 1.7$  for 5542T and  $2.9$  for 4525 at 800 m/sec, 5 MPa). Thus we see that changing oxidizer/fuel ratio from very fuel-rich to less fuel-rich, with accompanying increase in flame temperature and burning rate leads to decreased sensitivity to erosive burning. Comparison of results for 5565T and 4525, which differ in oxidizer/fuel ratio but not in base burning rate (oxidizer particle size having been adjusted to compensate for the burning rate change with changing oxidizer/fuel) permits separation of the effects of varying oxidizer/fuel (and thus flame temperature) from the effects of base burning rate. As may be seen by study of Figures

II-15 and II-21, the sensitivity of Formulations 5565T and 4525 to crossflow are nearly the same. For instance, at 200 m/sec (650 ft/sec) crossflow velocity and 5 MPa (50 atmospheres), the augmentation ratios for 5565T and 4525 are 1.50 and 1.65, respectively, while at 800 m/sec (2600 ft/sec) and 3 MPa (30 atmospheres), they are 2.65 and 2.50. Accordingly, we may conclude that oxidizer/fuel ratio (and consequently flame temperature) does not directly affect the erosion sensitivity of the composition studied to date, but only affects it through its effect on base burning rate.

Formulations 5555T and 5565T had the same composition, differing only in oxidizer particle size, which was adjusted in 5555T to give a very high burning rate. Again, the effect on erosion sensitivity of increased base burning rate can be seen in comparison of Figures II-21 and II-22. At 5 MPa (50 atmospheres), the base burning rates of 5555T and 5565T are 2.94 and 0.70 cm/sec, respectively. At 200 m/sec (650 ft/sec) crossflow velocities, the respective values of  $r/r_0$  are 1.0 and 1.5, while at 700 m/sec (2300 ft/sec), they are 1.2 and 2.4. Thus, once again, erosion sensitivity is seen to decrease with increasing base burning rate.

#### D. Conclusions

An experimental apparatus for measurement of erosive burning rates over a wide range of crossflow velocities, up to Mach 1 has been designed, constructed and checked-out. Erosive burning characteristics of seven formulations, with systematically varied properties, have been measured in this test device and checked against predictions of a first generation composite propellant erosive burning model based upon the bending of columnar diffusion flames. In general, the model appears to give reasonably good agreement with measured erosive burning data, except under conditions where the heterogeneity of the composite propellant is unimportant (low pressure, high crossflow velocity). Here, it appears that an additional mechanism(s) of erosive burning will have to be considered. The data indicate that the base (no crossflow) burning rate versus pressure characteristics of the propellant have a predominant effect on its sensitivity to erosive burning, high burning rate propellants being considerably less sensitive to crossflow than low burning rate formulations, whether the burning rate alterations

are produced by oxidizer particle size variation, oxidizer/fuel ratio variation, or use of catalysts. Oxidizer particle size appears to have some effect (but not a great one) beyond its effect on base burning rate, augmentation ratio increasing with increasing particle size. Oxidizer/fuel ratio (and thus flame temperature) appears to affect erosion sensitivity only through its effect on base burning rate.

The first generation erosive burning model described in this report requires no-crossflow burning rate versus pressure data as input: a second generation model for composite propellants containing unimodal oxidizer (still based upon bending of columnar diffusion flames) which does not require such data, but only composition and ingredient particle size data, has been developed and appears to give reasonable burning rate-pressure-crossflow velocity predictions for the one formulation against which it has been tested. Optimization of this model with respect to selection of several kinetic constants appearing within it has not been completed. In addition, the model has not yet been extended to the more useful case of multimodal oxidizer particle sizes.

A review of the literature indicates that the boundary layer profiles in rocket motors may differ significantly from those in typical erosive burning test devices. Comparison of erosive burning calculations using the first generation erosive burning model described in this report with profiles expected to prevail in the test apparatus versus those estimated to exist in cylindrically perforated motor grains indicate that erosive burning may be considerably less for a given mainstream crossflow velocity in such a motor than in a typical erosive burning testing apparatus, indicating a strong need for further study of boundary layer profiles in the near-wall region in rocket motor grain ports.

### III. MODELING OF ALUMINUM PARTICLE COMBUSTION IN CARBON DIOXIDE-NITROGEN MIXTURE, ALLOWING FOR FINITE-RATE KINETICS FOR THE ALUMINUM VAPOR-CARBON DIOXIDE GAS-PHASE REACTION

#### A. Introduction and Background

Over the past 20 years, numerous models have been developed for the combustion of metal particles or droplets, with varying degrees of sophistication of the treatment of oxide product condensation.<sup>(1-5)</sup> In all of these models, a flame sheet approximation was used; that is, metal vapor and oxidizer were assumed to react at an infinite rate in an infinitesimally thin zone removed some distance from the particle surface. Thus, the physical processes of diffusion of the metal vapor and oxidizer species were assumed to limit the rate of combustion. Such an assumption, in the absence of detailed consideration of the complex temperature dependency of equilibrium species concentrations in the  $Al_xO_y$  system, results in a "d<sup>2</sup>-law" for combustion:

$$d_o^2 - d^2 = K\theta \quad (1)$$

$d_o$  = initial particle diameter

$d$  = particle diameter at time  $\theta$

$\theta$  = time from beginning of combustion

$K$  = proportionality constant, function of temperature and gas composition.

Maček<sup>(6)</sup> has experimentally obtained burning time data for single aluminum particles as a function of their initial diameter which seem to follow such a d<sup>2</sup>-law. Pokhil,<sup>(7)</sup> on the other hand, has observed aluminum combustion to more closely follow a d<sup>1.5</sup>-law. (Since kinetically controlled combustion of metal particles may be shown to imply a d<sup>1</sup>-law, Pokhil's observations may be interpreted as implying burning behavior which is partly kinetics-controlled and partly diffusion-controlled: that is, a finite resistance due to each process must be considered.)

The question of what particle size power law is applicable to aluminum particle combustion is important since, due to resolution limitations, single particle combustion experiments have been conducted mostly

with particles on the order of 50 microns diameter or larger, while aluminum particles used in solid propellants are typically on the order of 5 to 10 microns in diameter (in the absence of agglomeration). Assuming that a 50 micron particle burns in 20 milliseconds under a given set of conditions, use of a  $d^1$ , a  $d^{1.5}$  or a  $d^2$ -law leads to predicted combustion times for a 5 micron particle of 2.0, 0.63 and 0.20 msec, respectively, a rather large range of times. Accordingly, predictions of aluminum particle combustion efficiency in typical low residence time tactical rocket motors are strongly dependent on the assumed particle-size combustion-time power law.

Recently, Fontijn<sup>(8)</sup> measured kinetic data for the reactions of aluminum vapor with  $\text{CO}_2$  and  $\text{O}_2$  in a fast-flow tubular reactor experiment. The reaction,  $\text{Al(g)} + \text{CO}_2 \rightarrow \text{AlO} + \text{CO}$ , was found to be first order with respect to aluminum vapor and first order with respect to carbon dioxide, with a complex dependency of the rate constant on temperature, as shown in Table III-I. Using preliminary Fontijn data, which indicated a rate constant of approximately  $10^{-11} \text{ cm}^3/\text{molecule second}$ , independent of temperature, this author performed calculations, described in detail in Reference 9, to evaluate the validity of the infinite-rate-kinetics assumption with respect to calculation of aluminum particle combustion rates. Two levels of analysis were carried out, the first being a very simple estimate of the flame zone thickness and the second involving development of a simplified droplet combustion model.

In the first analysis, a rough estimate was made of the required volume (and thus thickness) of flame zone required for quasi-steady-state consumption of  $\text{CO}_2$  by aluminum vapor (using Fontijn's kinetic data) with the  $\text{CO}_2$  being supplied at a diffusion-limited rate from the surroundings. In this calculation, a mass transfer Nusselt Number of 2 (based on the flame diameter) was assumed. In addition, it was assumed that the average aluminum vapor concentration and  $\text{CO}_2$  concentration in the reaction zone were equal and each was approximately ten to thirty percent of the freestream  $\text{CO}_2$  concentration. With these assumptions, the following approximate expression, based on a mass balance on  $\text{CO}_2$ , was derived for the flame zone thickness:

$$\Delta = \frac{82.05 D T_{\infty}}{(r_s + \delta) k P y_{CO_2, \infty}} \left( \frac{y_{CO_2, \infty}}{y_{CO_2, \text{rx zone}}} \right)^2 \quad (2)$$

$\Delta$  = estimated reaction zone thickness (cm)

$D$  = diffusivity ( $\text{cm}^2/\text{sec}$ )

$T_{\infty}$  = ambient temperature ( $^{\circ}\text{K}$ )

$y_{CO_2, \infty}$  = ambient carbon dioxide mole fraction

$y_{CO_2, \text{rx zone}}$  = "average" carbon dioxide mole fraction in reaction zone.

$P$  = pressure (atm)

$k$  = rate constant for  $\text{Al}(\text{g}) + \text{CO}_2 \rightarrow \text{AlO} + \text{CO}$  ( $\text{cm}^3/\text{mole sec}$ )

$r_s$  = particle radius (cm)

$\delta$  = average flame offset distance (cm).

Results for a set of calculations with pressure equal to one atmosphere, ambient temperature of  $300^{\circ}\text{K}$ , ambient  $\text{CO}_2$  mole fraction of 0.2, average flame radius equal to 1.10 times the particle radius, and diffusivity equal to  $2.1 \text{ cm}^2/\text{second}$  are presented in Table III-II. As may be seen, these calculations indicate that at least for particle sizes below 20 to 40 microns (depending upon what one accepts as a reasonable value of the ratio of "average" concentrations in the flame region to free-stream  $\text{CO}_2$  concentration), the assumption that the reaction zone thickness is small compared to the particle size is poor. However, without further analysis, it is impossible to define just what a meaningful "average" reaction zone concentration is or to estimate the effect of a given reaction zone thickness on burning rate. Accordingly, the question of the effect of use of finite-rate kinetics for the metal vapor oxidation process on predictions of aluminum droplet burning rates was examined further by use of a hydrocarbon droplet burning rate model capable of treating finite rate oxidation kinetics.

The treatment employed was quite similar to that used by Peskin and coworkers<sup>(10,11)</sup> for the analysis of the combustion of hydrocarbon fuel droplets. The major shortcoming involved with using such a model for treatment of aluminum combustion was that it does not properly treat product condensation effects which are known to be important in the combustion of aluminum.

TABLE III-I. Rate Constant Data obtained by Fontijn in a Fast-Flow Tubular Reactor for the Reaction,  $\text{Al(g)} + \text{CO}_2 \rightarrow \text{AlO} + \text{CO}$ .

<u>Rate Constant, k(cc/molecule second)</u>	<u>Temperature °K</u>
1.5 ( $10^{-13}$ )	310
6.9 ( $10^{-13}$ )	480
1.6 ( $10^{-12}$ )	730
9.0 ( $10^{-12}$ )	1470
3.8 ( $10^{-11}$ )	1830

TABLE III-II. Estimated Reaction Zone Thicknesses for Aluminum Particles Burning in Carbon Dioxide, with Use of Fontijn Rate Data for  $\text{Al(g)} + \text{CO}_2 \rightarrow \text{AlO} + \text{CO}$

Pressure = 1 atmosphere  
 Ambient Temperature = 300°K  
 Ambient  $\text{CO}_2$  Mole Fraction = 0.2

<u>Particle Radius (<math>\mu</math>)</u>	<u>Reaction Zone Thickness (<math>\mu</math>)</u>	
	<u>Assuming</u>	<u>Assuming</u>
	$Y_{\text{CO}_2, \text{ Rx zone}}/Y_{\text{CO}_2, \infty}$	$Y_{\text{CO}_2, \text{ Rx zone}}/Y_{\text{CO}_2, \infty}$
	<u>= 0.1</u>	<u>= 0.3</u>
50	8	0.89
40	10	1.11
30	13.3	1.48
20	20	2.22
10	40	4.45
5	80	8.90

However, it was felt that even though use of such a model would not give accurate quantitative burning rate predictions, it would permit examination of the effect of use of finite rate kinetics for the vapor phase oxidation step versus use of infinite kinetics (flame sheet assumption), by comparison of predicted burning rates with use of the Fontijn rate expression in the derived equations versus burning rates calculated with use of a very high rate constant (approaching infinity) in the same equations.

In this preliminary model developed for study of the effects of finite kinetics on predicted aluminum particle burning rate, the surrounding gases were assumed to be a mixture of  $\text{CO}_2$  and  $\text{N}_2$ . The overall oxidation reaction, as far as heat release was concerned, was assumed to be  $3/2 \text{CO}_2 + \text{Al}(\text{g}) \rightarrow 3/2 \text{CO} + 1/2 \text{Al}_2\text{O}_3 (\text{l})$ , with the reaction  $\text{Al}(\text{g}) + \text{CO}_2 \rightarrow \text{AlO} + \text{CO}$  being the limiting reaction, all succeeding steps being fast in comparison. (This assumption of fast succeeding steps, particularly condensation, was obviously a poor one and must be removed in any detailed analysis. This question was studied in-depth as a major part of the aluminum particle combustion modeling part of the current program.) In addition, the product,  $\text{Al}_2\text{O}_3$ , although being treated as a liquid as far as heat release was concerned, was treated as a gas in terms of its density and transport properties in order to permit use of the Shvab-Zeldovich equation formulation. The Lewis numbers of all species were assumed to be unity (also necessary for use of the Shvab-Zeldovich formulation. The purpose of these assumptions was to permit reduction of  $n + 1$  second order differential equations (where  $n$  is the number of chemical species involved) to one second order differential equation plus  $n$  algebraic equations (the Shvab-Zeldovich formulation). Without the assumption that all species behave in terms of transport as gases with a Lewis Number of unity, the second order differential equations were not similar, and thus could not be reduced to one second order differential equation. Since solution of these equations involves solution of a two-boundary eigen-value problem, the reduction from  $n + 1$  differential equations to one differential equation resulted in a tremendous simplification of the solution procedure. In addition, for further mathematical simplification, properties such as specific heat, thermal conductivity, and density-diffusivity product were assumed to be independent of position in the analysis.

Details of the equation development and solution procedure for this simplified model are presented in Reference 9. From this analysis, particle burning rates were calculated as a function of particle size for a given ambient temperature, pressure, and ambient gas composition. These calculations resulted in plots of burning rate versus particle size for finite and infinite kinetics. Numerical integration was then performed to calculate the burning time of a particle of given initial size as:

$$\tau_{\text{burn}} = \int_0^{r_{s,0}} \frac{dr_s}{(\text{linear burning rate})}$$

for both finite and infinite kinetics cases. Results of a set of calculations for  $P = 1$  atmosphere,  $T_{\text{ambient}} = 2000^\circ\text{K}$ , and  $y_{\text{CO}_2, \text{ambient}} = 0.5$  are presented in Figure III-1 in the form of burn time versus initial particle diameter on a log-log plot.

As may be seen, for infinite rate kinetics the particle combustion is predicted to follow a  $d^2$ -law. However, with the finite rate kinetics treatment using Fontijn's preliminary data, the burn time versus initial particle diameter predicted behavior is somewhat more complex, with a shift from approximately  $d^2$ -law behavior for particles in the  $100\mu$  initial diameter range to approximately  $d^1$ -law behavior in the 10 to  $20\mu$  initial diameter range. Thus, the retarding effect of finite rate kinetics is quite important for the smaller particle sizes. In fact, use of an infinite rate oxidation kinetics (flame sheet) model to extrapolate  $100\mu$  diameter data to  $10\mu$  initial particle diameter results in underprediction of the burn time compared to that calculated using Fontijn's preliminary data by a factor of 4 to 5 for the cases studied.

Thus it appears that the flame-sheet approximation for the reaction of metal vapor and oxidizer used in existing aluminum combustion models is a poor one, resulting in large errors in predicted burning times of small (less than 20 to 30 micron diameter) aluminum particles, the degree of error increasing rapidly as the particle size is further decreased. Accordingly, as described below, an advanced model including treatment of the kinetics of the metal vapor oxidation process (along with the condensation processes which was not really treated in the above preliminary analysis) was developed on this program.

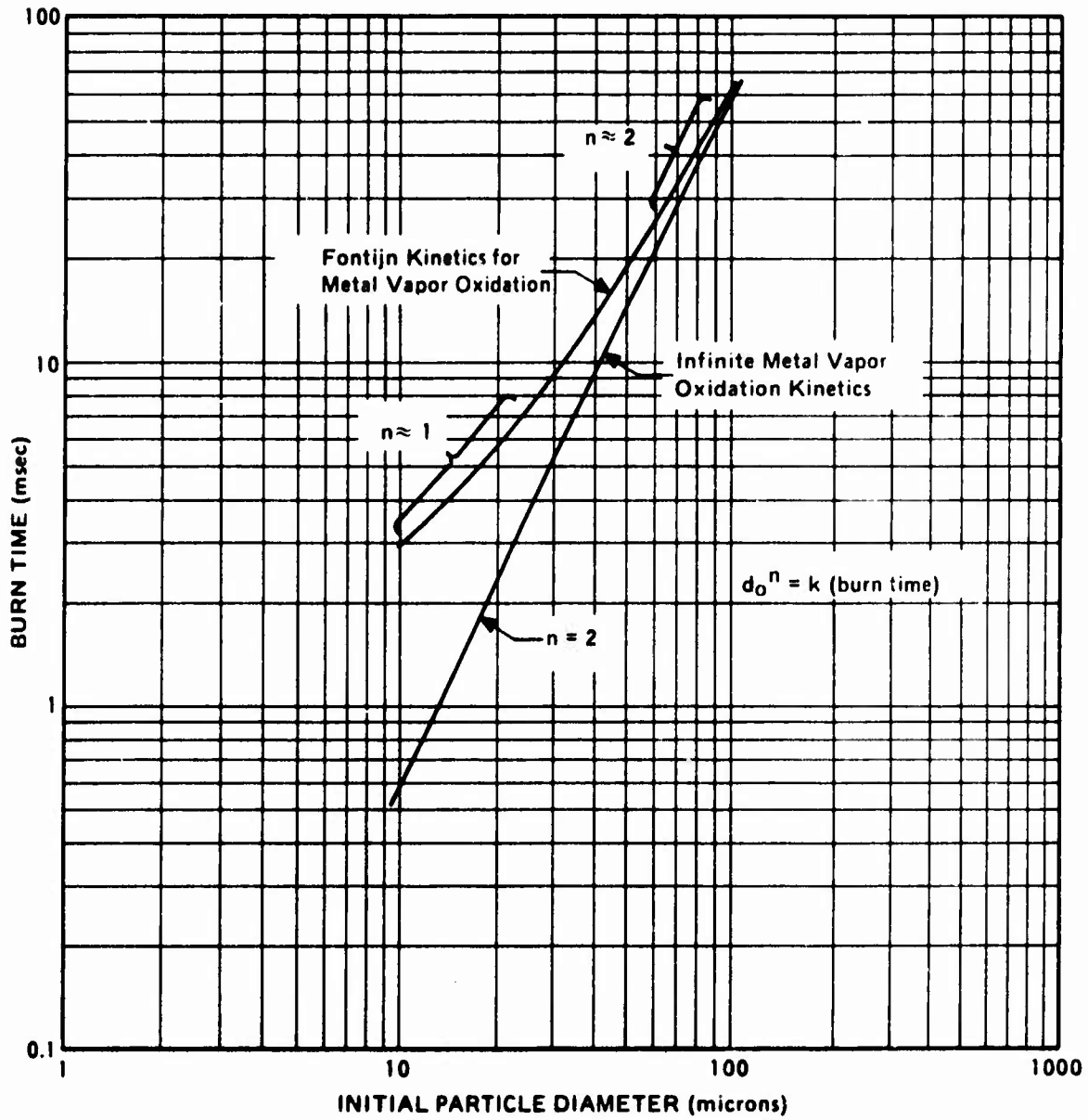
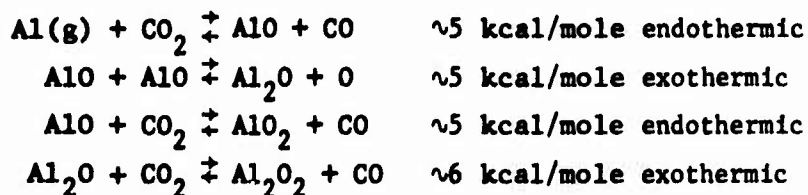


Figure III-1. Predicted Burn Time as a Function of Particle Size For Aluminum Particles,  $T_{\text{AMBIENT}} = 2000^{\circ}\text{K}$ ,  $Y_{\text{CO}_2, \text{AMBIENT}} = 0.5$

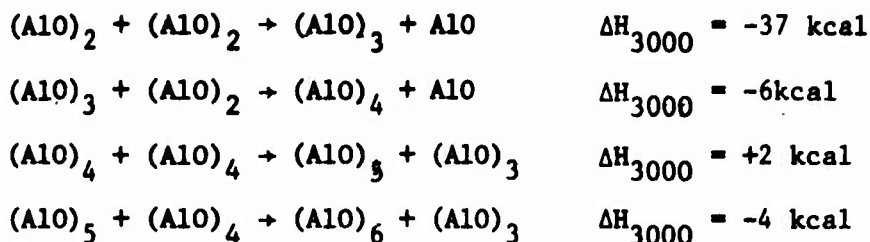
## B. Development of Physical Picture

As mentioned above, in the preliminary simplified analysis, all reactions subsequent to the gas-phase oxidation of aluminum vapor via  $\text{Al(g)} + \text{CO}_2 \rightarrow \text{AlO} + \text{CO}$ , including condensation of  $\text{Al}_2\text{O}_3(\ell)$ , were assumed to be infinitely fast. Among other problems resulting from such an assumption is the prediction of very high temperature regions (with temperatures well in excess of 5000°K) due to release of heat in the condensation of  $\text{Al}_2\text{O}_3(\ell)$ . At such temperatures, however,  $\text{Al}_2\text{O}_3(\ell)$  will be endothermically dissociated into such species as  $\text{AlO}$ ,  $\text{AlO}_2$ ,  $\text{Al}_2\text{O}$ , etc., with a resultant lowering of temperature. That is, the temperature is limited by the dissociative behavior of  $\text{Al}_2\text{O}_3(\ell)$ , and this feature must somehow be incorporated into any physically realistic model.

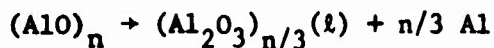
As part of the development of a physical picture of processes occurring during aluminum particle combustion in carbon dioxide atmospheres, a procedure described by Henderson<sup>(11)</sup> was used to identify likely reactions in the gas-phase. The key point to this procedure is the imposition of two criteria to identify likely important reactions. First, only two-body collision reactions are considered because of their much higher probability than three-body collisions. Secondly, it is required that the absolute value of the heat of reaction be small in order for a reaction to be likely. (If the reaction is highly endothermic, the fraction of sufficiently energetic reactant molecules will be extremely low, while if the reaction is highly exothermic, the energy release will result in dissociation of the product molecule[s].) Under these guidelines, four possibly significant gas-phase reactions are identified for the aluminum-carbon dioxide-nitrogen system:



As seen, none of these reactions yield  $\text{Al}_2\text{O}_3(\ell)$ : the path to this final product is not clear. Both homogeneous and heterogeneous processes may be postulated. For homogeneous condensation, Henderson has proposed a series of polymerization reactions as follows:



in combination with formation of liquid  $\text{Al}_2\text{O}_3$  by evolution of aluminum vapors from the AlO polymers:



where n must be large to keep the heat of reaction small. This author is not aware of any experimental evidence supporting this scheme. Moreover, it is a rather complex multistep scheme which as a consequence is probably rather slow. (Quantitative estimates cannot be made since there are no rate data available for any of the reactions postulated.) Consequently, it appears more likely that most or all of the condensation occurs by heterogeneous processes as discussed below, with reaction sites being supplied by initial aluminum oxide shed from the parent aluminum particle, further condensed phase alumina product trapped in a ring around the particle during its burning, and possibly carbon particles resulting from partial breakdown of CO in the fuel-rich regions near the particle.

Returning to the four likely gas-phase reactions listed above, rate data obtained by Fontijn for the first reaction are available, as mentioned earlier. (See Table III-I.) For this model development, Fontijn's data have been fit to a modified Arrhenius expression,

$$k = 7.8(10)^{-13} T^{1/2} \exp(-1500/T) \quad (3)$$

k = rate constant ( $\text{cm}^3/\text{molecule second}$ )

T = temperature ( $^{\circ}\text{K}$ )

with the rate being first order with respect to  $\text{CO}_2$  concentration and first order with respect to aluminum vapor concentration. Unfortunately, no kinetic data are available for the other three reactions. Accordingly, it was originally intended to examine two limiting cases with respect to these reactions:

(1) reactions negligibly slow; and (2) reactions sufficiently fast to be treated as equilibrium reactions. Unfortunately, time and financial limitations permitted examination of only one of these cases. Comparative estimates of rates of all four of the reactions based on the procedures of Benson<sup>(13)</sup> indicate that the second, third, and fourth reactions should be two to three orders of magnitude slower than that of the  $\text{Al(g)} + \text{CO}_2 \rightarrow \text{AlO} + \text{CO}$  reaction. Accordingly, it was decided that the limiting case of  $\text{AlO} + \text{AlO} \rightarrow \text{Al}_2\text{O} + \text{O}$ ,  $\text{AlO} + \text{CO}_2 \rightarrow \text{AlO}_2 + \text{CO}$ , and  $\text{Al}_2\text{O} + \text{CO}_2 \rightarrow \text{Al}_2\text{O}_2 + \text{CO}$  all being negligibly slow be modeled.

Next, we must examine the question of heterogeneous condensation of  $\text{Al}_2\text{O}_3(\ell)$ . One possible condensation site is obviously the surface of the parent aluminum particle itself. In addition, one may logically postulate the existence of a fairly thin shell region some distance from the particle surface at which virtually all of the  $\text{Al}_x\text{O}_y$  gas species condense (with  $\text{CO}_2$  supplying makeup oxygen as needed to satisfy stoichiometry constraints) to  $\text{Al}_2\text{O}_3(\ell)$ . Provided that no more than about one-third of the aluminum burning condenses at the surface (see later discussion), there is a net gas flow away from the surface of the particle as it burns. However, at large distances from the particle, outside the region(s) of oxide condensation, the net gas flow is toward the particles. As a result, there is some radius at which the net gas mass flux is zero. Any particles formed inside or outside this region will tend to be convected to this radius. Thus, one can easily visualize a sink radius where condensed-phase species will tend to gather. These species will then serve as sites for heterogeneous condensation at that radius. Now let us consider the location of this "condensation radius." If we choose a radius too close to the particle, condensation of aluminum oxide there in a relatively small area (the surface area associated with the shell at the condensation radius is proportional to the square of that radius) will lead to very high temperatures, above the dissociation temperature of the aluminum oxide and thus condensation will not be able to occur there. As the chosen radius is increased, the temperature associated with condensation of oxide at that radius decreases. It seems likely that some supercooling of the vapor will be required for condensation (certainly so if one wishes to simplify the picture by considering a thin rather than

broad condensation zone for mathematical simplification). Accordingly, in the model described below, the "condensation radius" was chosen as one which would result in a temperature at that radius, with condensation of all  $Al_xO_y$  species there, of a specified value. (3000°K and 3500°K cases were examined.) Treatment of a broad condensation zone rather than an infinitesimally thin one, with the temperature being held constant across the zone through variation of the fraction of  $Al_xO_y$  condensed across the zone would probably be more realistic than the thin condensation treatment employed herein; however, it does not appear likely that the calculated burning rates would be strongly changed, and the mathematical analysis is greatly simplified through use of the thin condensation zone treatment.

Next, let us examine possible processes occurring at the surface. Within the constraints of limiting the gas phase chemistry to  $Al(g) + CO_2 \rightarrow AlO + CO$ , there are three possible major surface reaction processes:

- (1) Vaporization of aluminum liquid.
- (2) Reaction of  $CO_2$  and/or  $AlO$  with liquid aluminum at the surface to yield  $Al_2O(g)$ .
- (3) Reactive condensation of  $Al_2O$  and/or  $AlO$  at the surface to yield  $Al_2O_3(l)$  which then remains on the surface.

The first process, vaporization of liquid aluminum, is obviously of importance and must be considered in any model of aluminum droplet combustion. Heat must be supplied either from heat feedback from the outer zones (most importantly the outer condensation zone) or from the exothermic reactions in Categories 2 and 3.

The reaction of  $AlO$  with  $Al(l)$  at the surface via the reaction:



not only aids in the consumption of the aluminum particle through direct removal of liquid aluminum from the surface but, being exothermic by approximately 55 kcal/mole, also releases heat for vaporization of additional liquid aluminum. The reaction of  $CO_2$  with  $Al(l)$  at the surface via:



directly removes two moles of aluminum from the particle per mole of  $CO_2$  reacting there, but is slightly endothermic, thus requiring heat from the

AlO-Al reaction or from the outer regions. Two cases were examined in the course of this modeling effort: in the first, both the AlO-Al and CO<sub>2</sub>-Al surface reactions were assumed to occur with infinite kinetics; while in the second, the CO<sub>2</sub>-Al surface reaction was prohibited. It is not clear which of these scenarios is most realistic.

The question of condensation of aluminum oxide at the surface appears to be quite a controversial one. Preliminary thermodynamic analysis with estimated values of surface temperature indicated that thermodynamically Al<sub>2</sub>O<sub>3</sub> should not be formed at the surface, the reaction  $3\text{Al}_2\text{O}(\text{g}) \rightleftharpoons \text{Al}_2\text{O}_3(\text{l}) + 4\text{Al}(\text{l})$  being shifted all the way to the left for reasonable values of Al<sub>2</sub>O partial pressure adjacent to the surface. However, there are considerable references in the literature to the existence of Al<sub>2</sub>O<sub>3</sub> on burning aluminum particle surfaces. While in most of these references it is not clear whether the Al<sub>2</sub>O<sub>3</sub> on the surface comes from initial Al<sub>2</sub>O<sub>3</sub> formed in preignition and ignition phases or whether it is actually built up during the combustion process, several (e.g., References 14 - 16) clearly state that oxide accumulates on the surface during the self-sustained combustion. It is interesting, however, to note that no such oxide formation on the surface is observed in combustion of particles in O<sub>2</sub>/Argon and oxygen-rich O<sub>2</sub>/CO flames.<sup>(17)</sup> In line with this, Prentice<sup>(18)</sup> suggests that nitrogen and carbon appear to be important factors in causing accumulation of oxide (and nitride ?) on the surface. It should be pointed out that these observations and conclusions regarding aluminum oxide accumulation on burning aluminum particles are, in general, based on experiments with rather large (greater than 100 micron diameter) aluminum particles. A particularly interesting conclusion regarding the dependency of oxide accumulation on initial particle size is presented in Reference 19. In this report, a plot of weight fraction of initial aluminum appearing in the final residue globule after burning versus original particle diameter is presented for the case of aluminum particles burning in 1 atmosphere 50/50 O<sub>2</sub>/N<sub>2</sub> environment. This plot indicates that this weight fraction decreases with decreasing initial particle diameter. Extrapolation of the data indicates that for initial particle diameters below about 100 microns, no accumulation will occur. Since the model development on this program was aimed at small particles (60 micron diameter or less) where kinetic effects

are more likely to be important relative to diffusion effects, it was decided that oxide condensation on the burning particle surface be neglected in this modeling. Outputs of the model(s) discussed below include such parameters as surface temperature and gas phase composition adjacent to the particle surface. With these, the validity (in terms of thermodynamics) of the assumption of no condensed oxide formation at the surface can be checked. Interestingly enough, the assumption was found to break down only for the larger particles, in line with the trend observed by Prentice of fractional surface oxide accumulation increasing with increasing initial particle size.

The final physical picture modeled is sketched in Figure III-2. Actually, two models were developed, differing only in the assumption of infinitely fast or infinitely slow reaction kinetics for the reaction of  $\text{CO}_2$  with liquid aluminum at the particle surface to form  $\text{Al}_2\text{O}$  and  $\text{CO}$ . Each model is divided into two regions, an inner region and an outer region, separated by a condensation zone. There are no reactions in the outer region, where the only species considered are  $\text{CO}$ ,  $\text{CO}_2$ , and  $\text{N}_2$ .  $\text{CO}$  and heat are transferred outward from the condensation zone in this region while  $\text{CO}_2$  is transferred inward. At the surface, aluminum vapor is boiled off, using heat supplied by feedback from the outer regions and by the infinitely fast exothermic  $(\text{AlO}) + \text{Al}(\ell) \rightarrow \text{Al}_2\text{O}$  reaction. In addition, aluminum is removed from the surface as  $\text{Al}_2\text{O}$  by this reaction and, in one of the model versions, by the reaction  $\text{CO}_2 + 2\text{Al}(\ell) \rightarrow \text{Al}_2\text{O} + \text{CO}$ . In the inner region, between the particle surface and the condensation radius, aluminum vapor reacts with  $\text{CO}_2$  at a rate determined by the previously described rate expression derived from the data of Fontijn. Convection and diffusion of all species and conduction and convection of sensible enthalpy are treated. All  $\text{Al}_x\text{O}_y$  species transported to the condensation radius react infinitely rapidly there with  $\text{CO}_2$  supplied from the outer region to form  $\text{Al}_2\text{O}_3(\ell)$  which is then trapped there. Heat released from these condensation reactions is transferred in either direction away from this zone. The condensation radius is chosen by a trial and error procedure to yield a specified temperature at that radius. (The further out the condensation radius, the lower the temperature.) Two values (3000°K and 3500°K) of condensation temperature, somewhat below the atmospheric decomposition temperature of  $\text{Al}_2\text{O}_3$  (approximately 3700 to 3900°K, depending on composition) were chosen for parametric study.

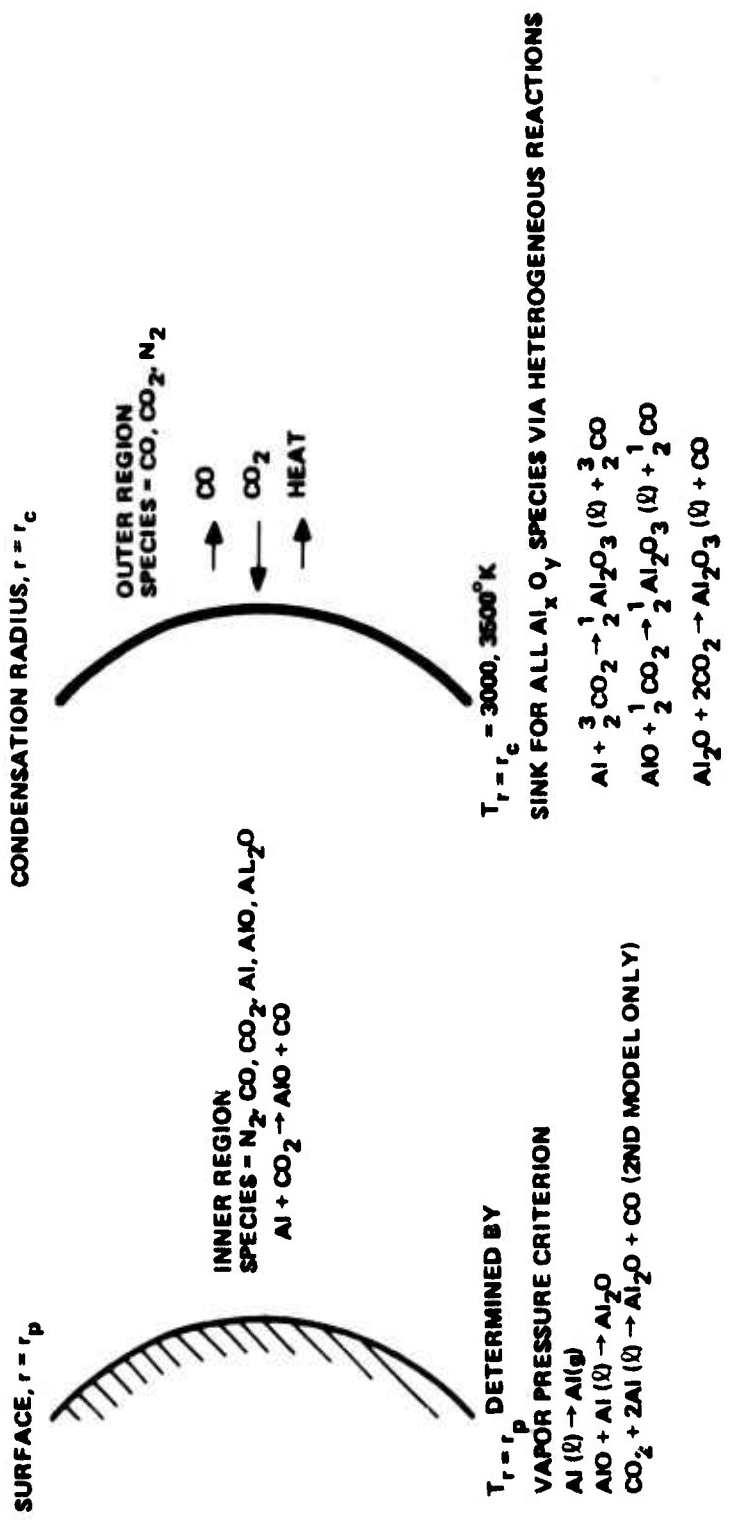


Figure III-2. Schematic of Single Particle Aluminum Combustion Model(s) Developed in This Study.

C. Model Development

As mentioned above, two models of single particle aluminum combustion were developed during the course of this program, the only difference being allowance or prohibition of an infinitely fast reaction of  $\text{CO}_2$  with aluminum liquid at the burning particle surface. As a result, the conservation equations in the inner and outer regions are the same in each model as are the condensation radius boundary conditions used to connect the inner and outer regions. The only difference occurs in the boundary conditions at the particle surface.

In the outer region ( $r > r_c$ , the condensation radius) there are only three chemical species,  $\text{CO}_2$ ,  $\text{CO}$ , and  $\text{N}_2$ . Since the problem is formulated as a quasi-steady-state one, it may easily be shown that the overall molar flux in this region is zero since there must be no net flux of carbon or nitrogen atoms to  $r = r_c$  and since  $\text{CO}$  and  $\text{CO}_2$  each contain one carbon atom. In addition, there are no reactions allowed in the outer regions. Accordingly, the species conservation equations for  $\text{CO}$ ,  $\text{CO}_2$  and  $\text{N}_2$  in the outer region reduce simply to:

$$\frac{d}{dr} \left( r^2 c D \frac{\partial y_j}{\partial r} \right) = 0, \quad j = \text{CO}, \text{CO}_2, \text{N}_2 \quad (4)$$

where:

- $r$  = radius
- $c$  = total molar concentration
- $y_j$  = mole fraction of species  $j$
- $D$  = diffusivity.

Substituting  $y_j = P_j/P$  and  $C = \rho/MW$  (where  $P_j$  is the partial pressure of species  $j$ ,  $\rho$  is the overall gas density, and  $MW$  is the overall gas molecular weight) and assuming that the density-diffusivity product is essentially independent of position, we arrive at, following integration of Equation 4:

$$\frac{r^2}{P(MW)} \frac{\partial P_j}{\partial r} = k_j \quad (5)$$

where  $k_j$  is a constant to be evaluated from application of boundary conditions and is different for each species. (Since  $\text{N}_2$  is the only nitrogen-containing species and the net molar flux of  $\text{N}_2$  must be zero for quasi-steady-state conditions to apply, it may easily be shown that  $k_j = 0$  for  $\text{N}_2$ .) The average molecular weight varies with composition and may be expressed as:

$$MW = \frac{44 P_{CO_2} + 28(P - P_{CO_2})}{P} \quad (6)$$

Substitution of this expression into Equation 5, integration of that equation and application of the boundary conditions that the various partial pressures at  $r \rightarrow \infty$  are equal to ambient values (0.0 in the case of CO) leads to:

$$P_{CO_2} = (P_{CO_2, Amb} + 1.75P)e^{-16 k_2/r} - 1.75 P \quad (7)$$

$$P_{CO} = 2.75P - P_{N_2, Amb} - (P_{CO_2, Amb} + 1.75 P)e^{-16 k_2/r} \quad (8)$$

$$P_{N_2} = P_{N_2, Amb} \quad (9)$$

for  $r > r_c$ , where  $k_2$  must be evaluated through boundary condition matching at  $r = r_c$ .

The energy conservation equation in the outer region ( $r > r_c$ ) may be written as:

$$\frac{1}{r} \frac{\partial}{\partial r} \left\{ r^2 \lambda \frac{\partial T}{\partial r} \right\} - \rho u C_p \frac{\partial T}{\partial r} = 0 \quad (10)$$

T = temperature

$\lambda$  = thermal conductivity

$C_p$  = specific heat

u = linear velocity relative to the particle surface

where the first term is a conduction term and the second term is a convection term. For integration of this equation it is necessary that an expression for the mass flux,  $\rho u$ , as a function of radius be substituted, with this expression preferably relating  $\rho u$  to the total mass flux of aluminum leaving the particle surface ( $\dot{m}_{p, TOT}$ ). Since all of the aluminum leaving the surface is assumed to disappear as  $Al_2O_3(l)$  into a single sink at  $r = r_c$ , it may easily be shown from a mass balance and stoichiometry considerations that the net mass flux,  $\rho u$ , at  $r = r_c^+$  is given by:

$$\begin{aligned} r_c^2 \rho u \Big|_{r = r_c^+} &= -\dot{m}_{p, TOT} r_p^2 \left( \frac{\text{Mass of oxygen per mole of } Al_2O_3}{\text{Mass of aluminum per mole of } Al_2O_3} \right) \\ &= -0.899 \dot{m}_{p, TOT} r_p^2 \end{aligned} \quad (11)$$

Then, since there are no other mass sinks, the mass flux at any other radius greater than  $r = r_c$  is related to that at  $r = r_c^+$  by the inverse square of the radius:

$$\rho u = [\rho u|_{r=r_c^+}] \frac{r_c^2}{r^2} = - \frac{0.889 \dot{m}_{p,TOT} r_p^2}{r^2} \quad (11a)$$

$\dot{m}_{p,TOT}$  = mass flux away from particle surface

$r_p$  = particle radius.

Thus, Equation 10 becomes:

$$\frac{1}{r^2} \frac{\partial}{\partial r} \left\{ r^2 \lambda \frac{\partial T}{\partial r} \right\} + \frac{0.889 \dot{m}_{p,TOT} r_p^2 C_p}{r^2} \frac{\partial T}{\partial r} = 0 \quad (12)$$

With the assumption that the thermal conductivity,  $\lambda$ , is independent of position (analogous to the earlier assumption that the density-diffusivity product is independent of position), this equation may be integrated to yield:

$$T = T_{amb} + \left( \frac{T_{r=r_c} - T_{amb}}{e^{0.889 \dot{m}_{p,TOT} r_p^2 C_p / \lambda r_c} - 1} \right) \left( e^{0.889 \dot{m}_{p,TOT} r_p^2 C_p / \lambda r} - 1 \right) \quad (13)$$

As mentioned earlier, it is assumed that the condensation radius,  $r = r_c$ , is a location at which all aluminum containing species arriving there react infinitely rapidly to form condensed  $Al_2O_3$ , any needed oxygen being supplied by  $CO_2$  diffusing and/or convecting in from the outer region. Thus, one may immediately write as part of the boundary conditions to be satisfied at  $r = r_c$ ,

$$P_{Al}|_{r=r_c^+} = 0 \quad (14)$$

$$P_{Al_2O}|_{r=r_c^+} = 0 \quad (15)$$

$$P_{AlO}|_{r=r_c^+} = 0 \quad (16)$$

In addition, applications of conservation equations for enthalpy, oxygen atoms, carbon atoms, and nitrogen atoms at  $r = r_c$  yield, when combined with equations 7 - 9 and 13:

$$D(MW) \left. \frac{(\partial P_{N_2}/MW)}{\partial r} \right|_{r=r_c^-} = \frac{\dot{m}_{p,TOT} r_p^2 RT_{r=r_c} P_{N_2,Amb}}{r_c^2 P(MW)} \quad (17)$$

$$D(MW) \left. \frac{(\partial P_{CO_2}/MW)}{\partial r} \right|_{r=r_c^-} = \frac{\dot{m}_{p,TOT} r_p^2 P_{CO_2} RT}{r_c^2 P(MW)}$$

$$\frac{D}{r_c} \left\{ \ln \left[ \frac{P_{CO_2} + 1.75P}{P_{CO_2,Amb} + 1.75P} \right] \right\} (P_{CO_2} + 1.75) +$$

$$D(MW) \left[ 1.5 \frac{\partial(P_{Al}/MW)}{\partial r} + 0.5 \frac{\partial(P_{AlO}/MW)}{\partial r} + 2.0 \frac{\partial(P_{Al_2O}/MW)}{\partial r} \right] \quad (18)$$

$$D(MW) \left. \frac{\partial(P_{CO}/MW)}{\partial r} \right|_{r=r_c^-} = \frac{\dot{m}_{p,TOT} r_p^2 RT_{r=r_c} (P - P_{N_2,Amb} - P_{CO_2})}{r_c^2 P(MW)} +$$

$$\frac{D}{r_c} \left\{ \ln \left[ \frac{P_{CO_2} + 1.75P}{P_{CO_2,Amb} + 1.75P} \right] \right\} (P_{CO_2} + 1.75P) -$$

$$D(MW) \left[ 1.5 \frac{\partial(P_{Al}/MW)}{\partial r} + 0.5 \frac{\partial(P_{AlO}/MW)}{\partial r} + 2.0 \frac{\partial(P_{Al_2O}/MW)}{\partial r} \right] \quad (19)$$

$$- 0.889 \dot{m}_{p,TOT} r_p^2 C_p (T_{r=r_c} - T_{amb}) e^{0.889 \dot{m}_{p,TOT} r_p^2 C_p / \lambda r_c}$$

$$\lambda \frac{\partial T}{\partial r} \Big|_{r=r_c^-} = \frac{\dot{m}_{p,TOT} r_p^2 C_p (T_{r=r_c} - T_{amb}) e^{0.889 \dot{m}_{p,TOT} r_p^2 C_p / \lambda r_c}}{r_c^2 (e^{0.889 \dot{m}_{p,TOT} r_p^2 C_p / \lambda r_c} - 1)} +$$

$$\frac{1.889 \dot{m}_{p,TOT} r_p^2 C_p T_{r=r_c}}{r_c^2} - \frac{D(MW)}{RT} \left[ Q_{10} \frac{\partial(P_{Al}/MW)}{\partial r} + \right.$$

$$\left. Q_{11} \frac{\partial(P_{AlO}/MW)}{\partial r} + Q_{12} \frac{\partial(P_{Al_2O}/MW)}{\partial r} \right]_{r=r_c^-} \quad (20)$$

where  $Q_{10}$  is the heat release associated with  $Al(g) + 3/2 CO_2 + 1/2 Al_2O_3(l) + 3/2 CO$ ,  $Q_{11}$  is the heat release associated with  $AlO + 1/2 CO_2 + 1/2 Al_2O_3(l) + 1/2 CO$ , and  $Q_{12}$  is the heat release associated with  $Al_2O(g) + 2CO_2 + Al_2O_3(l) + 2CO$ .

In the inner region between the particle radius ( $r = r_p$ ) and the condensation radius ( $r = r_c$ ), the species to be considered are (Figure III-2)  $N_2$ ,  $CO$ ,  $CO_2$ ,  $Al$ ,  $AlO$ , and  $Al_2O$ . Applying mass, enthalpy and species conservation equations, using the procedures of Williams,<sup>(20)</sup> we find:

$$\frac{1}{r^2} \frac{\partial}{\partial r} \left\{ r^2 \lambda \frac{\partial T}{\partial r} \right\} - \rho u C_p \frac{\partial T}{\partial r} + Q_1 R_1 = 0 \quad (21)$$

$$\frac{1}{r^2} \frac{\partial}{\partial r} \left\{ r^2 (\rho D) \frac{\partial (P_j / MW)}{\partial r} \right\} - \rho u \frac{\partial (P_j / MW)}{\partial r} - P R_1 v_j = 0 \quad (22a-f)$$

$$j = N_2, CO, CO_2, Al, AlO, Al_2O$$

$$\dot{m}_{p, TOT} r_p^2 = \rho u r^2 \quad (23)$$

where the  $v_j$ 's are the stoichiometric coefficients in the reaction  $Al(g) + CO_2 + AlO + CO$  ( $v_{N_2} = 0.0$ ,  $v_{Al} = 1.0$ ,  $v_{CO_2} = 1.0$ ,  $v_{AlO} = 1.0$ ,  $v_{CO} = -1.0$ ,  $v_{Al_2O} = 0.0$ ),  $R_1$  is the rate of the reaction (moles/volume/time), and  $Q_1$  is the heat release associated with the reaction. Substitution of Equation 23 into Equations 21 and 22 yields seven second-order differential equations to be solved over the inner region subject to boundary conditions at the condensation radius given above (Equations 14 - 20) and the boundary conditions at the particle surface which are discussed below.

$$\frac{1}{r^2} \frac{\partial}{\partial r} \left\{ r^2 \lambda \frac{\partial T}{\partial r} \right\} - \frac{\dot{m}_{p, TOT} r_p^2 C_p}{r^2} \frac{\partial T}{\partial r} + Q_1 R_1 = 0 \quad (24)$$

$$\frac{1}{r^2} \frac{\partial}{\partial r} \left\{ r^2 (\rho D) \frac{\partial (P_j / MW)}{\partial r} \right\} - \frac{\dot{m}_{p, TOT} r_p^2 C_p}{r^2} \frac{\partial (P_j / MW)}{\partial r} - P R_1 v_j = 0 \quad (25a-f)$$

As mentioned earlier, two slightly differing models were examined during the course of this program, with infinitely fast reaction of  $\text{CO}_2$  with liquid aluminum at the particle surface being allowed in the first and prohibited in the second. Let us first examine the inner boundary conditions for the case where  $\text{CO}_2$  is allowed to react at the surface. In this case, we can immediately write as two boundary conditions:

$$P_{\text{AlO}, r = r_p} = 0 \quad (26)$$

$$P_{\text{CO}_2, r = r_p} = 0 \quad (27)$$

In addition, conservation equations for the other four species permit derivation of four additional boundary conditions:

$$D(\text{MW}) \frac{\partial (P_{\text{N}_2} / \text{MW})}{\partial r} = \frac{\dot{m}_{\text{p, TOT}} \text{RT}_s}{P(\text{MW})} P_{\text{N}_2} \quad (28)$$

$$D(\text{MW}) \frac{\partial (P_{\text{CO}} / \text{MW})}{\partial r} = \frac{\dot{m}_{\text{p, TOT}} \text{RT}_s}{P(\text{MW})} P_{\text{CO}} - D(\text{MW}) \frac{\partial (P_{\text{CO}_2} / \text{MW})}{\partial r} \quad (29)$$

$$D(\text{MW}) \frac{\partial (P_{\text{Al}} / \text{MW})}{\partial r} = \frac{\dot{m}_{\text{p, TOT}} \text{RT}_s}{P(\text{MW})} P_{\text{Al}} - \frac{\dot{m}_{\text{evap}} \text{RT}_s}{27} \quad (30)$$

$$D(\text{MW}) \frac{\partial (P_{\text{Al}_2\text{O}} / \text{MW})}{\partial r} = \frac{\dot{m}_{\text{p, TOT}} \text{RT}_s}{P(\text{MW})} P_{\text{Al}_2\text{O}} - D(\text{MW}) \left\{ \frac{\partial (P_{\text{AlO}} / \text{MW})}{\partial r} + \frac{\partial (P_{\text{CO}_2} / \text{MW})}{\partial r} \right\}_{r = r_p} \quad (31)$$

A seventh boundary condition is obtained from an enthalpy balance at the particle surface as:

$$\frac{\dot{m}_{\text{evap}} L_{\text{evap}}}{27} = \lambda \frac{\partial T}{\partial r} + \frac{D(\text{MW})}{\text{RT}} \left[ Q_5 \frac{\partial (P_{\text{AlO}} / \text{MW})}{\partial r} + Q_7 \frac{\partial (P_{\text{CO}_2} / \text{MW})}{\partial r} \right]_{r = r_p} \quad (32)$$

where  $\dot{m}_{\text{evap}}$  is the evaporation mass flux of aluminum from the particle surface,  $L_{\text{evap}}$  is the heat of vaporization of aluminum and  $Q_5$  and  $Q_7$  are heat releases

associated with  $\text{Al}(\ell) + \text{AlO} \rightarrow \text{Al}_2\text{O}$  and  $2\text{Al}(\ell) + \text{CO}_2 \rightarrow \text{Al}_2\text{O} + \text{CO}$ , respectively. Since aluminum leaves the surface by both evaporative and reactive processes, one more equation relating the total mass flux to the evaporative flux is given by:

$$\dot{m}_{p,\text{TOT}} = \dot{m}_{\text{evap}} + \frac{27D(\text{MW})}{RT} \left[ \frac{\partial (P_{\text{Al}_2\text{O}}/\text{MW})}{\partial r} + 2 \frac{\partial (P_{\text{CO}_2}/\text{MW})}{\partial r} \right]_{r=r_p} \quad (33)$$

Finally, to close the problem, a rate expression using Fontijn's kinetic data (Equation 3) is substituted for  $R_1$  in Equations 24 and 25, and an expression relating the partial pressure of aluminum vapor at the particle surface to the surface temperature is employed. This latter expression was obtained by curve-fitting JANNAF thermodynamic data, yielding:

$$T_{r=r_p} = 34860 / (12.537 - \ln P_{\text{Al},r=r_p}) \quad (34)$$

In the second model, where  $\text{CO}_2$  is not allowed to react with aluminum liquid at the surface, the only changes in the particle surface (inner) boundary conditions are the substitution of:

$$D(\text{MW}) \frac{\partial (P_{\text{CO}_2}/\text{MW})}{\partial r} = \frac{\dot{m}_{p,\text{TOT}} RT_s}{P(\text{MW})} P_{\text{CO}_2} \quad (35)$$

for equation 27, and the elimination of the  $\partial (P_{\text{CO}_2}/\text{MW})/\partial r$  term in Equations 29, 31, 32, and 33.

The problem at this point is to find solutions to seven coupled non-linear second-order differential equations (24, 25a-f) which will satisfy the seven outer boundary condition relationships given by Equations 14 - 20 and the seven inner boundary conditions relationships and ancillary equations given by Equations 26 - 34 (or, for the second model, Equations 26, 28, 30, 34, 35, and modified versions of 29, 31, 32, and 33). In order to simplify this problem, two major approximations were made. First, the Lewis Numbers (ratio of thermal diffusivity to species diffusivity) were assumed to be unity for all species, permitting use of the Shvab-Zeldovich procedure to reduce the seven second-order differential equations to one second-order differential equation plus six algebraic equations relating the various species concentrations to one another and to temperature at any given position.

In addition, the thermal conductivity (and thus the density-diffusivity product) were assumed to be independent of position.

In the employment of the Shvab-Zeldovich procedure, the following new variables were defined:

$$P_1' = (P_{AlO} + P_{Al} + 2P_{Al_2O})/MW \quad (36)$$

$$P_2' = (P_{CO} + P_{CO_2})/MW \quad (37)$$

$$P_3' = (2P_{CO_2} + P_{CO} + P_{AlO} + P_{Al_2O})/MW \quad (38)$$

$$P_4' = P_{N_2}/MW \quad (39)$$

$$\psi_1 = T + (Q_I/P_{C_p}) (P_{CO_2}/MW) \quad (40)$$

$$\psi_2 = (P_{CO_2} - P_{Al})/MW \quad (41)$$

and substituted into Equations 24 and 24a-f to yield:

$$\frac{\partial}{\partial r} \left\{ r^2 \lambda \frac{\partial T}{\partial r} \right\} - \frac{\dot{m}_{p, TOT} r^2 C_p}{r^2} \frac{\partial T}{\partial r} + Q_1 R_1 r^2 = 0 \quad (42)$$

$$\frac{\partial}{\partial r} \left\{ r^2 \lambda \frac{\partial F_j}{\partial r} \right\} - \frac{\dot{m}_{p, TOT} r^2 C_p}{r^2} \frac{\partial F_j}{\partial r} = 0 \quad (43a-f)$$

$$F_j = P_1', P_2', P_3', P_4', \psi_1, \psi_2$$

where:

$$\begin{aligned} R_1 &= 4.70(10^{11}) T^{1/2} e^{-1500/T} C_{Al} C_{CO_2} \\ &= 6.98(10^7) P_{Al} P_{CO_2} e^{-1500/T} / T^{1.5} \end{aligned} \quad (44)$$

With the approximation that the thermal conductivity,  $\lambda$ , is independent of position, Equations 43a-f can then be integrated to yield the closed-form expressions:

$$P_1' = c_1 + d_1 e^{-K_1/\lambda r} \quad (45)$$

$$P_2' = c_2 + d_2 e^{-K_1/\lambda r} \quad (46)$$

$$P_3' = c_3 + d_3 e^{-K_1/\lambda r} \quad (47)$$

$$P_4' = c_4 + d_4 e^{-K_1/\lambda r} \quad (48)$$

$$\psi_1 = c_5 + d_5 e^{-K_1/\lambda r} \quad (49)$$

$$\psi_2 = c_6 + d_6 e^{-K_1/\lambda r} \quad (50)$$

where  $K_1 = \dot{m}_{p,TOT} r_p^2 C_p$  and  $c_j$  and  $d_j$  are constants of integration to be evaluated using the boundary condition equations.

Equations 36 - 41 are also substituted into the appropriate boundary condition equations to convert them into the new variables. Values for the condensation radius ( $r_c$ ) and the total mass flux at the particle surface ( $\dot{m}_{p,TOT}$ ) are then estimated for given ambient conditions and particle radius and the inner and outer boundary conditions, ancillary equations, and Equations 45 - 50 are solved simultaneously (a miserable algebra problem) to yield first-cut values for  $c_1$  thru  $c_6$ ,  $d_1$  thru  $d_6$ , temperature at the condensation radius, and temperature, composition and temperature gradient at the particle surface. Successive estimates are made on the condensation radius (at a fixed estimate of  $\dot{m}_{p,TOT}$ ) until the desired condensation radius temperature is calculated. At this point, the calculated surface temperature, composition and surface temperature gradient are used to start numerical integration of Equation 42 from the particle surface. Equations 40, 41, 49 and 50 are used to relate aluminum vapor and carbon dioxide partial pressures to temperature at each point to permit evaluation of  $R_1$  from Equation 44 at each step in the integration. Equation 42 is integrated from  $r = r_p$  to  $r = r_c$  where the calculated parameter values are tested to see whether they satisfy the outer boundary conditions. If not, a new value of  $\dot{m}_{p,TOT}$  is estimated, and the entire procedure (including searching for the condensation radius which yields the desired condensation temperature) is repeated.

Application of this procedure to the second model (in which the reaction of  $\text{CO}_2$  with aluminum liquid at the particle surface was prohibited) was relatively straightforward (discounting the horrendous algebra). However, when the  $\text{CO}_2$  surface reaction was permitted (with infinite kinetics) an interesting (and upon reflection, to be expected) result occurred; namely, the temperature gradient at the surface was calculated to be infinity (from a combination of Equations 32 and 33 with  $\dot{m}_{\text{evap}}$  eliminated) at all estimated values of  $\dot{m}_{\text{p,TOT}}$  except one, at which it was calculated to be indeterminate (zero over zero). Examination of the problem revealed that the value of  $\dot{m}_{\text{p,TOT}}$  which gave an indeterminate value of this gradient was the correct answer and was independent of the kinetics of the gas-phase  $\text{Al(g)} + \text{CO}_2 \rightarrow \text{AlO} + \text{CO}$  reaction. Reflection indicated that this was logical, given the assumptions made in this model. Since it was assumed that all  $\text{CO}_2$  reactant which reaches the surface without reacting with aluminum vapor reacts infinitely fast there to produce the same product as any  $\text{AlO}$  from the gas-phase reaction which reaches the surface (namely  $\text{Al}_2\text{O}$ ) and since it was furthermore assumed that all Lewis Numbers were unity, the total mass flow from the surface is naturally independent of the rate of the gas-phase reaction. While the details of the temperature and concentration profiles in the gas-phase depend on the gas-phase kinetics, the change in sensible enthalpy feedback from the gas-phase due to the gas-phase reaction is just offset by reactive oxidizer species gradient changes resulting from the gas-phase reaction. Thus, we arrive at the very interesting result that if we allow all products of any gas-phase reactions (including not only Reaction 1, but Reactions 2, 3, and 4 as listed earlier) and all unreacted oxidizer ( $\text{CO}_2$ ) to react infinitely fast at the surface to the same product (and if the Lewis Number = 1 assumption is reasonably good) the burning rate of an aluminum particle is independent of gas-phase kinetics as implicitly assumed in past models. If, however, oxidizer which does not react in the gas-phase cannot react at the surface while products (e.g.,  $\text{AlO}$ ) of gas-phase reactions can, the burning rate will depend on the gas-phase kinetics as shown by the results presented in the next section. As would be expected, if the gas-phase kinetic rates are assumed to be infinite, results of the second model collapse to those of the first.

Further discussion will be mainly limited to the second model, in which  $\text{CO}_2$  is prohibited from reacting with liquid aluminum at the surface. A computer program was written to solve the equations presented earlier using the procedure outlined above, giving predicted surface mass fluxes as a function of ambient conditions, particle size, and assumed condensation temperature. These surface mass fluxes were then straightforwardly converted to linear burning rates. Burning times for particles of various initial sizes were then calculated by integrating burning rate versus particle size predictions (for given ambient conditions and assumed condensation temperatures):

$$\tau_{\text{burn}} = \int_0^{r_{p,\text{initial}}} \frac{dr}{(\text{Linear Burning Rate})} \quad (51)$$

Results are presented and discussed in the next section.

#### D. Results

As indicated above, only results from the second model ( $\text{CO}_2$  surface reactions prohibited) will be discussed here, since the first model (infinitely fast reaction of  $\text{CO}_2$  with liquid aluminum at particle surface allowed) collapses to a diffusion-limited result, particle burning rate being independent of gas-phase kinetics. That is, no matter what rate expression is used in the first model for the  $\text{Al(g)} + \text{CO}_2 \rightarrow \text{AlO} + \text{CO}$  reaction, the predicted burning rate is the same as that which would be predicted with the second model using an infinite rate for that reaction.

Predicted temperature and species concentration profiles around a burning aluminum particle are presented for three typical cases in Figures III-3 through III-5. In all of these cases, the temperature at the condensation radius was chosen to be  $3500^\circ\text{K}$ . (As mentioned earlier, we specify the temperature at the condensation shell and then solve for its location.) Since the condensation shell is postulated to be an infinitesimally thin region in which considerable reaction occurs, there are, as would be expected, discontinuities in the temperature derivative and the  $\text{CO}$  and  $\text{CO}_2$  partial pressure derivatives at this radius. For the case depicted in Figure III-3

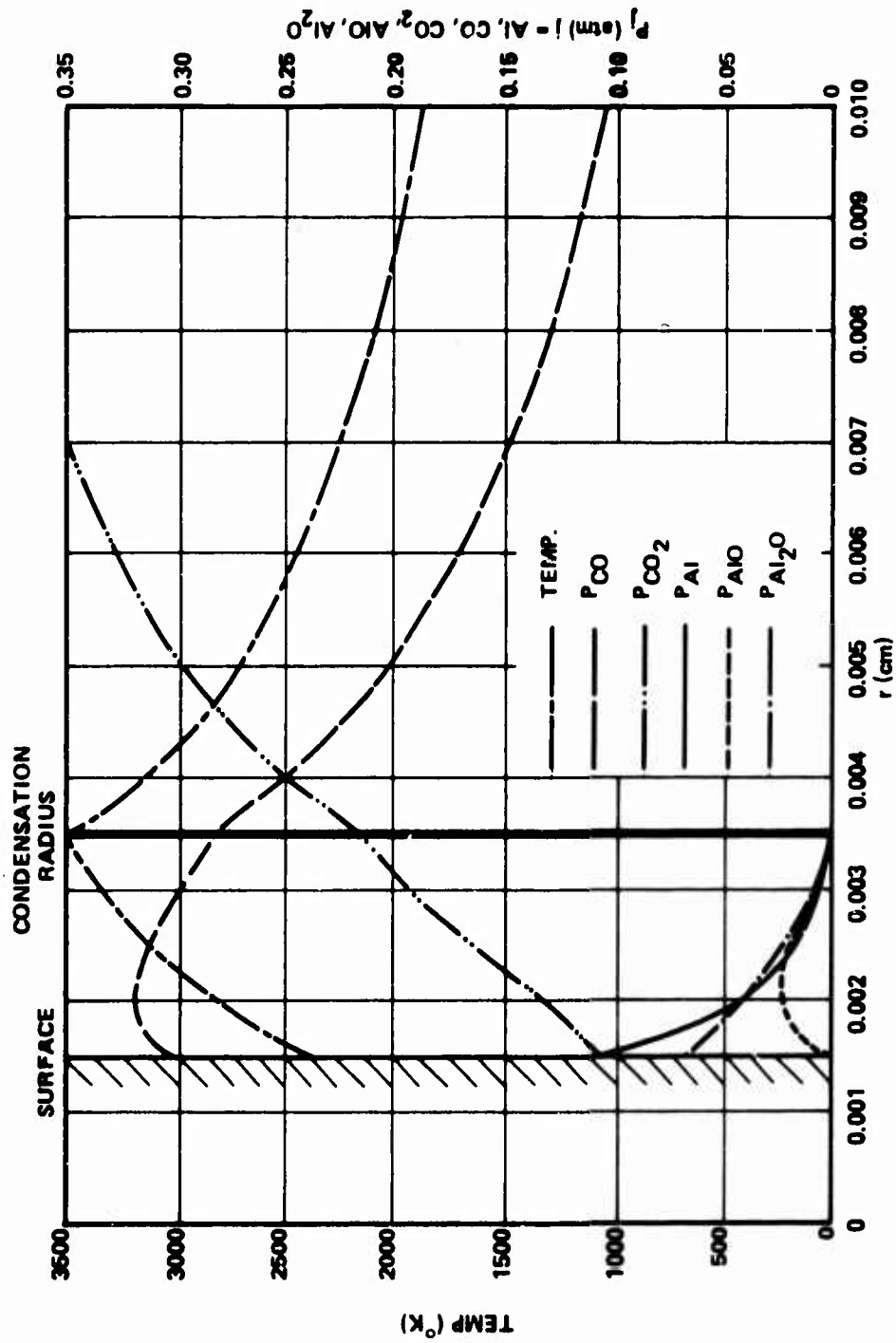


Figure III-3. Predicted Temperature and Concentration Profiles Around Burning Aluminum Particle.  
 Case 13,  $r_p = 15\mu$ ,  $T_{AMB} = 1000^\circ\text{K}$ ,  $P = 1$  atm,  $Y_{CO_2, AMB} = 0.5$ ,  $T_{rc} = 3500$ ,  $\dot{m}/\dot{m}_{\infty} = 0.74$ .

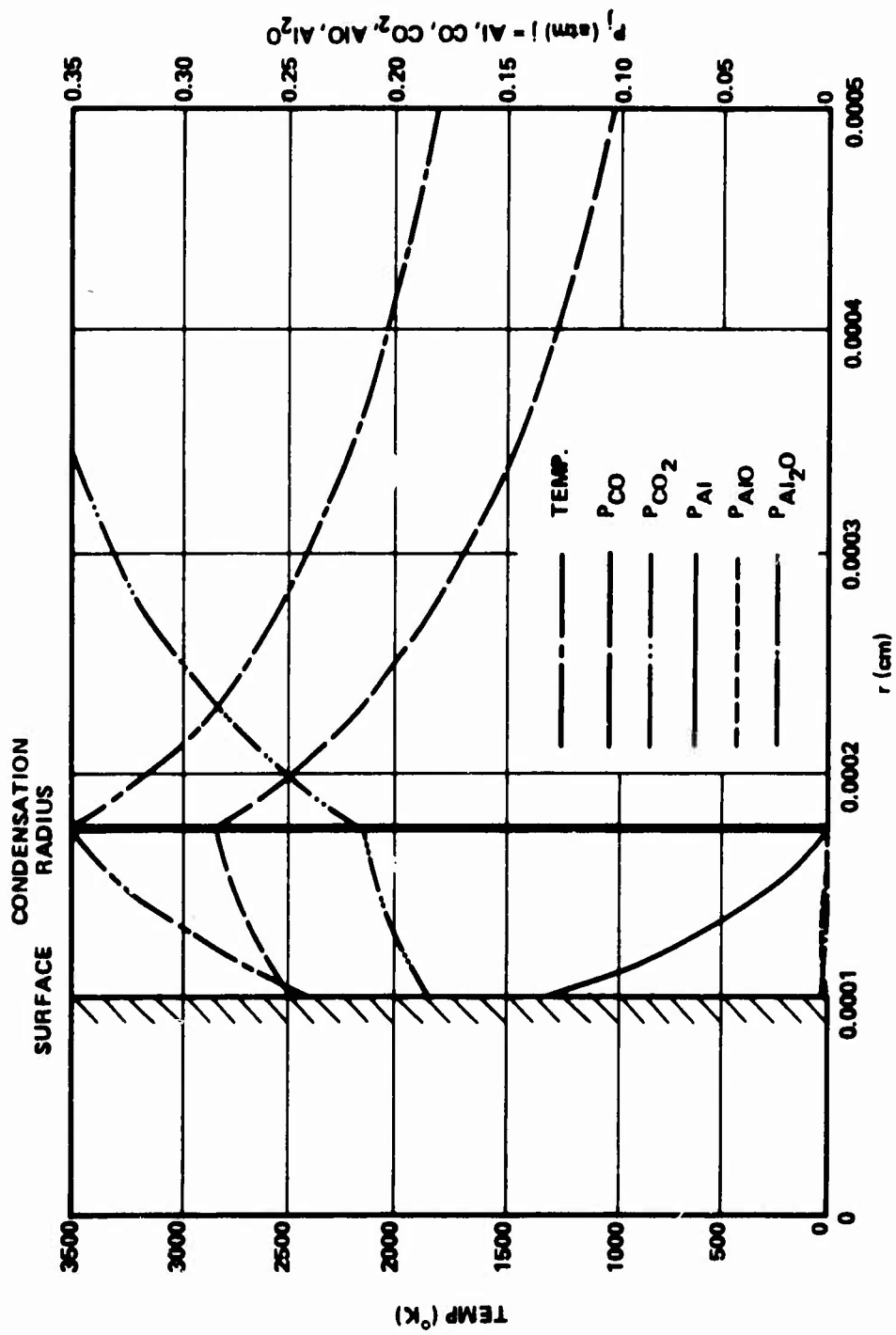


Figure III-4. Predicted Temperature and Concentration Profiles Around Burning Aluminum Particle.  
 Case 17,  $r_p = 1\mu$ ,  $T_{AMB} = 1000^\circ K$ ,  $P = 1$  atm,  $Y_{CO_2,AMB} = 0.5$ ,  $T_{rc} = 3500$ ,  $\dot{m}/\dot{m}_\infty = 0.53$ .

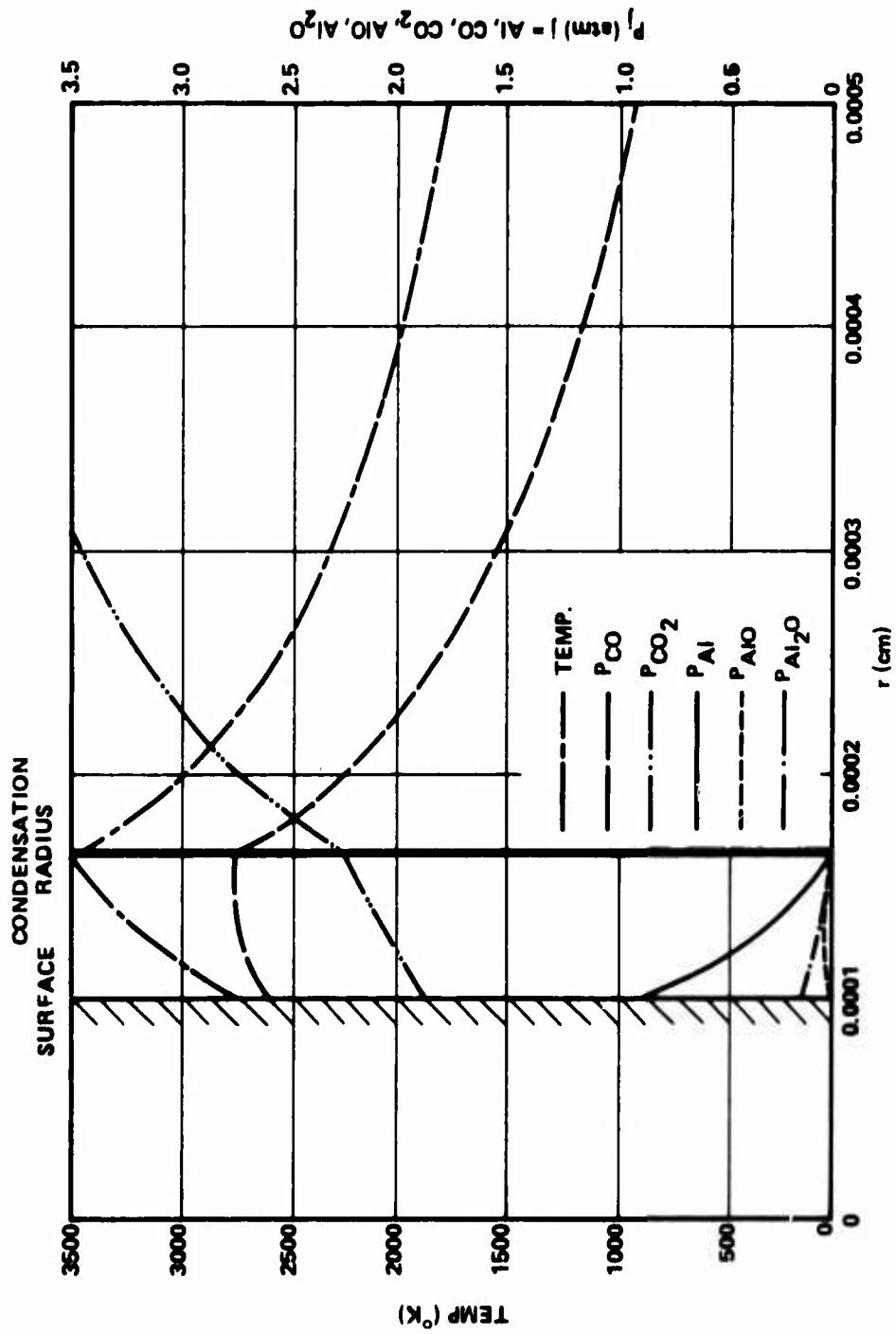


Figure III-5. Predicted Temperature and Concentration Profiles Around Burning Aluminum Particle.  
 Case 30,  $r_p = 1\mu$ ,  $T_{AMB} = 1000^\circ K$ ,  $P = 10$  atm,  $Y_{CO_2 AMB} = 0.5$ ,  $T_{rc} = 3500$ ,  $\dot{m}/\dot{m}_\infty = 0.52$ .

(Particle radius = 15 microns, ambient temperature = 1000°K, pressure = 1 atmosphere, ambient CO<sub>2</sub> mole fraction = 0.5), the diffusion processes are slow enough relative to the kinetics of the Al-CO<sub>2</sub> gas reaction that this reaction occurs to an appreciable extent as may be seen from the AlO and Al<sub>2</sub>O partial pressure curves. (Under the assumptions of this model, Al<sub>2</sub>O can be generated at the surface only if AlO is produced by the initial Al-CO<sub>2</sub> gas reaction, since AlO is the only species permitted to react at the surface to form Al<sub>2</sub>O.) For this particular case, the burning rate of the aluminum particle is predicted to be 74% of what it would be if the Fontijn kinetics were replaced with an infinite rate constant ( $\dot{m}_{\text{Fontijn}} / \dot{m}_{\text{infinite kin}} = 0.74$ ). The fact that the Al-CO<sub>2</sub> gas reaction occurs to an appreciable extent in this case is also shown in the CO partial pressure profile, which shows a peak value between the particle radius and the condensation shell due to its production by the Al-CO<sub>2</sub> gas reaction in this inner zone.

In contrast, Figures III-4 and III-5 depict predicted profiles for cases in which the amount of Al-CO<sub>2</sub> gas-phase reaction is very small. In both these cases, the particle radius is considerably smaller (1 micron) than that of the Figure III-3 case, leading to a much higher ratio of characteristic reaction time to diffusion time (lower value of the Damkohler Number). As may be seen, considerably less AlO and Al<sub>2</sub>O are produced in these cases, with the evaporation of aluminum thus basically being driven by heat feedback from the condensation zone, most of this heat being produced by the heterogeneous reaction of Al(g) and CO<sub>2</sub> at particle sites in this thin zone to Al<sub>2</sub>O<sub>3</sub>(l). In these cases, the CO concentration peaks at the condensation radius rather than in the region between the particle surface and the condensation radius. In addition, the ratio of predicted burning rate to that which would be predicted with infinite kinetics for the Al-CO<sub>2</sub> gas-phase reaction drops to approximately 0.5.

Burning rate predictions have been carried out using the model described above with Fontijn's reaction rate data for the Al(g) + CO<sub>2</sub> → AlO + CO reaction for a number of cases covering a wide range of particle sizes and ambient conditions. Results of these calculations are summarized in Table III-III and Figures III-6 and III-7. In Table III-III, the independent variables tabulated in Columns 2 to 5 are particle radius, ambient

TABLE III-III. Predicted Burning Rates of Aluminum Particles of Various Sizes Burning in Various CO<sub>2</sub>-N<sub>2</sub> Environments

Case Number	Particle Radius (microns)	Ambient Temperature (°K)	Pressure (atm)	CO <sub>2</sub> Partial Pressure (atm)	m(gm/cm <sup>2</sup> sec) With Infinite Kinetics, Temp At Condensation Radius = 3000 - 3500 °K	Condensation Radius Temperature = 3500°K			Condensation Radius Temperature = 3000°K				
						m/m <sub>∞</sub> (cm/sec)	Burn Rate (cm/sec)	Condensation Radius (μ)	m/m <sub>∞</sub> (cm/sec)	Burn Rate (cm/sec)	Condensation Radius (μ)		
1	10	1000	1	0.5	0.363	0.236	0.65	0.087	20.9	0.178	0.45	0.066	19.4
2	5	1000	1	0.5	0.726	0.404	0.56	0.150	8.9	0.299	0.41	0.111	8.1
3	20	1000	1	0.5	0.182	0.146	0.80	0.054	51.5	0.118	0.85	0.094	51.0
4	10	300	1	0.5	0.326	0.241	0.74	0.089	16.2	0.188	0.58	0.070	16.7
5	10	2000	1	0.5	0.404	0.246	0.61	0.091	37.2	0.183	0.45	0.068	41.0
6	10	3000	1	0.5	0.435	0.247	0.57	0.092	116.0	Can't have Tamb > Trc		0.094	27.6
7	10	1000	5	2.5	0.354	0.317	0.90	0.117	28.3	0.254	0.72	0.101	29.6
8	10	1000	10	5.0	0.349	0.330	0.95	0.122	29.6	0.272	0.78	0.101	29.6
9	10	1000	1	0.2	Insufficient Energy to Reach 3000°K								
10	10	1000	1	0.8	0.057	0.285	0.56	0.106	25.2	0.213	0.42	0.079	23.0
11	10	1000	10	2.0	0.497								
12	10	1000	10	8.0	0.414	0.414	0.83	0.153	36.8	0.314	0.63	0.116	34.1
13	15	1000	1	0.5	0.241	0.179	0.74	0.066	35.4	0.161	0.59	0.052	34.1
14	25	1000	1	0.5	0.145	0.123	0.85	0.046	67.9	0.100	0.69	0.037	67.5
15	30	1000	1	0.5	0.121	0.1065	0.88	0.039	83.9	0.088	0.73	0.033	85.0
16	3	1000	1	0.5	1.208	0.862	0.55	0.245	5.3	0.482	0.40	0.179	4.7
17	1	1000	1	0.5	3.619	1.934	0.33	0.716	1.71	1.41	0.39	0.522	1.33
18	20	300	1	0.5	0.162	0.135	0.83	0.050	36.6	0.112	0.69	0.042	34.9
19	30	300	1	0.5	0.108	0.0985	0.91	0.036	59.6	0.085	0.79	0.031	60.0
20	5	300	1	0.5	0.648	0.462	0.71	0.171	7.81	0.362	0.56	0.134	7.13
21	3	300	1	0.5	1.080	0.770	0.71	0.285	4.88	0.596	0.55	0.221	4.21
22	1	300	1	0.5	3.245	2.288	0.705	0.847	1.55	1.771	0.55	0.656	1.39
23	5	2000	1	0.5	0.808	0.378	0.47	0.140	14.2	0.255	0.32	0.094	14.3
24	20	2000	1	0.5	0.202	0.151	0.74	0.056	92.0	0.115	0.57	0.043	103.0
25	5	3000	1	0.5	0.874	0.382	0.44	0.141	45.0	Can't have Tamb > Tpeak = Trc			
26	20	3000	1	0.5	0.151	0.1218	0.69	0.056	282.0	Can't have Tamb > Tpeak = Trc			
27	20	1000	10	5.0	0.175	0.172	0.98	0.064	61.5	0.154	0.86	0.057	67.0
28	5	1000	10	5.0	0.703	0.604	0.85	0.223	13.5	0.460	0.65	0.170	12.7
29	3	1000	10	5.0	1.164	0.895	0.77	0.331	7.2	0.64	0.58	0.237	6.3
30	1	1000	10	5.0	3.505	1.83	0.52	0.678	1.65	1.23	0.35	0.456	1.37
31	30	1000	1	0.8	0.168	0.127	0.77	0.048	102.0	0.103	0.61	0.038	98.0
32	20	1000	1	0.8	0.252	0.177	0.70	0.066	82.0	0.136	0.45	0.050	58.0
33	5	1000	1	0.8	1.007	0.46	0.44	0.163	9.7	0.320	0.32	0.119	8.7
34	3	1000	1	0.8	1.678	0.668	0.40	0.247	5.33	0.488	0.29	0.181	4.77
35	1	1000	1	0.8	5.036	1.928	0.38	0.714	1.71	1.42	0.28	0.526	1.34
36	30	1000	1	0.65	0.148	0.121	0.82	0.448	96.0	0.097	0.66	0.036	94.0
37	20	1000	1	0.65	0.221	0.164	0.74	0.061	58.0	0.129	0.58	0.048	55.5
38	10	1000	1	0.65	0.442	0.264	0.60	0.098	23.3	0.197	0.45	0.073	21.3
39	5	1000	1	0.65	0.885	0.423	0.48	0.157	9.35	0.31	0.35	0.115	8.4
40	3	1000	1	0.65	1.474	0.665	0.45	0.246	5.30	0.490	0.33	0.181	4.8
41	1	1000	1	0.65	4.423	1.94	0.44	0.719	1.72	1.43	0.32	0.531	1.34
42	30	1000	1	0.35	0.127	0.0805	0.95	0.030	64.2	0.070	0.82	0.026	68.7
43	20	1000	1	0.35	0.114	0.114	0.90	0.042	40.3	0.096	0.76	0.036	41.5
44	10	1000	1	0.35	0.234	0.203	0.80	0.075	18.2	0.156	0.61	0.058	16.9
45	3	1000	1	0.35	0.508	0.391	0.77	0.145	8.65	0.290	0.57	0.107	7.90
46	3	1000	1	0.35	0.847	0.647	0.76	0.240	5.15	0.477	0.56	0.177	4.66
47	1	1000	1	0.35	2.540	1.944	0.765	0.720	1.72	1.42	0.56	0.526	1.36
48	20	1000	5	0.5	0.177	0.171	0.965	0.0633	60.8	0.148	0.836	0.0348	64.2
49	5	1000	5	0.5	0.708	0.544	0.748	0.201	12.2	0.407	0.575	0.151	11.1
50	3	1000	5	0.5	1.100	0.758	0.642	0.281	6.11	0.532	0.451	0.197	5.25
51	1	1000	5	0.5	3.540	1.80	0.508	0.666	1.61	1.282	0.362	0.474	1.41

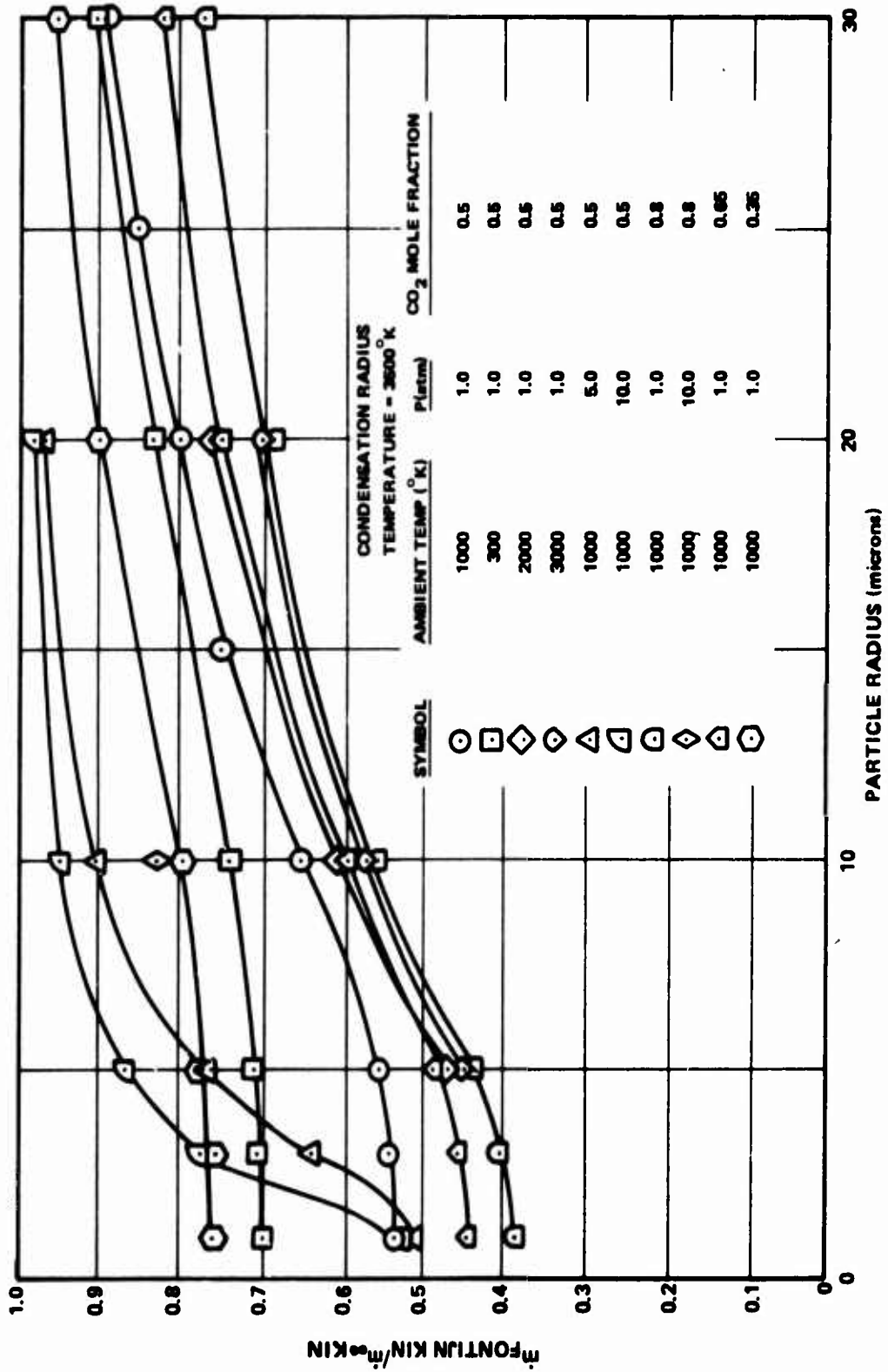


Figure III-6. Predicted Ratio of Burning Rate with Fontijn Kinetics to That with Infinite Kinetics.

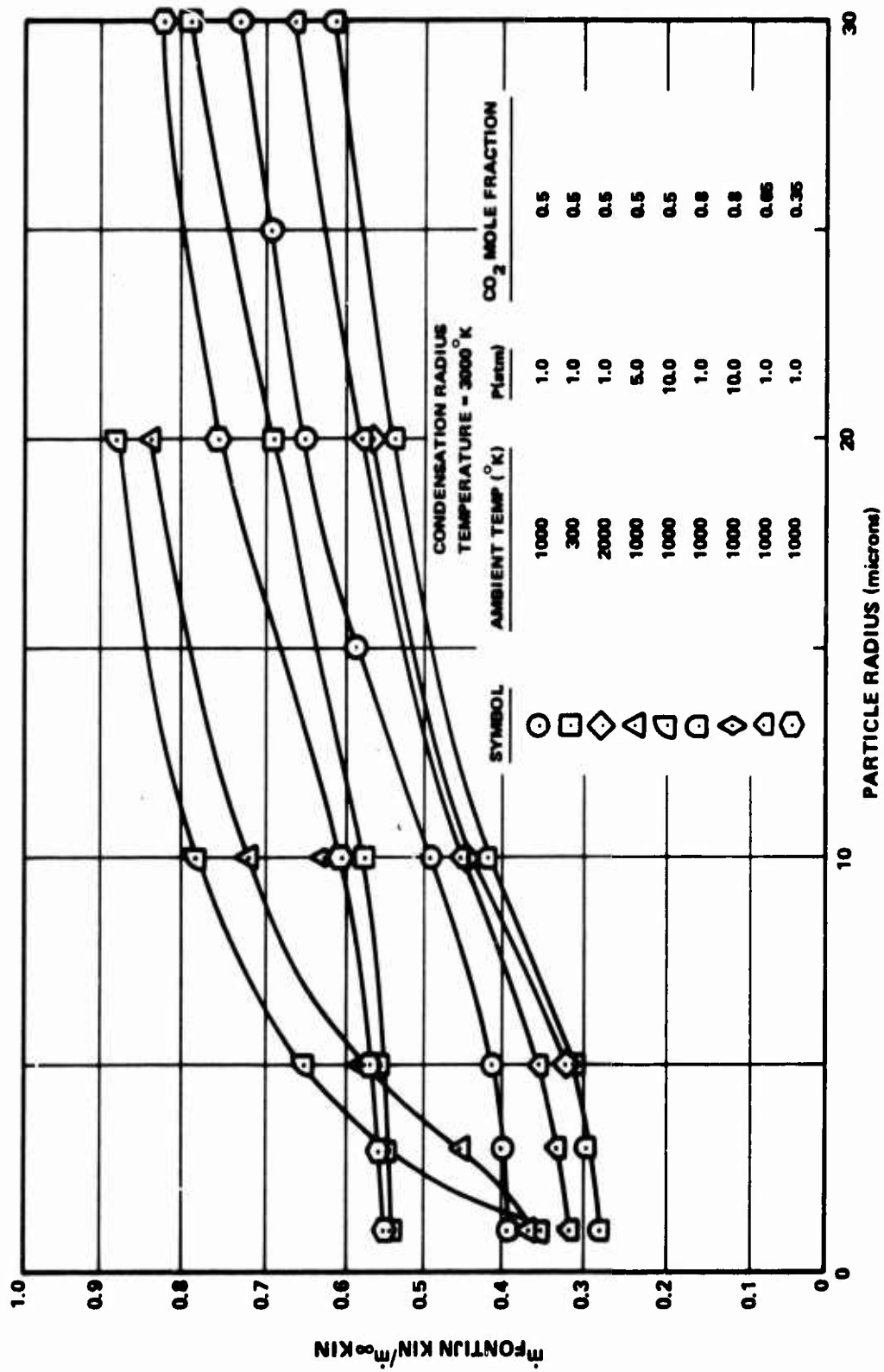


Figure III-7. Predicted Ratio of Burning Rate with Fontijn Kinetics to That with Infinite Kinetics.

temperature, pressure, and  $\text{CO}_2$  ambient partial pressure (with the remaining ambient gas being nitrogen). Two values of condensation radius temperature,  $3000^\circ\text{K}$  and  $3500^\circ\text{K}$ , were studied. The predicted mass burning rate (mass per unit area per time) was found to be very nearly independent of this temperature over this range for the case of infinite kinetics for the  $\text{Al}(\text{g}) + \text{CO}_2 \rightarrow \text{AlO} + \text{CO}$  reaction (or for the case where  $\text{CO}_2$  is allowed to react infinitely rapidly with liquid aluminum at the particle surface, as discussed earlier). This predicted mass burning rate for infinite kinetics is presented in Column 6. With finite kinetics (and  $\text{CO}_2$  reaction with liquid aluminum prohibited), however, the predicted burning rate was found to depend on condensation radius temperature, decreasing with decreased temperature (logically enough). In columns 7 through 10, the mass burning rate, ratio of that burning rate to the infinite-kinetics rate, linear burning rate, and condensation radius location, are tabulated for the  $3500^\circ\text{K}$  condensation temperature case, while the same outputs for the  $3000^\circ\text{K}$  case are presented in columns 11 through 14. As may be seen, the condensation shell location is not particularly dependent on the condensation temperature. (If the burning rates were the same, the condensation shell location would be further out for the lower temperature case, but as it turns out the decrease in burning rate associated with the decreased condensation temperatures results in a shift of the condensation shell back inwards.) In some cases, the condensation shell radius is slightly less for the  $3000^\circ\text{K}$  condensation temperature; in other cases it is slightly greater.

In Figures III-6 and III-7, the ratio of burning rate predicted using Fontijn kinetics to that predicted using infinite kinetics for the aluminum vapor reaction with  $\text{CO}_2$  is plotted against particle radius for various sets of ambient conditions (temperature, pressure,  $\text{CO}_2$  mole fraction). The ratios in Figure III-6 are calculated for a condensation shell temperature of  $3500^\circ\text{K}$ , while those in Figure III-7 are for  $3000^\circ\text{K}$ . As may be seen, the ratios (and thus the absolute rates, since the infinite-kinetics burning rate is essentially independent of condensation shell temperature over this range) are lower for the  $3000^\circ\text{K}$  case. As particle radius becomes larger, diffusion becomes slower relative to kinetics, and the burning rate ratio accordingly approaches unity at very large particle radii. Logically enough, since the

aluminum vapor reaction with  $\text{CO}_2$  is second order with respect to pressure, this approach of the burning rate ratio to unity occurs at lower values of particle radius for higher pressures. (Compare the 1, 5 and 10 atmosphere curves for  $T_{\text{ambient}} = 1000^\circ\text{K}$ ,  $Y_{\text{CO}_2, \text{ambient}} = 0.5$ .) At very small values of particle radius, on the other hand, where the characteristic diffusion times are small compared to the characteristic reaction times, one might expect the ratio of burning rate calculated using Fontijn kinetics to that calculated using infinite kinetics to drop to very low (approaching zero as particle radius approaches zero) values. This does not occur, however, since as the rate of the gas-phase reaction drops well below the diffusion rate, the location of the condensation zone begins to dominate the burning rate. (That is, the heat feedback from the condensation zone begins to dominate the rate of removal of aluminum from the particle surface, with removal by the  $\text{AlO}(\text{g}) + \text{Al}(\text{l}) \rightarrow \text{Al}_2\text{O}(\text{g})$  reaction becoming comparatively small.) Examination of Table III-III reveals that as particle radius becomes very small (less than about 5 microns for the 1 atmosphere cases) the ratio of condensation radius to particle radius, which, in general, decreases with decreasing particle radius, approaches a constant value (as is the case for all particle radii for infinite kinetics): as a result, the ratio of burning rate calculated using Fontijn kinetics to that calculated using infinite kinetics asymptotically approaches a constant value at small particle sizes, the magnitude of this value depending on ambient conditions. For the 1 atmosphere cases studied, this asymptotic value is approached at particle radii of 5 to 10 microns (depending on ambient conditions, while for the 5 atmosphere case it appears that it is being approached at about a 1 to 2 micron radius, and for the 10 atmosphere case, it may not be approached until particle radius is less than 1 micron. The burning ratio (Fontijn kinetics/infinite kinetics) is seen to decrease with increasing ambient temperature or increasing ambient  $\text{CO}_2$  mole fraction. Examination of Table III-III reveals that most of the variation of the burning rate ratio with ambient temperature is due to increase in the infinite-kinetics burning rate with ambient temperature, with the Fontijn-kinetics burning rate decreasing with increasing temperature for small particles (5 micron radius) and slightly increasing with increasing temperature for large particles

(20 micron radius). With respect to the calculated dependence of burning rate ratio on ambient CO<sub>2</sub> mole fraction, this is due to the dependence on this parameter of the burning rate calculated from Fontijn kinetics being somewhat less than that calculated using infinite kinetics, both calculated rates increasing with increasing ambient CO<sub>2</sub> mole fraction. The dependence of the burning rate calculated using Fontijn kinetics on this parameter decreases with decreasing particle radius.

One of the more critical assumptions made in development of this aluminum particle burning model was the assumption (based partly on thermodynamic equilibrium calculations at estimated particle surface temperatures) that aluminum oxide condensation at the particle surface could be neglected. With the outputs of the final model (notably aluminum vapor concentration and Al<sub>2</sub>O concentration adjacent to the surface and surface temperature) this assumption can be checked, at least in terms of thermodynamic equilibrium considerations, more rigorously. Such calculations have been performed, with the predicted Al<sub>2</sub>O partial pressure at the surface being compared to the saturation Al<sub>2</sub>O partial pressure as calculated from the equilibrium constant for  $3\text{Al}_2\text{O}(\text{g}) \rightleftharpoons \text{Al}_2\text{O}_3(\text{l}) + 4\text{Al}(\text{l})$  at the surface temperature. Results of calculations performed for the cases where the condensation shell temperature was set at 3500°K are presented in Table III-IV. Similar calculations were also performed for the cases where the condensation shell temperature was set at 3000°K. With the 3500°K cases, thermodynamically predicted surface condensation of Al<sub>2</sub>O<sub>3</sub> was only encountered for the high pressure-high CO<sub>2</sub> concentration (P = 10 atm, Y<sub>CO<sub>2</sub></sub> = 0.8) Case Number 12, while it was marginal for large particles for the high ambient temperature and high pressure intermediate CO<sub>2</sub> concentration cases. With 3000°K as the condensation shell temperature, potential surface condensation problems extended to more of the high pressure cases, being predicted for the larger particle sizes but not for the smaller, while the largest particle sizes (30 micron radius) gave problems for high CO<sub>2</sub> mole fractions even at 1 atmosphere. The trend that larger particles are indicated to be most likely to have oxide condensation on the surface is quite interesting in that, as discussed earlier, Prentice<sup>(19)</sup> observed that the amount of initial aluminum

TABLE III-IV. Thermodynamic Evaluation of the Assumption of No  $\text{Al}_2\text{O}_3(\ell)$  Condensation on the Burning Aluminum Particle Surface

Case No.	$T_{\text{surface}} (^{\circ}\text{K})$	$P^*_{\text{Al}_2\text{O surface}} (\text{atm})$	$P^*_{\text{Al}_2\text{O saturation}} (\text{atm})$
1	2389	0.0469	0.40
2	2408	0.0096	0.46
3	2357	0.1020	0.32
4	2300	0.0129	0.44
5	2365	0.1097	0.34
6	2345	0.1647	0.30
7	2559	0.697	1.20
8	2641	1.571	1.90
10	2368	0.101	0.35
12	2551	2.330	1.18
13	2372	0.078	0.36
14	2348	0.117	0.30
15	2342	0.126	0.29
16	2409	0.0074	0.46
17	2412	0.0011	0.48
18	2383	0.044	0.39
19	2370	0.067	0.36
20	2404	0.003	0.46
21	2404	0.002	0.46
22	2405	0.001	0.46
23	2400	0.048	0.44
24	2330	0.162	0.27
25	2381	0.106	0.39
26	2303	0.216	0.22
27	2626	1.695	1.72
28	2668	1.330	2.20
29	2699	1.035	2.65
30	2769	0.202	0.38
31	2302	0.194	0.22
32	2325	0.165	0.26
33	2408	0.029	0.47
34	2416	0.010	0.50
35	2420	0.0013	0.51
26	2317	0.169	0.24
37	2339	0.139	0.29
38	2378	0.076	0.38
39	2407	0.021	0.46
40	2413	0.008	0.48
41	2415	0.003	0.49
42	2381	0.050	0.39
43	2389	0.035	0.40
44	2401	0.013	0.44
45	2406	0.003	0.46
46	2406	0.0004	0.46
47	2406	0.007	0.46

\*Based on equilibrium calculations for  $3\text{Al}_2\text{O}(\text{g}) \rightleftharpoons \text{Al}_2\text{O}_3(\ell) + 4\text{Al}(\ell)$  at  $T = T_{\text{surface}}$ .

appearing in the final residue globule after burning decreased with decreasing particle size and, in fact, extrapolation of his data indicates that for sufficiently small particle sizes, no such oxide residue globule will occur.

The predicted burning rates as functions of particle radius presented in Table III-III and Figures III-6 and III-7 for various sets of ambient conditions were plugged into Equation 51 for graphical integration to yield predicted burn times as functions of initial particle radius. Results of these calculations are presented in Figures III-8 through III-13. In each figure (representing one set of ambient conditions, as labeled) predicted burn-time is plotted on log-log coordinates against initial particle radius. Lines representing three sets of assumptions are plotted on each figure: (1) infinite kinetics for the Al-CO<sub>2</sub> gas-phase reaction; (2) Fontijn kinetics, condensation shell temperature = 3500°K; and (3) Fontijn kinetics, condensation shell temperature = 3000°K. The average slope of each line, representing the exponent in the  $d_0^n - d^n = kt$  burning time power law is included on these figures. While the predicted exponent for the infinite-kinetics case is 2.0 (classic diffusion-limited  $d^2$  law) the exponents for the Fontijn kinetics cases are somewhat lower, ranging from approximately 1.35 to 1.85 for the 3000°K condensation temperature cases and from 1.4 to 1.9 for the 3500°K condensation cases. The predicted burn times for the 3500°K cases are anywhere from 10 to 120 percent greater than for the infinite-kinetics cases (the largest differences occurring for the smallest particles) while those for the 3000°K cases are from 30 to 200 percent greater than for the infinite-kinetics cases. As would be expected, the high pressure (10 atm) cases exhibit less difference between burn-time predictions with infinite and finite rate kinetics than the low pressure (1 atm) cases.

In Figures III-14 and III-15, predicted burn-times are cross-plotted against ambient CO<sub>2</sub> mole fraction for small (5μ radius) and large (30μ radius) particles for each of the three sets of assumptions listed above. As may be seen, for the small particles use of the finite-rate kinetics of Fontijn considerably reduces the predicted dependency of burn-time on CO<sub>2</sub> mole fraction for small particles, but does not appreciably affect this dependence for large particles where the burning is more nearly diffusion-limited.

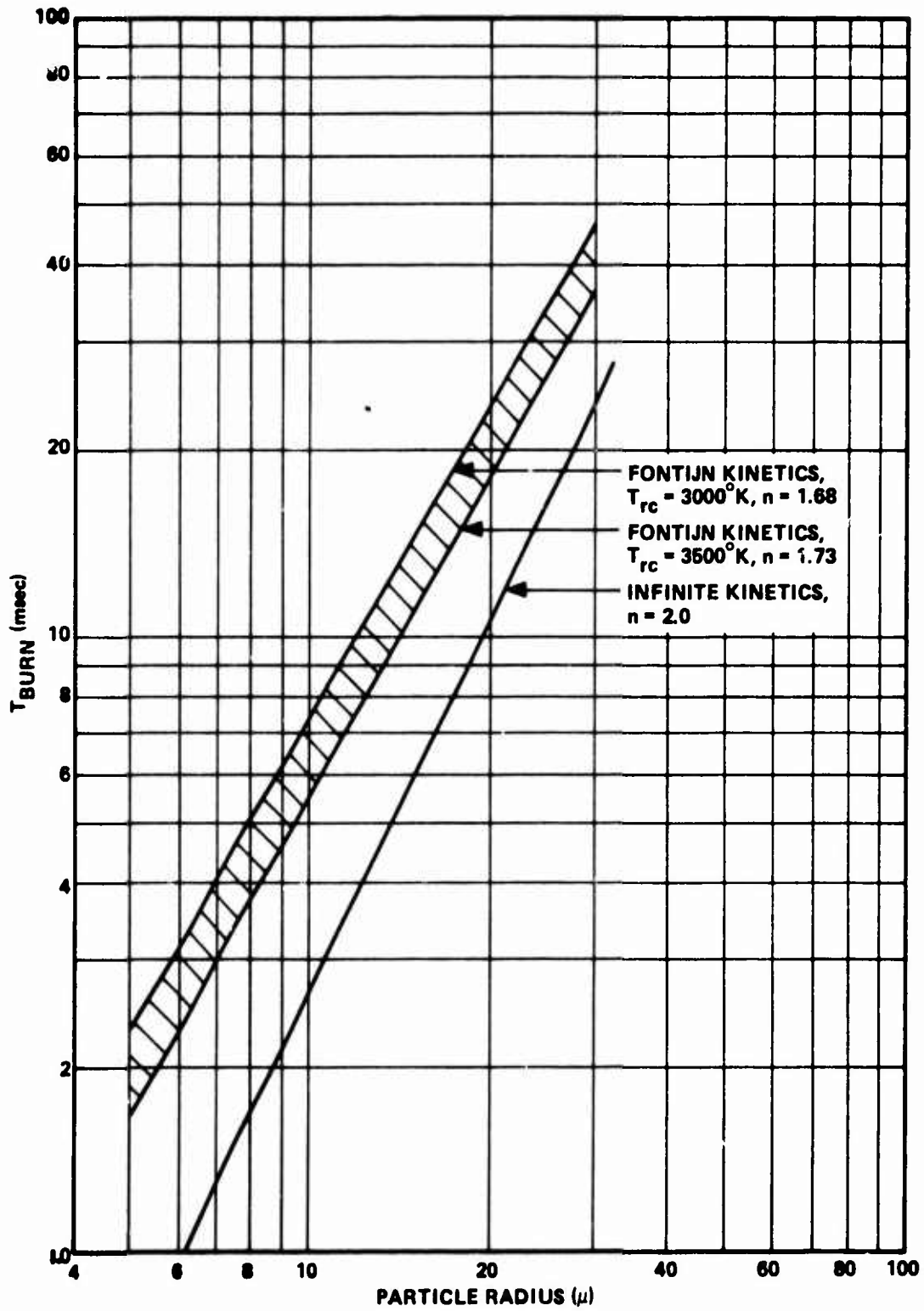


Figure III-8. Burn-Time Versus Particle Radius,  $T_{AMB} = 1000^{\circ}\text{K}$ ,  $P = 1 \text{ atm}$ ,  $Y_{\text{CO}_2} = 0.8$ .

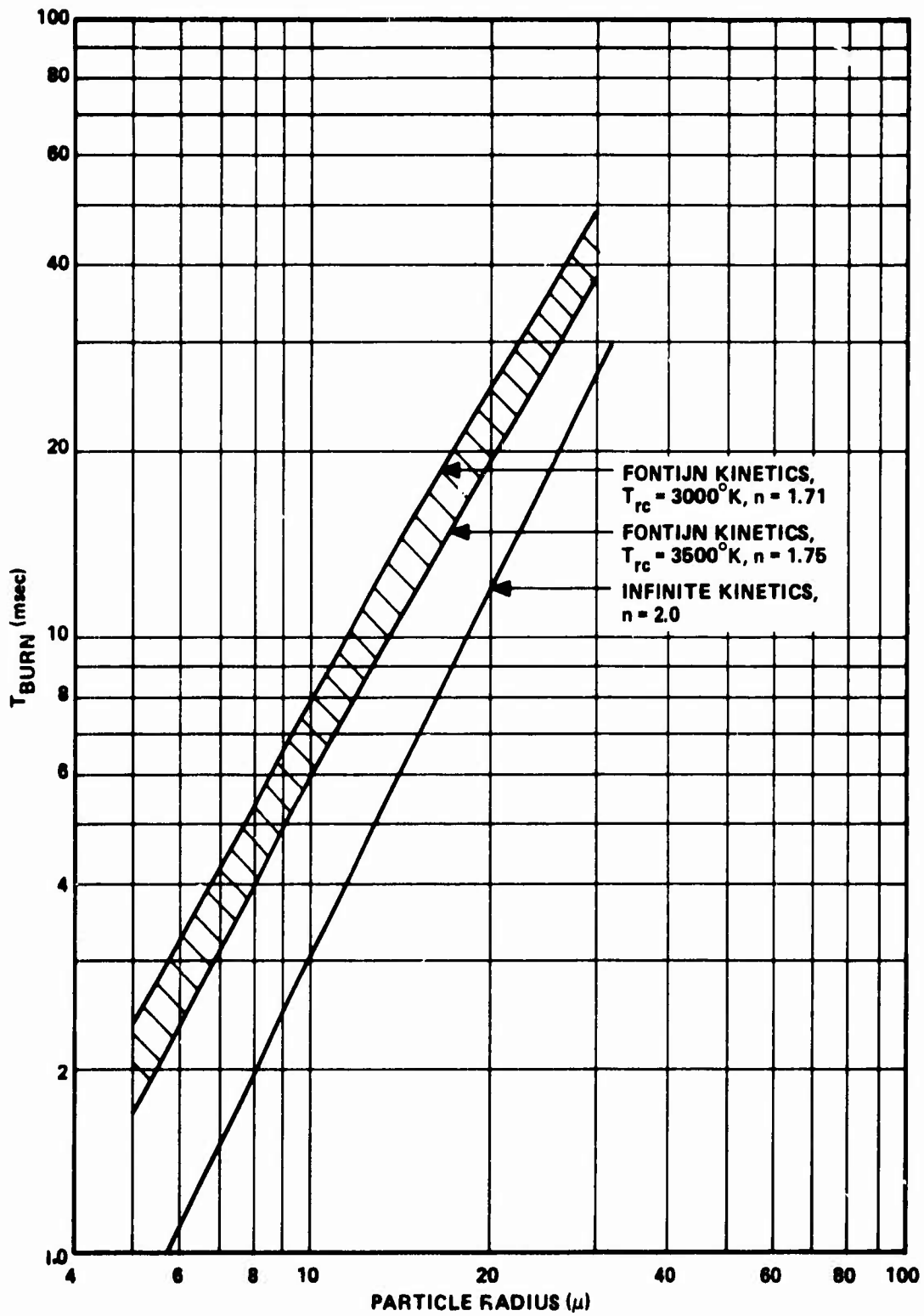


Figure III-9. Burn-Time Versus Particle Radius,  $T_{AMB} = 1000^{\circ}\text{K}$ ,  $P = 1 \text{ atm}$ ,  $Y_{CO_2} = 0.65$ .

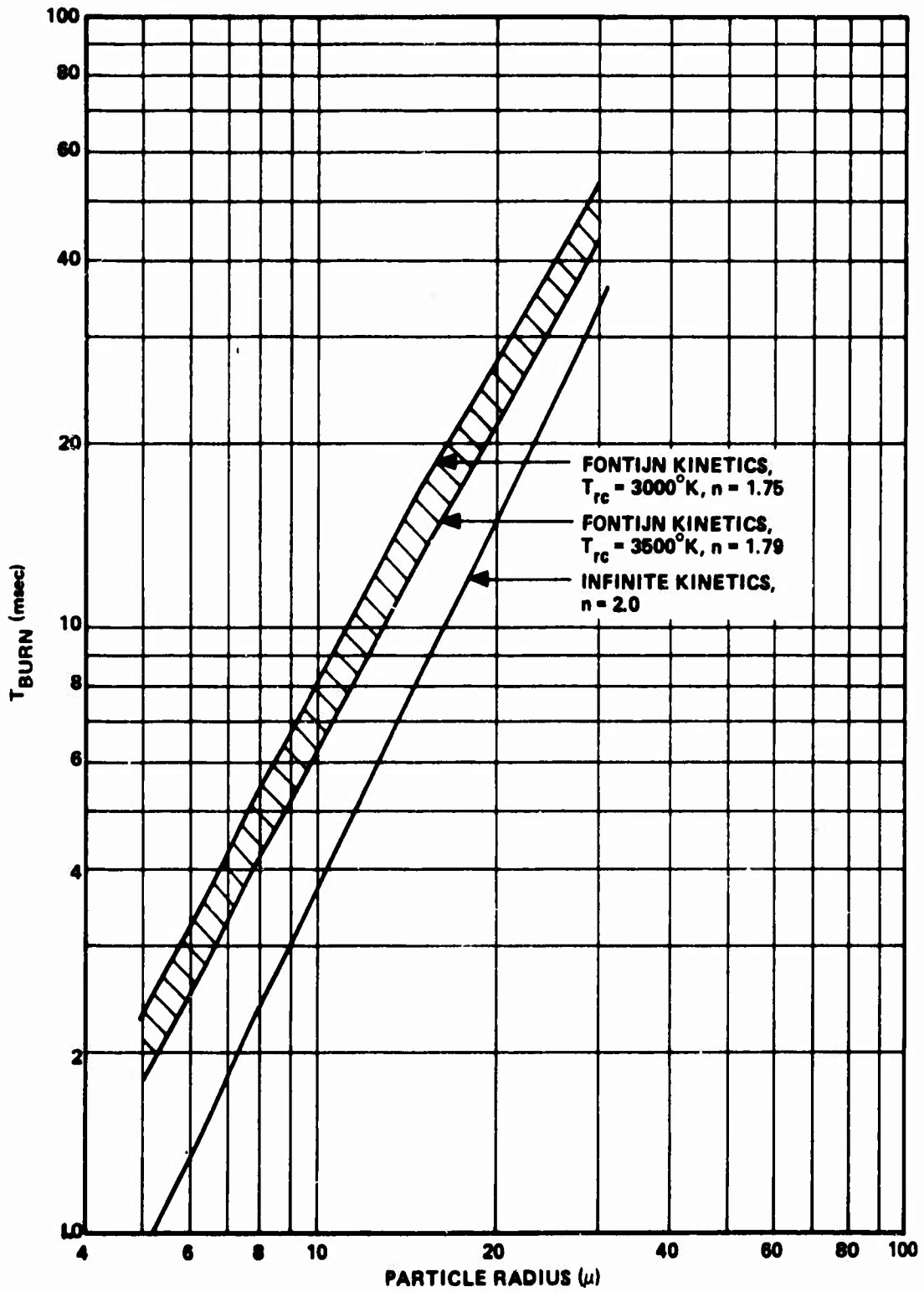


Figure III-10. Burn-Time Versus Particle Radius,  $T_{AMB} = 1000^{\circ}\text{K}$ ,  $P = 1 \text{ atm}$ ,  $Y_{\text{CO}_2} = 0.5$ .

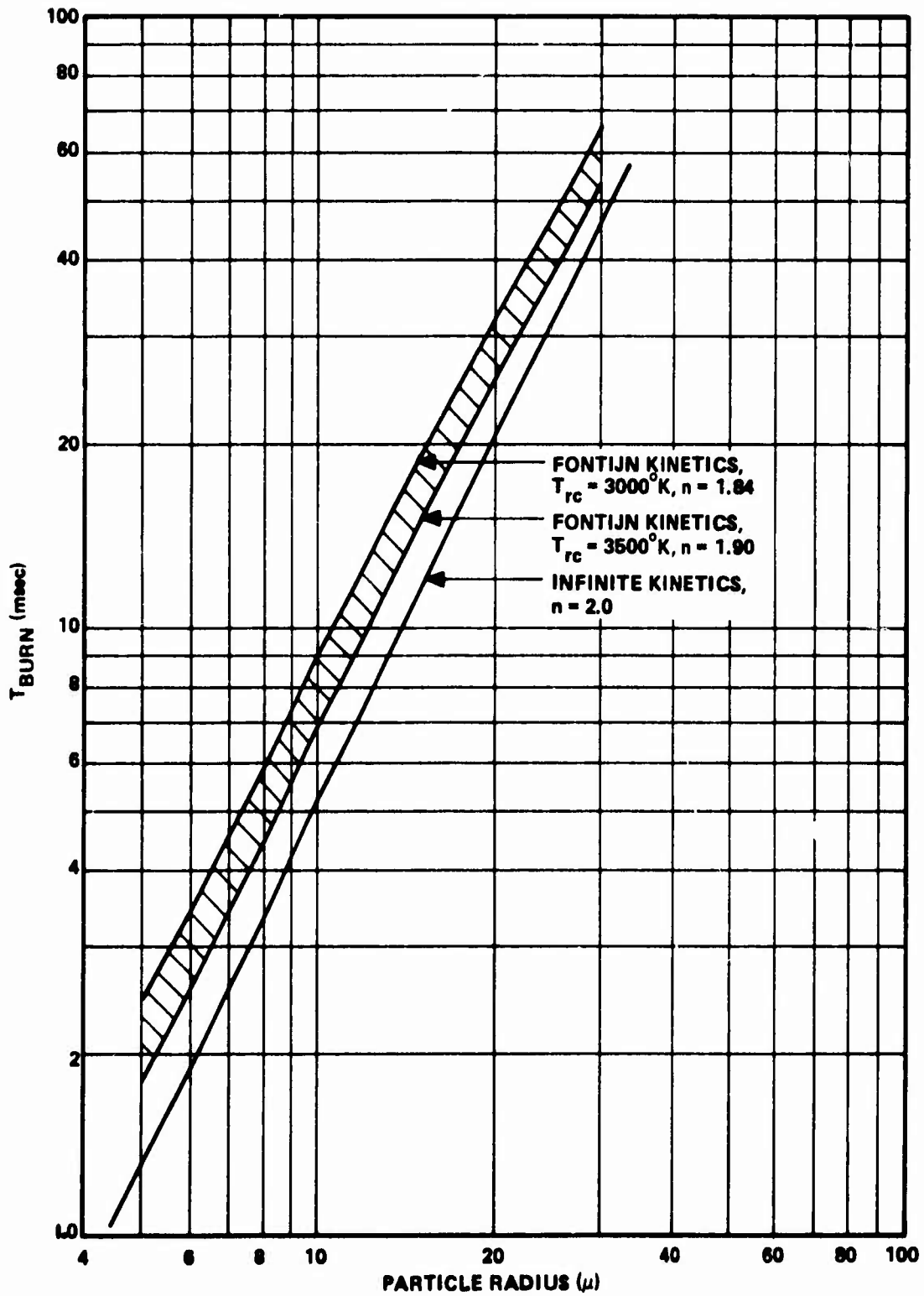


Figure III-11. Burn-Time Versus Particle Radius,  $T_{AMB} = 1000^{\circ}\text{K}$ ,  $P = 1 \text{ atm}$ ,  $Y_{\text{CO}_2} = 0.35$ .

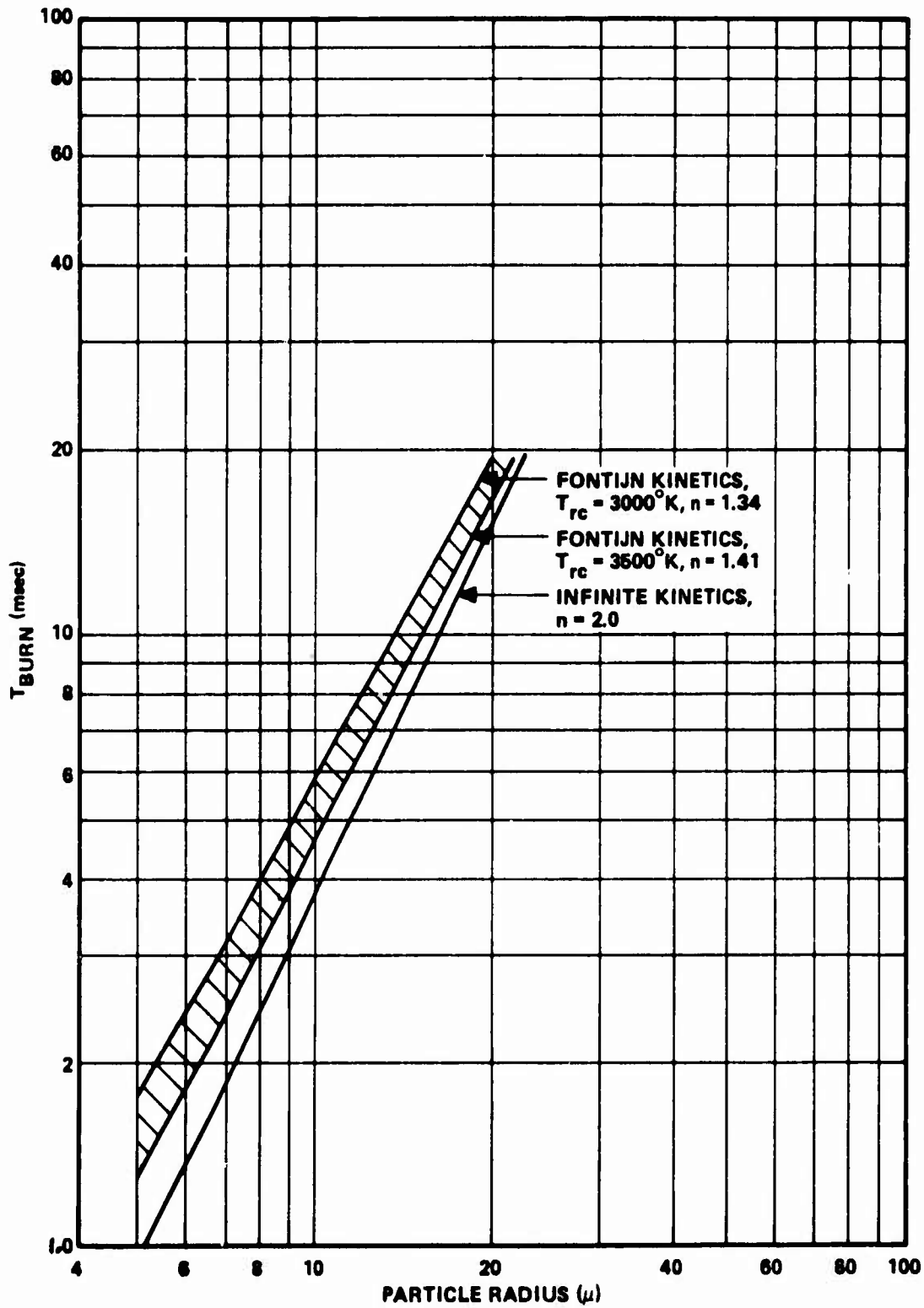


Figure III-12. Burn-Time Versus Particle Radius,  $T_{\text{AMB}} = 1000^{\circ}\text{K}$ ,  $P = 10 \text{ atm}$ ,  $Y_{\text{CO}_2} = 0.5$ .

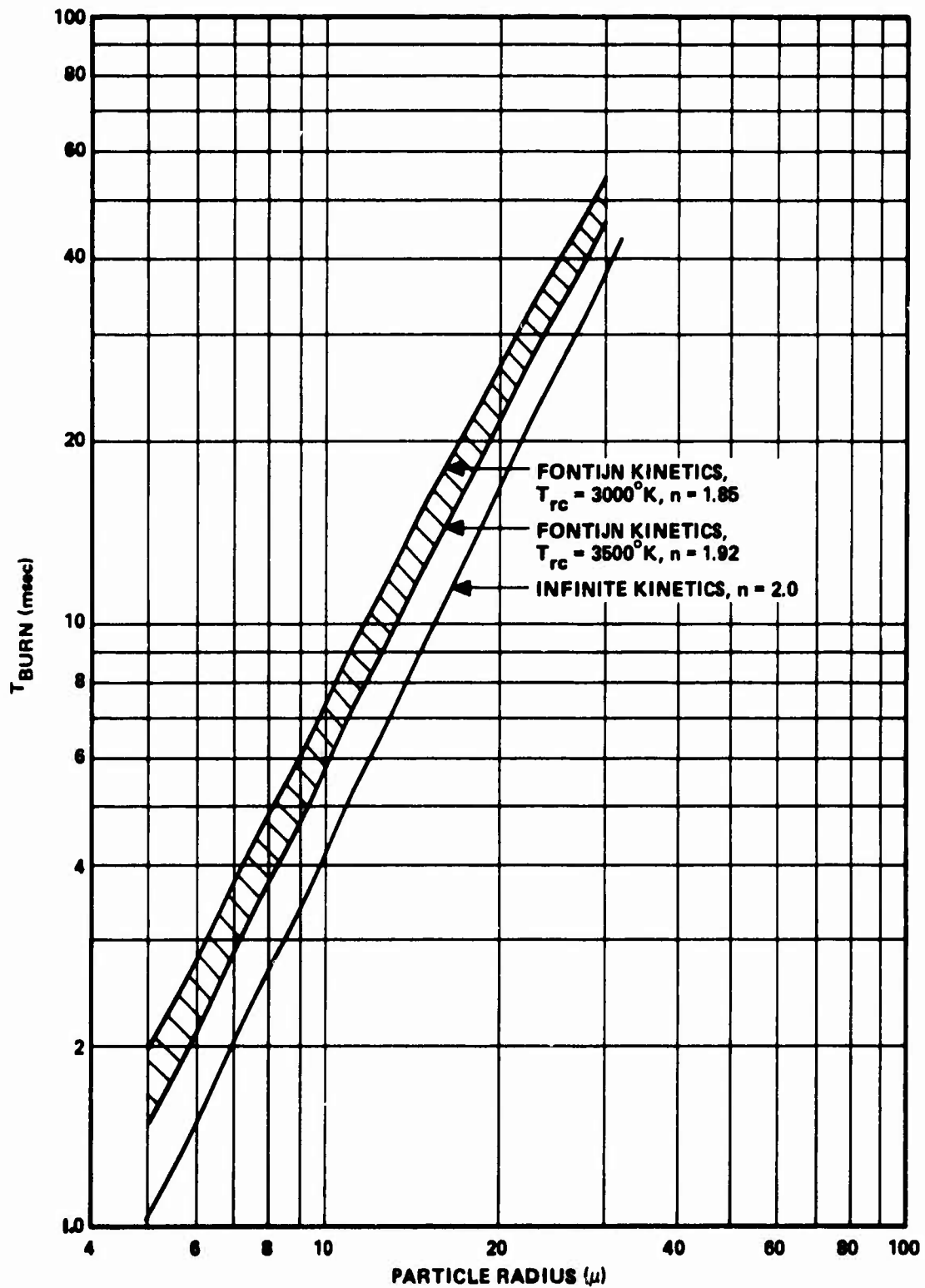


Figure III-13. Burn-Time Versus Particle Radius,  $T_{AMB} = 300^\circ\text{K}$ ,  $P = 1 \text{ atm}$ ,  $Y_{CO_2} = 0.5$ .

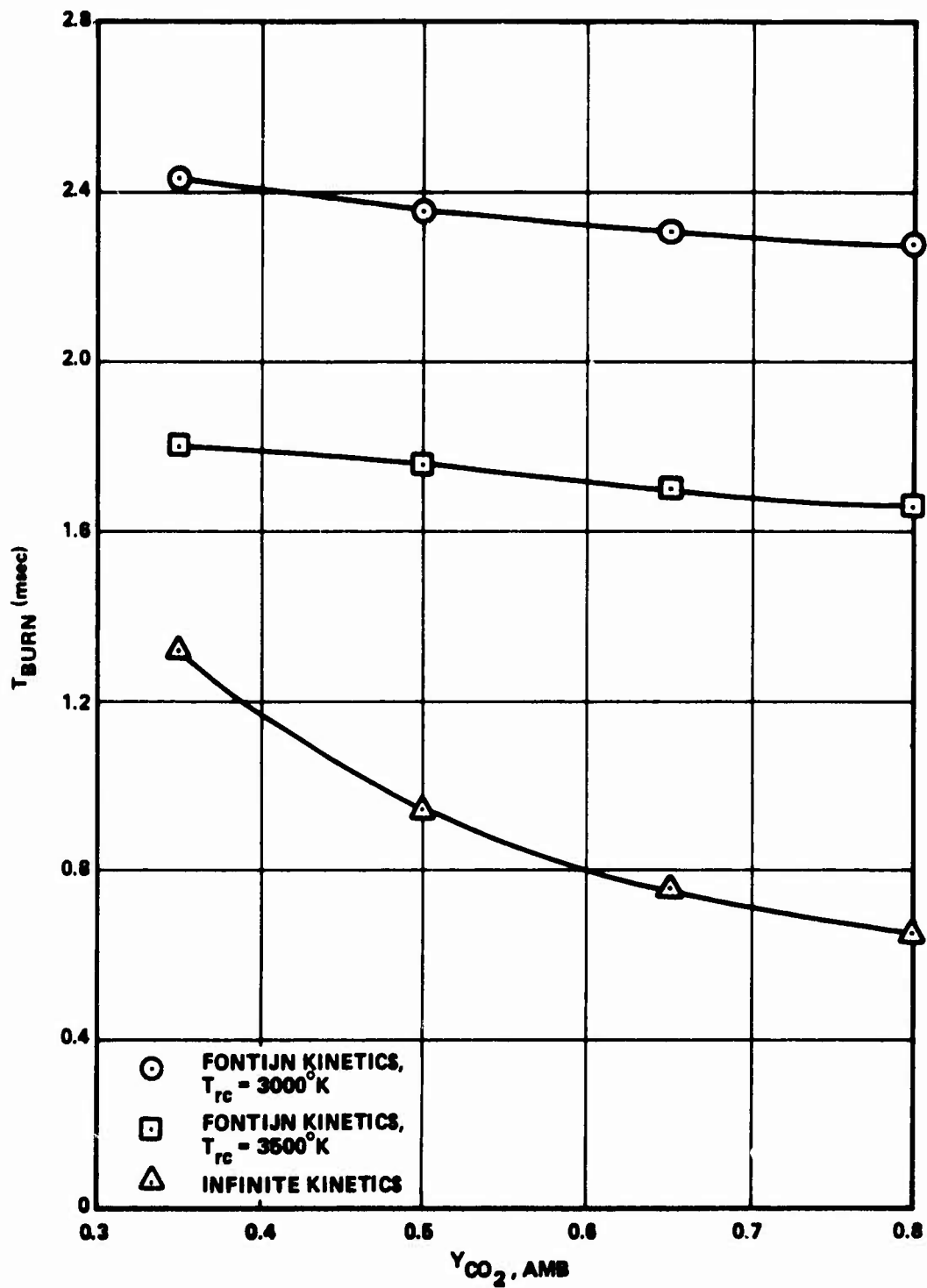


Figure III-14. Burn-Time Versus  $Y_{CO_2, AMB}$ ,  $P = 1 \text{ atm}$ ,  $T_{AMB} = 1000^\circ K$ ,  $r_p = 5\mu$ .

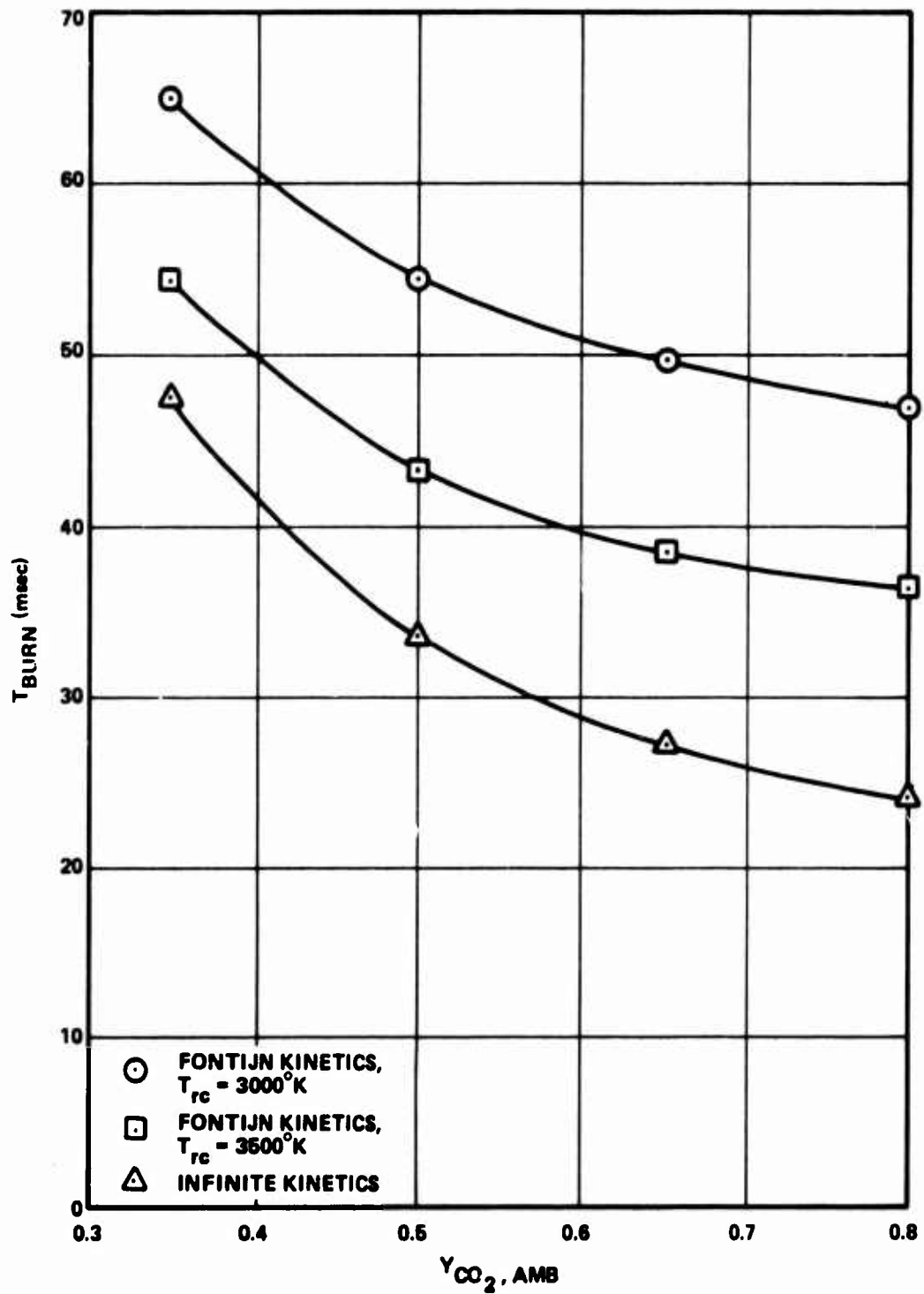


Figure III-15. Burn-Time Versus  $Y_{\text{CO}_2, \text{AMB}}$ ,  $P = 1 \text{ atm}$ ,  $T_{\text{AMB}} = 1000^{\circ}\text{K}$ ,  $r_p = 30\mu$ .

In Figures III-16 and III-17 predicted burn-times are plotted against pressure for small ( $5\mu$  radius) and large ( $20\mu$  radius) particles. While with infinite kinetics (diffusion-limited burning) the burn-time is predicted to be independent of pressure, with Fontijn kinetics burn-time is predicted to decrease with increasing pressure (an expected result). Finally, in Figures III-18 and III-19, predicted burn-time is plotted against ambient temperature for  $5\mu$  and  $20\mu$  radius particles. In both cases, for infinite kinetics, the predicted burn-time decreases with increasing ambient temperature. However, with Fontijn kinetics, for the  $5\mu$  particles, burn-time is predicted to increase with increasing ambient temperature, probably due to the burn rate in these cases being mainly determined by the location of the condensation shell, which moves out with increasing ambient temperature. This same trend is seen, though to a much lesser extent for the  $20\mu$  particles for the  $3000^\circ\text{K}$  condensation temperature case though not for the  $3500^\circ\text{K}$  case where the effect is sufficient to essentially eliminate the decrease in burn time with increased ambient temperature predicted for infinite kinetics, but not to reverse it.

#### E. Conclusions

A model of aluminum particle combustion in  $\text{CO}_2$  which incorporates measured kinetic data for the gas-phase reaction of aluminum with  $\text{CO}_2$  rather than assuming a flame-sheet (infinite gas-phase kinetics) as in past models has been developed, programmed and used to parametrically study the effect of various parameters on particle burning rate and burn-time. This model treats aluminum oxide condensation as occurring in an infinitesimally thin shell whose location is determined by specification of a condensation temperature. Condensation of aluminum oxide at the particle surface is not permitted, but  $\text{AlO}$  produced by the gas-phase reaction of aluminum vapor with  $\text{CO}_2$  is permitted to react with infinite kinetics with aluminum liquid at the surface to form  $\text{Al}_2\text{O}$  gas, thus removing aluminum from the surface as well as supplying heat to vaporize additional aluminum. Heat feedback from the condensation shell also provides additional energy for aluminum vaporization. Two variations of this model were developed: in one, any  $\text{CO}_2$  reaching the surface was permitted to react infinitely rapidly with aluminum

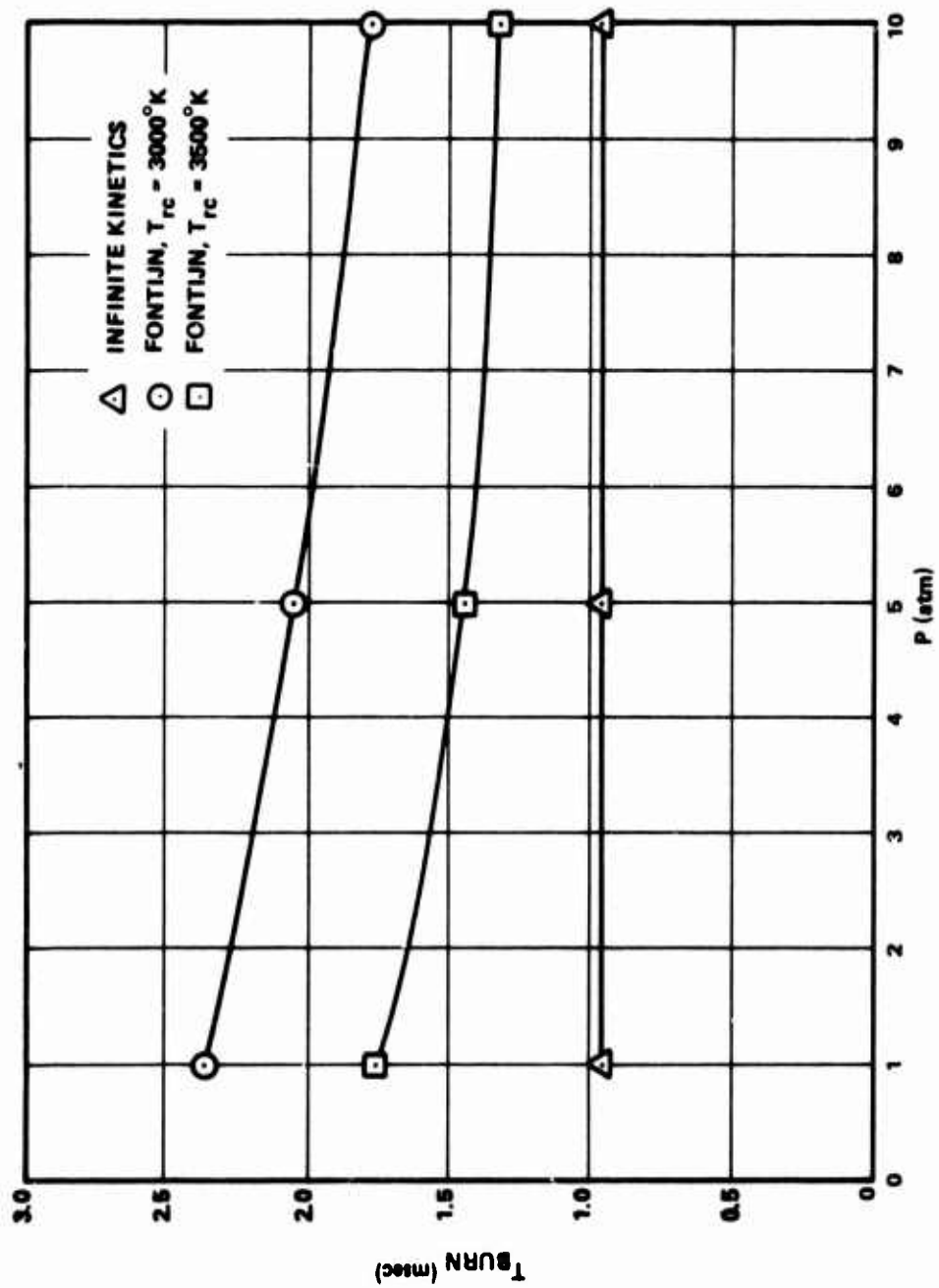


Figure III-16. Burn-Time Versus Pressure,  $Y_{CO_2} = 0.5$ ,  $T_{AMB} = 1000^\circ\text{K}$ ,  $r_p = 5\mu$ .

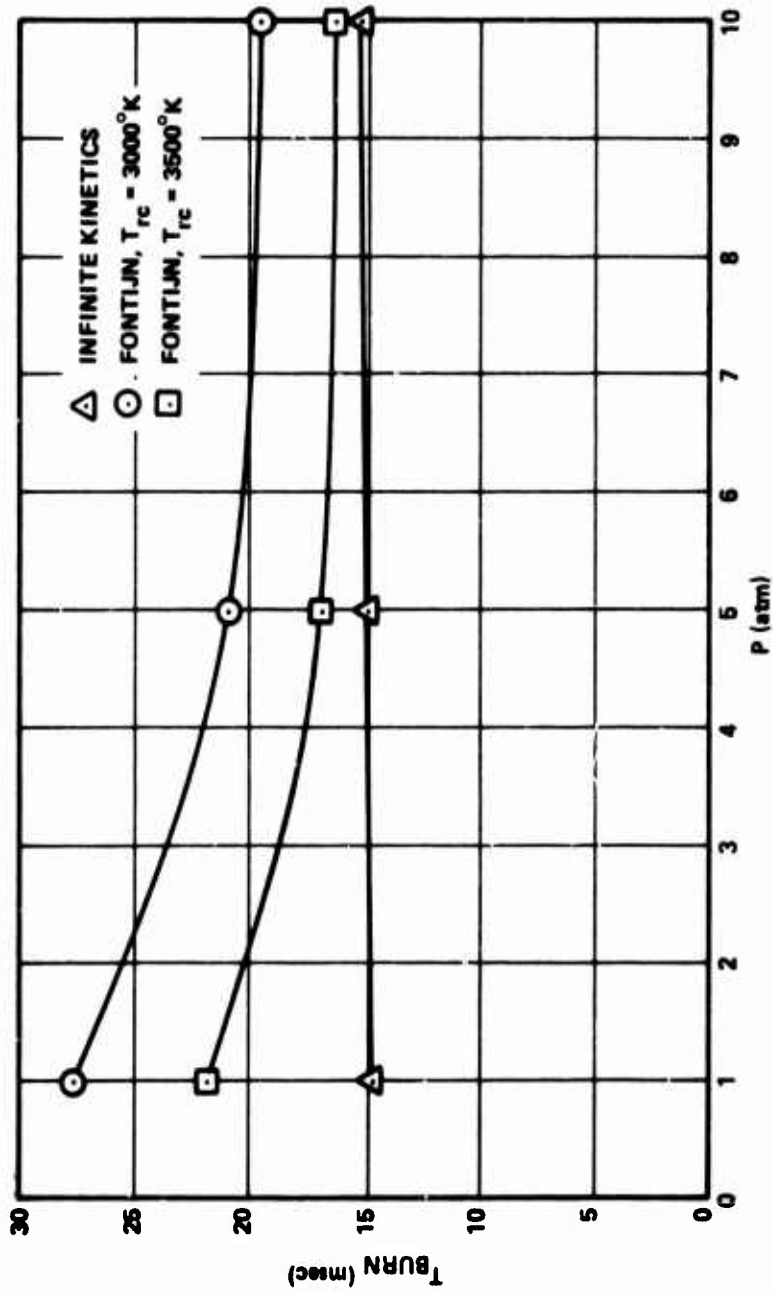


Figure III-17. Burn-Time Versus Pressure,  $Y_{CO_2} = 0.5$ ,  $T_{AMB} = 1000^\circ K$ ,  $r_p = 20\mu$ .

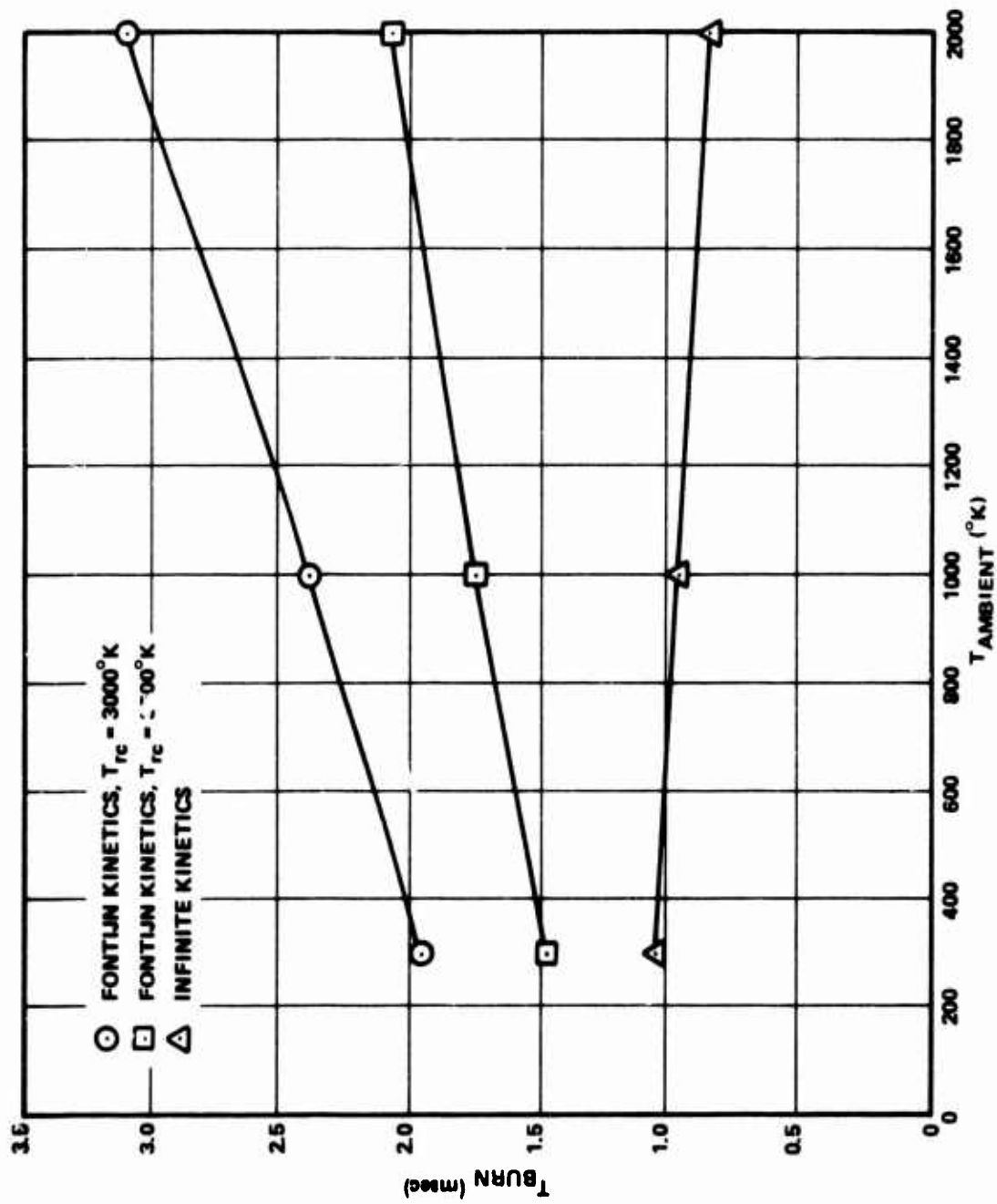


Figure III-18. Burn Time Versus T AMBIENT. P = 1 atm,  $Y_{CO_2} = 0.5$ ,  $r_p = 5\mu$ .

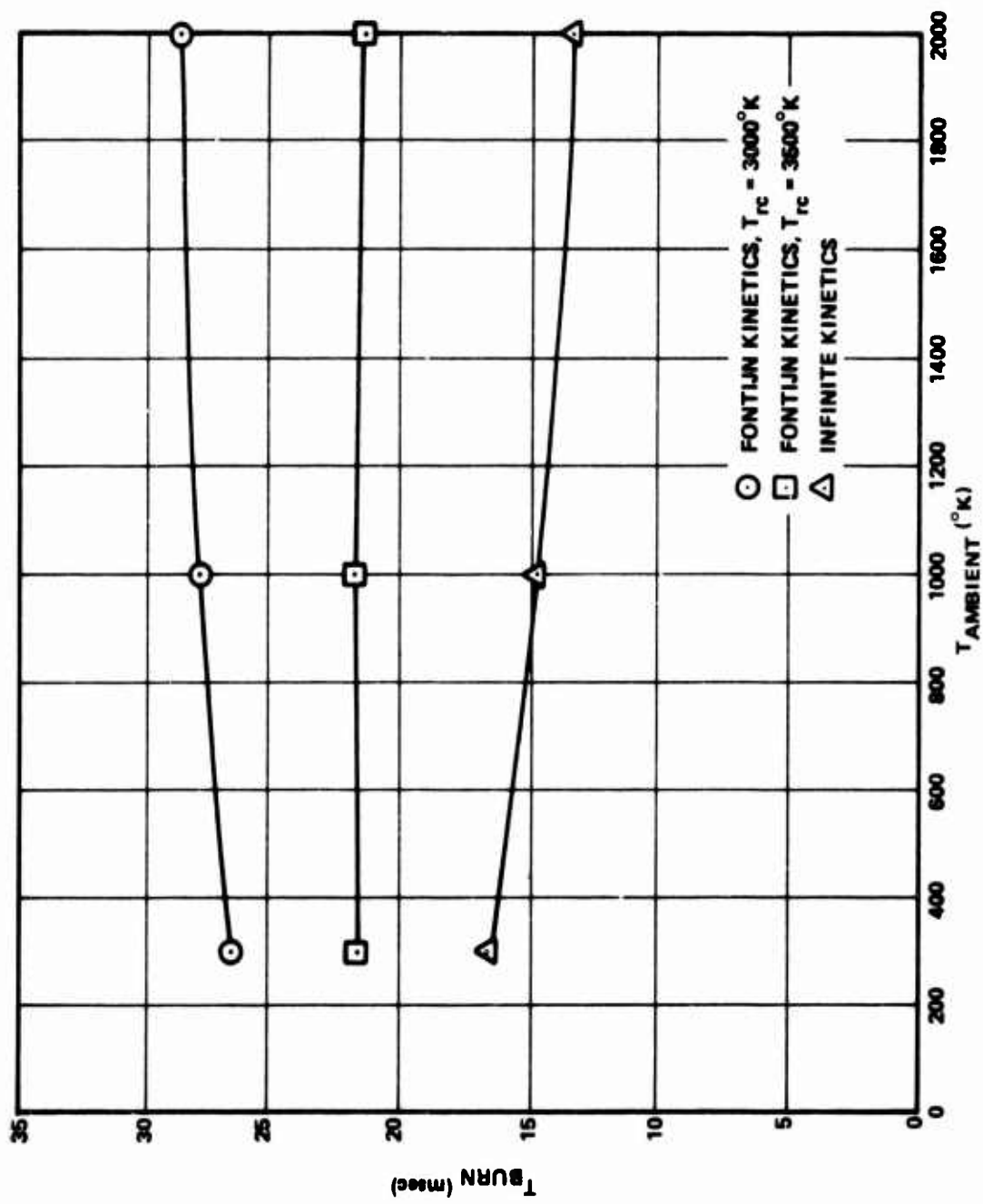


Figure III-19. Burn Time Versus T<sub>AMBIENT</sub>. P = 1 atm, Y<sub>CO<sub>2</sub></sub> = 0.5, r<sub>p</sub> = 20μ.

liquid to produce  $Al_2O$  gas, while in the other this reaction was prohibited. With the similarity approximations made in the model(s), the former variant leads to a degenerate solution in which the predicted burning rate is independent of the gas-phase kinetics, while the latter variant leads to burning rates predicted with the measured gas-phase kinetic data which are less than those predicted with infinite kinetics assumed. The ratio of burning rates predicted with the measured kinetic data to those predicted with infinite kinetics for the same conditions varies from about 0.3 to 0.95 over the range of conditions studied, increasing with increased particle size, increased pressure, decreased ambient  $CO_2$  mole fraction, and decreased ambient temperature. This ratio asymptotically approaches unity for large particle sizes and asymptotically approaches a value between zero and unity, which depends on ambient conditions, at very small particle sizes (where the location of the condensation shell dominates relative to gas-phase kinetics). Burn-time versus initial particle diameter calculations indicate a reduction in the exponent in the  $d^n$ -burning law ( $d_0^2 - d^2 = kt$ ) from 2 for the case of infinite kinetics (diffusion-limited burning) to 1.35 - 1.90, depending on ambient conditions.

#### IV. REFERENCES

##### A. Section II

1. Viles, J. M., "Prediction of Rocket-Motor Chamber Pressures Using Measured Erosive-Burning Rates," Technical Report S-275 (Contract DAAH01-70-C-0152), Rohm and Haas Co., Huntsville, Alabama 35807, October, 1970 (██████████).
2. Saderholm, C. A., "A Characterization of Erosive Burning for Composite H-Series Propellants," AIAA Solid Propellant Rocket Conference, Palo Alto, California, January 29, 1964.
3. Kreidler, J. W., "Erosive Burning: New Experimental Techniques and Methods of Analysis," AIAA Solid Propellant Rocket Conference, Palo Alto, California, January 29, 1964.
4. Schultz, R., Green, L., and Penner, S. S., "Studies of the Decomposition Mechanism, Erosive Burning, Sonance and Resonance for Solid Composite Propellants," Combustion and Propulsion, 3rd AGARD Colloquium, Pergamon Press, N. Y., 1958.
5. Green, L., "Erosive Burning of Some Composite Solid Propellants," Jet Propulsion, 24, 9, 1954.
6. Peretz, A., "Experimental Investigation of the Erosive Burning of Solid Propellant Grains with Variable Port Area," AIAA Journal, 6, 910, 1968.
7. Marklund, T., and Lake, A., "Experimental Investigation of Propellant Erosion," ARS Journal, 30, 173, 1960.
8. Dickinson, L. A., Jackson, F., and Odgers, A. L., "Erosive Burning of Polyurethane Propellants in Rocket Engines," Eighth Symposium (International on Combustion), 754, Williams and Wilkins, Baltimore, 1962.
9. Zucrow, M. J., Osborn, J. R., and Murphy, J. M., "An Experimental Investigation of the Erosive Burning Characteristics of a Nonhomogeneous Solid Propellant," AIAA Journal, 3, 523, 1965.
10. Vilyuncv, V. N., Dvoryashin, A. A., Margolin, A. D., Ordzhonikidze, S. K., and Pokhil, P. R., "Burning of Ballistite Type H in Sonic Flow," Fizika Goreniya i Vzryva, 8, 4, 501-5, October - December, 1972.
11. King, M., "Effects of Crossflow on Solid Propellant Combustion: Interior Ballistic Design Implications," 1976 JANNAF Propulsion Meeting, Atlanta, Georgia, December, 1976, CPIA Publ. 280, Vol. V, p. 342.
12. King, M., "Erosive Burning of Composite Propellants," 13th JANNAF Combustion Meeting, Monterey, California, September, 1976, CPIA Publ. 281, Vol. II, p. 407.

13. King, M., "A Model of the Erosive Burning of Composite Propellants," AIAA/SAE 13th Propulsion Conference, Orlando, Florida, July, 1977, AIAA Paper 77-930.
14. King, M., "A Modification of the Composite Propellant Erosive Burning Model of Lenoir and Robillard," Combustion and Flame, 24, 365-368, 1975.
15. Lenoir, J. M., and Robillard, G., "A Mathematical Method to Predict the Effects of Erosive Burning in Solid-Propellant Rockets," Sixth Symposium (International) on Combustion, 663, Reinhold Publishing Corp., New York, 1957.
16. Burick, R. J., and Osborn, J. R., "Erosive Combustion of Double-Base Solid Rocket Propellants," 4th ICRPG Combustion Conference, CPIA Publication No. 162, Vol. II, pp. 57-69, December, 1967.
17. Zucrow, M. J., Osborn, J. R., and Murphy, J. M., "The Erosive Burning of a Nonhomogeneous Solid Propellant," AICHE Symposium Series No. 52, 23-29, 1964.
18. Jojic, B., and Blagojevic, Dj., "Theoretical Prediction of Erosive Burning Characteristics of Solid Rocket Propellant Based on Burning Rate Dependence of Pressure and Initial Temperature and Its Energetic Characteristics," AIAA/SAE 12th Propulsion Conference, Palo Alto, California, July, 1976, AIAA Paper No. 76-697.
19. Saderholm, C. A., Biddle, R. A., Caveny, L. H., and Summerfield, M., "Combustion Mechanisms of Fuel Rich Propellants in Flow Fields," AIAA/SAE 8th Joint Propulsion Specialist Conference, New Orleans, Louisiana, November 29, 1972, AIAA Paper No. 72-1145.
20. Lengellé, G., "Model Describing the Erosive Combustion and Velocity Response of Composite Propellants," AIAA Journal, 13, 3, 315-322, March, 1975.
21. Corner, J., Theory of the Interior Ballistics of Guns, John Wiley and Sons, Inc., New York, 1950.
22. Vandenkerckhove, J., "Erosive Burning of a Colloidal Solid Propellant," Jet Propulsion, 28, 599, 1958.
23. Zeldovich, Y. B., "Theory of Propellant Combustion in a Gas Flow" Fizika Goreniya i Vzryva, 7, 4, 463-76, October - December, 1971.
24. Geckler, R. E., et al., Aerojet Engineering Corporation Report 445, 1950.
25. Tsuji, H., "An Aerothermochemical Analysis of Erosive Burning of Solid Propellant," Ninth International Symposium on Combustion, 384-393, 1963.

26. Beddini, R. A., Varma, A. K., and Fishburn, E. S., "A Preliminary Investigation of Velocity-Coupled Erosive Burning," 13th JANNAF Combustion Meeting, Monterey, California, September, 1976, CPIA Publication 281, Vol. II, p. 385.
27. Kuo, K. K., Razdan, M. K., and Kovolcin, R. L., "Theoretical and Experimental Investigation of Erosive Burning of Non-Metalized Composite Solid Propellants," Presented at 1977 Joint AFOSR/AFRPL Rocket Propulsion Research Meeting, Lancaster, California, March, 1977.
28. Klimov, A. M., "Erosive Burning of Propellants," Combustion, Explosion and Shock Waves, 11, 5, October, 1976, p. 678 (Translated from Fizika Goreniya i Vzryva, 11, 5, September - October, 1975, p. 793).
29. Molnar, O., "Erosive Burning of Propellant Slabs," AIAA/SAE 8th Joint Propulsion Specialist Conference, New Orleans, Louisiana, November, 1972, AIAA Paper 72-1108.
30. Miller, E., "Erosive Burning of Composite Solid Propellants," Combustion and Flame, 10, p. 330, December, 1966.
31. Mickley, H. S., and Davis, R. S., "Momentum Transfer for Flow Over a Flat Plate with Blowing," NACA Technical Note 4017, November, 1975.
32. Beckstead, M. W., Derr, R. L., and Price, C. F., "The Combustion of Solid Monopropellants and Composite Propellants," Thirteenth International Symposium on Combustion, The Combustion Institute, Pittsburgh, Pennsylvania, 1971, pp. 1047-1056. Also, "Combustion Tailoring Criteria for Solid Propellants," Lockheed Propulsion Company Report 835F (AFRPL-TR-69-190), May, 1969.
33. Waesche, R. H. W., and Wenograd, J., "Calculation of Solid Propellant Burning Rates from Condensed-Phase Decomposition Kinetics," AIAA 7th Aerospace Sciences Meeting January, 1969, AIAA paper 69-145. Also, United Aircraft Final Report on Research Investigation of the Decomposition of Composite Solid Propellants, Report No. H910457-37, September, 1969.
34. Burke, S. P., and Schumann, T. E. W., "Diffusion Flames," Ind. and Eng. Chem., 20, 10, p. 998, October, 1928.
35. Andersen, W. H., and Chaiken, R. F., "Detonability of Solid Composite Propellants," ARS Journal, 1379, 1961.
36. Cohen, N., Fleming, R., and Derr, R., "Role of Binders in Solid Propellant Combustion," AIAA/SAE 8th Propulsion Joint Specialist Conference, November, 1972, AIAA Paper 72-1121.
37. Yamada, K., Goto, M., and Ishikawa, N., "Simulative Study on the Erosive Burning of Solid Rocket Motors," AIAA Journal, 14, 9, p. 1170, September, 1976.
38. Dunlap, R., Willoughby, P. G., and Hermsen, R. W., "Flowfield in the Combustion Chamber of a Solid Propellant Rocket Motor," AIAA Journal, 12, 10, p. 1440, October, 1974.

3. Section III

1. Coffin, K. P., and Brokaw, R. S., "A General System for Calculating Burning Rates of Particles and Drops and Comparison of Calculated Rates for Carbon, Boron, Magnesium, and Iso-Octane," NACA Tech. Note 3929, Feb., 1957.
2. Brzustowski, T. A., and Glassman, I., "Vapor-Phase Diffusion Flames in the Combustion of Magnesium and Aluminum. I. Analytical Developments," AIAA Paper 63-489, Dec., 1963.
3. Kuehl, D. K., and Zwillenberg, M. L., "Predictions of Burning Times of Metal Particles," AIAA Paper 68-494, June, 1968.
4. Law, C. K., "A Simplified Theoretical Model for the Vapor-Phase Combustion of Metal Particles," Combustion Science and Technology, 7, p. 197, 1973.
5. Law, C. K., and Williams, F. A., "Combustion of Magnesium Particles in Oxygen-Inert Atmospheres," Combustion and Flame, 22, pp. 383-405, 1974.
6. Macek, A., "Fundamentals of Combustion of Single Aluminum and Beryllium Particles, 11th International Symposium on Combustion, The Combustion Institute, Pittsburgh, Pa., pp. 203-217, 1967.
7. Pokhil, P. R., et al., Combustion of Powdered Metals in Active Media, FTD-MT-24-551-73, Foreign Technology Division Translation from Russian Text, Oct. 18, 1973.
8. Fontijn, A., and Felder, W., "HTFFR Kinetic Studies of  $Al + CO_2 \rightarrow AlO + CO$  from 300 to 1800°K, a Non-Arrhenius Reaction," Project SQUID Technical Report AC-16-PU, 1977.
9. King, M. K., "Preliminary Examination of the Validity of the Flame-Sheet Approximation for Aluminum Particle Combustion Modeling, Presented at the 14th JANNAF Combustion Meeting, Colorado Springs, Colorado, August, 1977. To be published in CPIA Publication of Proceedings of this meeting.
10. Polymeropoulos, C. E., and Peskin, R. L., "Ignition and Extinction of Liquid Fuel Droplets - Numerical Computations," Combustion and Flame, 13, pp. 166-72, April, 1969.
11. Ahlert, R. C., Peskin, R. L., Gaston, J. W., and Ridgik, T., "Interaction of Droplet Size Ignition Requirements in External Burning," AIAA Paper 70-607, June, 1970.
12. Henderson, C. B., "A Proposed Combustion Scheme for the Gaseous Oxidation Reaction of Beryllium and Aluminum," Combustion Science and Technology, 1, pp. 275-78, 1970.

13. Benson, S. W., The Foundations of Chemical Kinetics, McGraw-Hill, N.Y., 1960, pp. 267-318.
14. Gordon, A. S., Drew, C. M., Prentice, J. L., and Knipe, R. H., "Techniques for the Study of the Combustion of Metals,"
15. Prentice, J. L., "On the Combustion of Single Aluminum Particles," Combustion and Flame, 9, 1965, p. 208.
16. Razdobreev, A. A., Skorik, A. I., and Frolov, Y. V., "Ignition and Combustion Mechanism in Aluminum Particles," Fizika Gorennya i Vzryva, 12, 2, pp. 203-208, March-April, 1976.
17. Crump, J. E., Prentice, J. L., and Krautle, K. J., "Role of the Scanning Electron Microscope in the Study of Solid Propellant Combustion: II. Behavior of Metal Additives," Combustion Science and Technology, 1, pp. 205-223, 1969.
18. Prentice, J. L., "Combustion of Pulse-Heated Single Particles of Aluminum and Beryllium," Combustion Science and Technology, 1, pp. 385-98, 1970.
19. Prentice, J. L., "Aluminum Droplet Combustion: Rates and Mechanisms in Wet and Dry Oxidizers," NWC TP 5569, Naval Weapons Center, China Lake, Calif., April, 1974.
20. Williams, F., Combustion Theory, Addison-Wesley Publ. Co., Reading, Mass., p. 11, 1965.

V. CHRONOLOGICAL BIBLIOGRAPHY OF PAPERS AND REPORTS RESULTING FROM CONTRACT F44620-76-C-0023

1. King, M. K. "Study of Erosive Burning Phenomena in Composite Propellants," Progress Report (October 1, 1975 to September 30, 1976), AFOSR Contract F44620-76-C-0023, November 17, 1976, Report No. AFOSR-TR-76-1251.
2. King, M. K., "Erosive Burning of Composite Propellants," 13th JANNAF Combustion Meeting, Monterey, California, September, 1976, CPIA Publication 281, Vol. II, p. 407, December, 1976.
- \*3. King, M. K., "Effects of Crossflow on Solid Propellant Combustion: Interior Ballistic Design Implications," 1976 JANNAF Propulsion Meeting, Atlanta, Georgia, December, 1976, CPIA Publication 280, Vol. V., p. 341.
4. King, M. K., "A Model of Erosive Burning of Composite Propellants," AIAA/SAE 13th Propulsion Conference, Orlando, Florida, July, 1977, AIAA Paper 77-930. Also accepted for publication in Journal of Spacecraft and Rockets.
5. King, M. K., "An Analytical and Experimental Investigation of the Erosive Burning of Composite Propellants," 14th JANNAF Combustion Meeting, Colorado Springs, Colorado, August, 1977. To appear in upcoming CPIA publication.
- \*6. King, M. K., "Preliminary Examination of the Validity of the Flame-Sheet Approximation for Aluminum Particle Combustion Modeling," 14th JANNAF Combustion Meeting, Colorado Springs, Colorado, August, 1977. To appear in upcoming CPIA publication.
7. King, M. K., "Model for Steady-State Combustion of Unimodal Composite Solid Propellants," To be presented at AIAA 16th Aerospace Sciences Meeting, Huntsville, Alabama, January, 1978, AIAA Paper 78-216.

\* Generated largely under Atlantic Research IR&D funds, but including information generated on Contract F44620-76-C-0023.